PHOTOSYSTEM I – BASED SYSTEMS FOR PHOTOELECTROCHEMICAL ENERGY CONVERSION

By

Peter N. Ciesielski

Dissertation

Submitted to the Faculty of the

Graduate School of Vanderbilt University

in partial fulfillment of the requirements

for the degree of

DOCTOR OF PHILOSOPHY

in

Interdisciplinary Materials Science

August, 2010

Nashville, Tennessee

Approved:

Professor G. Kane Jennings

Professor David E. Cliffel

Professor Paul E. Laibinis

Professor Sharon M. Weiss

Professor Norman H. Tolk

ACKNOWLEDGEMENTS

I am very grateful first and foremost to God for creating such elegant and intriguing photoelectrochemical nanoscale devices and for allowing me to use some of them for this thesis. Next, it is an honor for me to thank my advisor G. Kane Jennings for opening my eyes to things that are too small to see, and for subjecting my papers to the rigorous and infamous "Jennings Scale of Completion," which has extracted the very best that work I am capable of producing. I am very grateful to my co-advisor David Cliffel whose expertise and creative ideas have been an essential and consistent component of this work. I would like to thank Norman Tolk and Sandra Rosenthall for their contributions of time and resources which expanded this project in new directions, and I am grateful to Sharon Weiss and Paul Laibinis for serving on my committee and offering their insight and assistance. This thesis would not have been possible without the experimental contributions of my co-workers, namely Christopher Faulkner, Justin Gregory, Amanda Scott, Fred Hijazi, Matt Irwin, and Kevin Emmett. I am also grateful to my colleagues in the Jennings and Cliffel groups who made the labs fun and productive places to work.

I would like to thank my wife Bethany who supported me throughout my time in graduate school, lent some of her awesome editing skills to my papers, and tolerated me pausing movies in the middle when I had a weird idea that couldn't wait to be explained and recorded. I would also like to thank my parents for raising me to be inquisitive and rewarding my creativity, and for loving me even when I made bad decisions. I am grateful to my twin sister Emily for being loving and supportive throughout our

childhood, and my friends in Colorado for being like brothers to me. I would like to thank my grandparents for their constant love and prayers, and the Gonzales family for adopting me and being my family while I have been in Tennessee.

I gratefully acknowledge the financial support provided by an IGERT fellowship (NSF 0333392), the National Science Foundation (DMR 0907619), and the Department of Energy (DE-FGO2–99ER45781) that made this work possible.

TABLE OF CONTENTS

Page

LIST OF TABLES

LIST OF FIGURES

CHAPTER I

INTRODUCTION TO PHOTOSYSTEM I AND ITS BEHAVIOR IN PHOTOELECTROCHEMICAL SYSTEMS

Photosynthesis is the natural solar energy conversion process that has long allowed plants and certain types of bacteria to thrive on the ample amount of sunlight that reaches our planet[1] and accounts for the annual conversion of 10^{11} metric tons of CO_2 to organic matter, which equates to a storage of 4×10^{21} J of free energy in the form of reduced carbon.[2] This process is carried out by a tandem of protein complexes of impressive complexity that coordinate the tasks of light absorption and transduction, charge separation, electron transport, and catalysis of redox reactions. The success of photosynthesis has resulted in the continual, mass-production of these nanoscale biochemical constituents of the process by the superabundant photosynthetic organisms on our planet. One of these constituents, Photosystem I (PSI), is a ~500 kDa protein complex located in the thylakoid membranes of chloroplasts found within most organisms that perform oxygenic photosynthesis. PSI exhibits particularly useful functionality: with a quantum efficiency near unity, the protein complex operates as a photodiode for the transport of electrons across the thylakoid membrane.[3] Plant PSI is a complex of 17 smaller protein subunits that coordinate approximately 100 chlorophylls, 2 phylloquinones, and 3 iron-sulfur complexes.[4] The structure of PSI shown in **Figure 1.1** also contains 4 light-harvesting subunits that are known to orient additional chlorophylls around the periphery of the main antenna complex, bringing the chlorophyll

total of the super-complex to ~ 180.[5] These antenna chlorophylls allow PSI to harvest energy from incident photons and subsequently transfer that energy with impressive speed and efficiency to a reaction center composed of a special pair of chlorophylls (denoted P_{700}) where a resident electron is excited, causing charge separation to occur within 10-30 picoseconds.[6] Following the charge separation event, the excited electron travels down an electron transfer chain made up of chlorophylls, phylloquinones, and iron-sulfur complexes.[7] The terminal electron acceptor of the chain is an Fe-S cluster denoted F_B, and the redox potential of -0.59 V vs NHE achieved by this complex when in the reduced state (designated F_B^-) is among the most negative found in nature.[8] The tertiary structure of PSI includes two docking sites for the other proteins: one located near the iron-sulfur clusters for chloroplast ferredoxin, a redox protein that is reduced by F_B^- in natural photosynthesis, and another near the P_{700} chlorophyll dimer for a copper containing protein called plastocyanin which is responsible for resupplying electrons to P_{700}^+.

The rapid, photo-induced charge transfer capabilities of PSI have earned the protein a reputation as "arguably the smallest, fastest, and most efficient photovoltaic cell,"[9] which has attracted much attention from researchers seeking to utilize PSI's functionality. The origins of this research are found in the work of Greenbaum whose 1985 publication in *Science* reported the use of platinized chloroplasts for photosynthetic hydrogen production.[10] This work progressed to the use of PSI complexes further isolated from the chloroplasts, and direct platinization of the F_B FeS clusters was achieved by Lee and Greenbaum at Oak Ridge National Lab in 1995.[9, 11] Several years later, these researchers reported an intriguing result upon which the basis for the

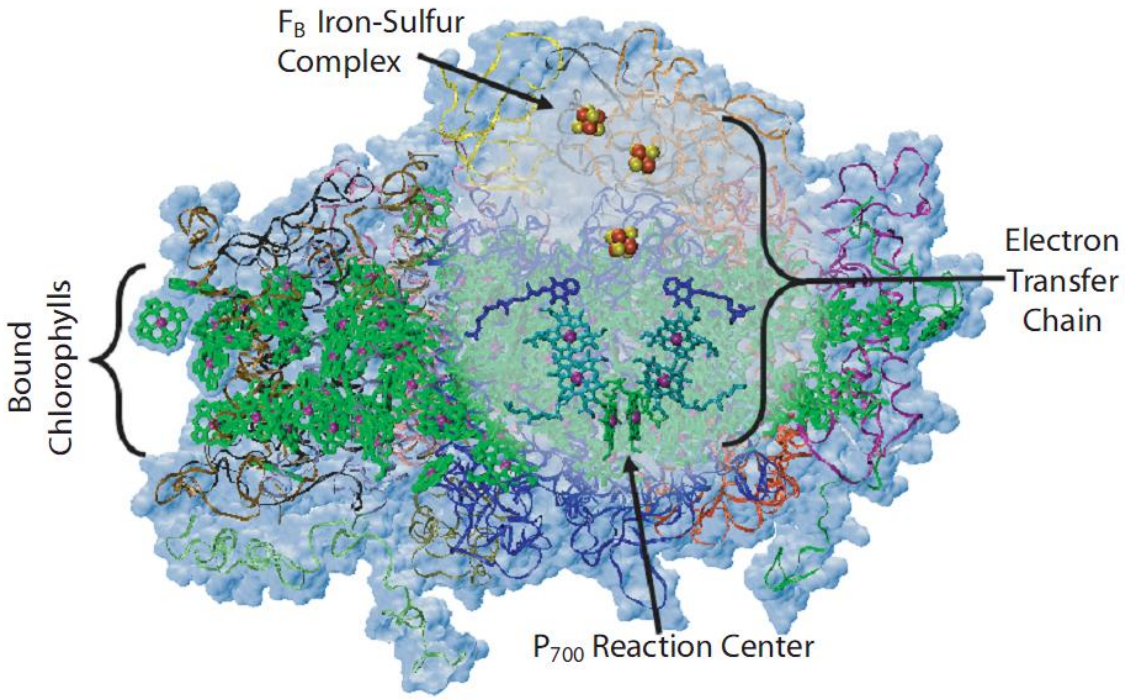

Figure 1.1. Structure of Plant Photosystem I. Chlorophylls oriented within PSI collect photonic energy and transfer it to a special pair of chlorophylls that make up the P_{700} reaction center. Upon receipt of this energy, charge separation occurs rapidly at P_{700} as an electron is released into an electron transfer chain to eventually reduce an iron sulfur cluster, denoted F_B, that is located on the opposite side of the protein complex. Atomic coordinates used in this figure are from PDB entry 2o01, contributed by Amunts *et al.* [5]

studies in this thesis are derived: PSI complexes immobilized on the surface of a substrate acted as nanoscale diodes, and allowed transport of charge in a vectorial direction that was thought to be parallel to the electron transport chain of the protein.[12] These observations were verified by scanning tunneling spectroscopy in which I-V scans were performed using a scanning probe above individual protein complexes, and changes in the scans were attributed to different orientations of the electron transport vector of PSI with respect to the probe and substrate. Soon thereafter, electrochemical investigations of PSI films were undertaken by Rusling and colleagues at the University of Connecticut. Rusling was able to observe direct electron transfer between both the P_{700} reaction center and the F_A/F_B iron-sulfur complexes of PSI in a lipid film on an electrode surface by way of cyclic voltammetry.[13] The photocatalytic capability of PSI complexes in solution was also demonstrated via cyclic voltammetry in a study by Bourdillon and coworkers, and the results were used to determine electron transfer kinetics between PSI and the various redox couples present in the system.[14] In 2006, Terasaki and coworkers fabricated a high-surface area electrode comprised of gold nanoparticles and decorated with PSI that was capable of producing larger catalytic currents than planar electrodes.[15] Since then, the Terasaki group has improved their PSI-based electrochemical systems by developing an attachment/orientation scheme based on genetic mutants of PSI,[16] and have produced several biohyrbrid photosensors based on this technology.[17, 18] Meanwhile, the photoactivity of adsorbed PSI complexes in a solid-state system was measured using Kelvin force probe microscopy by Frolov and Carmelli, wherein a change in surface voltage was exhibited by the PSI film in response to irradiation.[19] In 2004, a solid-state PSI-base photovoltaic device was produced by

Das *et al.*,[20] but this research has yet to yield additional studies apart from the original publication. The research of Frolov and Carmelli, however, progressed to investigate the enhanced surface photovoltage produced by PSI multilayer films,[21] and produce PSI-based field effect transistors.[22]

Our group began investigating the adsorption of PSI films onto substrates modified by self-assembled monolayers (SAMs) of various ω-terminated alkanethiols in 2004.[23] We observed that PSI adsorbs to hydrophilic surfaces but not to hydrophobic surfaces due to the mediating effect of the Triton-X surfactant, and we demonstrated that PSI could be entrapped within films comprised of long-chain alkanethiols using a back-filling technique.[24] The selective adsorption of PSI was used to direct the deposition of PSI onto pre-patterned surfaces that we imaged using scanning electrochemical microscopy.[25] We then reported direct electrochemistry of the reaction centers of PSI complexes in adsorbed monolayers and we showed that these PSI monolayers could produce an increase in chronoamperometric current in response to irradiation.[26] Several strategies for the covalent attachment of PSI to functionalized SAMs were developed in tandem with a vacuum assisted assembly technique for the rapid preparation of dense PSI monolayers by Faulkner *et al.*[27] These studies demonstrated that PSI retained its functionality after its immobilization onto various substrates, and furthermore, that monolayer films of PSI complexes could produce a photocurrent when incorporated into an electrochemical system by photoinduced electron transfer between PSI's reaction centers and the electrode surface (shown schematically in **Figure 1.2**).

Building from these results, the studies presented in this work further elucidate the photocatalytic behavior of PSI complexes in electrochemical systems, present

strategies by which this technology may be improved to produce larger photocurrents, and describe construction of a stand-alone PSI-based solar energy conversion device. These bio-hybrid photoelectrochemical energy conversion systems are fundamentally different from the majority of biomaterial-based renewable energy platforms, in which biomass or its chemically processed derivatives such as ethanol and biodiesel are burned as fuel,[28] because the energetic driving force for the photoelectrochemical processes comes directly from light, rather than exothermic liberation of energy stored in chemical bonds by combustion of the material. The results presented herein demonstrate that the functionality of PSI is, in fact, a valuable natural resource that holds great potential for its utility in solar energy conversion systems.

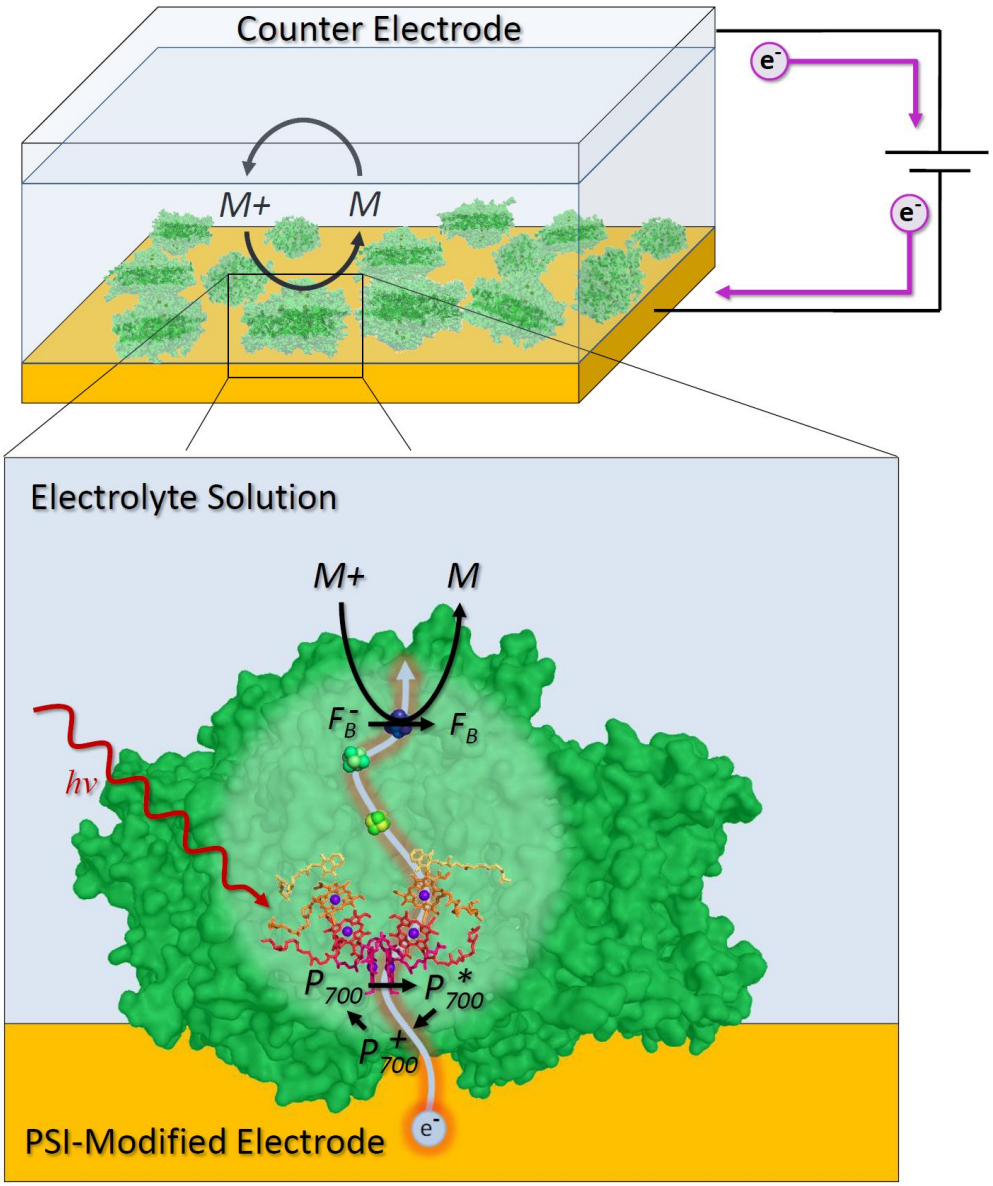

Figure 1.2. Cathodic Photocurrent Production by a PSI Monolayer on an Electrode Surface. In response to irradiation, charge separation occurs within PSI complexes on the electrode surface. Electrons are removed from the reduced iron-sulfur complex, denoted F_B^- , by an electrochemical mediator and carried to the counter electrode by electrochemical mediators (denoted "M"). Electrons are resupplied to the oxidized chlorophyll dimer reaction center, denoted P_{700}^+, by its direct reduction by the electrode.

Works Cited

1. Bjorn, L.O. and Govindjee, *The evolution of photosynthesis and its environmental impact*, in *Photobiology: The Science of Life and Light, Second Edition*, L.O. Bjorn, Editor. 2008, Springer. p. 255-287.

2. Govindjee, *Milestones in Photosynthesis Research*, in *Probing Photosynthesis Mechanisms, Regulation and Adaptation*, M. Yunus, U. Pathre, and P. Mohanty, Editors. 2000, Taylor & Francis: London. p. 9-31.

3. He, W.Z. and R. Malkin, *Photosystems I and II*, in *Photosynthesis: A Comprehensive Treatise*, A.S. Raghavendra, Editor. 1998, Cambridge University Press: Cambridge. p. 29-43.

4. Nelson, N. and C.F. Yocum, *Structure and function of photosystems I and II.* Annual Review of Plant Biology, 2006. **57**: p. 521-565.

5. Amunts, A., O. Drory, and N. Nelson, *The structure of a plant photosystem I supercomplex at 3.4 Å resolution.* Nature, 2007. **447**(7140): p. 58-63.

6. Chitnis, P.R., *Photosystem I: Function and physiology.* Annual Review of Plant Physiology and Plant Molecular Biology, 2001. **52**: p. 593-626.

7. Brettel, K. and W. Leibl, *Electron transfer in photosystem I.* Biochimica Et Biophysica Acta-Bioenergetics, 2001. **1507**(1-3): p. 100-114.

8. Nelson, N. and A. Ben-Shem, *The structure of photosystem I and evolution of photosynthesis.* Bioessays, 2005. **27**(9): p. 914-922.

9. Lee, J.W. and E. Greenbaum, *Bioelectronics and Biometallocatalysis for Production of Fuels and Chemicals by Photosynthetic Water-Splitting.* Applied Biochemistry and Biotechnology, 1995. **51-2**: p. 295-305.

10. Greenbaum, E., *Platinized Chloroplasts: A Novel Photocatalytic Material.* Science, 1985. **230**(4732): p. 1373-1375.

11. Lee, J.W., et al., *Chemical Platinization and Its Effect on Excitation Transfer Dynamics and P700 Photooxidation Kinetics in Isolated Photosystem-I.* Biophysical Journal, 1995. **69**(2): p. 652-659.

12. Lee, I., J.W. Lee, and E. Greenbaum, *Biomolecular electronics: Vectorial arrays of photosynthetic reaction centers.* Physical Review Letters, 1997. **79**(17): p. 3294-3297.

13. Munge, B., et al., *Electron Transfer Reactions of Redox Cofactors in Spinach Photosystem I Reaction Center Protein in Lipid Films on Electrodes.* Journal of the American Chemical Society, 2003. **125**(41): p. 12457-12463.

14. Proux-Delrouyre, V., et al., *Electrocatalytic investigation of light-induced electron transfer between cytochrome c(6) and photosystem I.* Journal of the American Chemical Society, 2003. **125**(45): p. 13686-13692.

15. Terasaki, N., et al., *Fabrication of novel photosystem I-gold nanoparticle hybrids and their photocurrent enhancement.* Thin Solid Films, 2006. **499**(1-2): p. 153-156.

16. Terasaki, N., et al., *Plugging a Molecular Wire into Photosystem I: Reconstitution of the Photoelectric Conversion System on a Gold Electrode.* Angewandte Chemie-International Edition, 2009. **48**(9): p. 1585-1587.

17. Terasaki, N., et al., *Photosensor Based on an FET Utilizing a Biocomponent of Photosystem I for Use in Imaging Devices.* Langmuir, 2009. **25**(19): p. 11969-11974.

18. Terasaki, N., et al., *Bio-photo sensor: Cyanobacterial photosystem I coupled with transistor via molecular wire.* Biochimica Et Biophysica Acta-Bioenergetics, 2007. **1767**(6): p. 653-659.

19. Frolov, L., et al., *Fabrication of a photoelectronic device by direct chemical binding of the photosynthetic reaction center protein to metal surfaces.* Advanced Materials, 2005. **17**(20): p. 2434-+.

20. Das, R., et al., *Integration of photosynthetic protein molecular complexes in solid-state electronic devices.* Nano Letters, 2004. **4**(6): p. 1079-1083.

21. Frolov, L., et al., *Fabrication of oriented multilayers of photosystem I proteins on solid surfaces by auto-metallization.* Advanced Materials, 2008. **20**(2): p. 263-+.

22. Frolov, L., et al., *Photoelectric junctions between GaAs and photosynthetic reaction center protein.* Journal of Physical Chemistry C, 2008. **112**(35): p. 13426-13430.

23. Ko, B.S., et al., *Effect of surface composition on the adsorption of photosystem I onto alkanethiolate self-assembled monolayers on gold.* Langmuir, 2004. **20**(10): p. 4033-4038.

24. Kincaid, H.A., et al., *Entrapment of Photosystem I within Self-Assembled Films.* Langmuir, 2006. **22**(19): p. 8114-8120.

25. Ciobanu, M., et al., *Photosystem I Patterning Imaged by Scanning Electrochemical Microscopy.* Langmuir, 2005. **21**: p. 692-698.

26. Ciobanu, M., et al., *Electrochemistry and photoelectrochemistry of photosystem I adsorbed on hydroxyl-terminated monolayers.* Journal of Electroanalytical Chemistry, 2007. **599**(1): p. 72-78.

27. Faulkner, C.J., et al., *Rapid Assembly of Photosystem I Monolayers on Gold Electrodes.* Langmuir, 2008. **24**(16): p. 8409-8412.

28. Ragauskas, A.J., et al., *The Path Forward for Biofuels and Biomaterials.* Science, 2006. **311**(5760): p. 484-489.

CHAPTER II

EXPERIMENTAL AND ANALYTICAL METHODS

Introduction

In order to thoroughly characterize the biohybrid systems discussed in this work, experimental techniques and analytical methods from various of disciplines were employed. The studies presented in subsequent chapters are predominantly electrochemical investigations, but additional tools including optical spectroscopy, electron microscopy, and numerical simulation were used to provide a more comprehensive understanding of the systems' geometry, composition, and behavior under various conditions. While details pertaining to specific experiments and analyses are included in the subsequent chapters in which the data are presented, this chapter introduces the methods in general with a focus on aspects most pertinent to the experiments performed in this thesis, and discusses the underlying theory by which the experimental results may be interpreted and formulated into conclusions.

Analytical Electrochemistry

Photochronoamperometry

Perhaps the most obvious evidence of the photocatalytic role of PSI films in electrochemical systems is offered by photochronoamperometry, which has caused this technique to play a central role in studies of PSI-based systems. This method is variation of chronoamperometry, in which a constant potential is applied to the working electrode

and the resulting current density is measured as time progresses. During a photochronoamperometric experiment, the light conditions to which the electrode surface is exposed are varied throughout the course of the experiment. These variations can be caused by changing the intensity of the light irradiating the sample, modifying the emission spectrum of a polychromatic light source using a filter, or by changing the wavelength of a monochromatic light source. If the electrochemical system of interest contains components that participate in photoinitiated heterogeneous redox reactions, the variations in current density will be measured in response to the changes in irradiation. Photochronoampermetric experiments presented in this work were performed using two configurations. The most common are those performed using a 3-electrode cell (shown schematically in **Figure 2.1**) with the PSI modified electrode as the working electrode, an Ag/AgCl reference electrode, and a platinum mesh counter electrode. This configuration was used to collect the photochronoampermetric data presented in Chapters 3, 4, and 6. The second configuration, which was used to measure the photocurrent responses of the complete photoelectrochemical cell reported in chapter 5, entails clipping the working electrode lead to the cathode of the device (i.e. the PSI-modified electrode in the case of the device in Chapter 5) and clipping both the counter electrode and reference electrode leads to the anode. This configuration allows the measurement of the short-circuit current produced by a device by setting the potential between the working and reference electrodes to zero.

For an electrochemical system in which current is produced by reversible, single-electron transfer events between a redox couple and the electrode surface, the net current

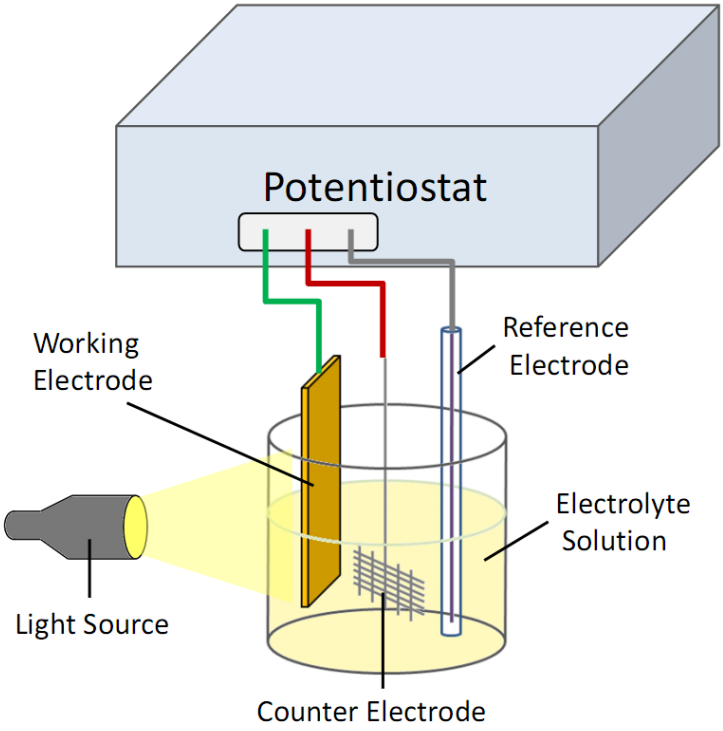

Figure 2.1. Schematic of a Three-Electrode Electrochemical Cell used for Photochrono-amperometric and Photochonopotentiometric Experiments. All three electrodes are immersed in an electrolyte solution, and the PSI-modified working electrode is subjected to variations in irradiation as the current or voltage is measured. This three-electrode configuration was also used for cyclic voltammetry and electrochemical impedance spectroscopy.

produced from this reaction at time *t* is proportional to the difference of the rates of reduction and oxidation as

$$i_{net}(t) = FA\left[k_{red}C_O(0,t) - k_{ox}C_R(0,t)\right] \quad (1)$$

where *F* is the Faraday constant, *A* is the area of the electrode, $C_O(0,t)$ and $C_R(0,t)$ are the respective concentrations of the oxidized and reduced form of the redox couple at the electrode surface, and k_{red} and k_{ox} are the heterogeneous rate constants for the reduction and oxidation reactions, respectively. The case of completely diffusion-limited current production was described by Cottrell[1] by solving Fick's second law for the diffusion of the heterogeneous reactant to the electrode surface and assuming boundary conditions wherein the concentration of the heterogeneous reactant was equal to zero at the electrode surface (i.e. x = 0) and remained equal to the bulk concentration far away from the electrode surface (i.e. x = ∞). These assumptions allow an analytical solution to be obtained via Laplace transform from which a current-time relationship is derived, called the Cotrell Equation:

$$i = nFAC^*\left(\frac{D}{\pi t}\right)^{\frac{1}{2}} \quad (2)$$

where *n* is the number of electrons transferred, and *D* and *C** are the diffusion coefficient and bulk concentration of the redox couple, respectively. This relationship predicts that the current density will decrease with $t^{-1/2}$ for a diffusion-limited heterogeneous reaction in an unstirred electrolyte solution. While the majority of the photochronoamperometric experiments presented in this work are not completely diffusion limited, all display a similar time-decay in current density due to the propagation of concentration gradients

from the electrode surface as the mobile redox couple reacts at the electrode/electrolyte interface.

Responses of current density to irradiation can manifest in several ways. For example, consider an electrode to which a negative overpotential is applied, in which overpotential is defined as $\eta = E_W - E_{eq}$, where η is the overpotential, E_w is the potential applied to the working electrode, and E_{eq} is the equilibrium potential. The negative overpotential prompts the heterogeneous reduction of the redox couple which is observed as cathodic current, reported positive by convention. If irradiation of the electrode causes an increase in cathodic current, this denotes that the frequency of heterogeneous reduction events has increased, or that the frequency of heterogeneous oxidation events has decreased. For a PSI-modified electrode, this effect can be observed when the reaction centers of adsorbed PSI complexes are reduced, or when the flux of the oxidized form of the redox couple at the electrode surface increase due to the activity of PSI complexes in a multilayer film. Conversely, a decrease in current density in response to irradiation when the electrode is held at a negative overpotential indicates a decrease in the rate of reduction events or an increase in the rate of oxidation. I have observed such decreases in PSI-multilayer system at a negative overpotential when only the oxidized form of a redox couple was present in the electrolyte. When the electrode was irradiated, PSI complexes in the multilayer consume the heterogeneous reactant by reducing it within the film, which decreases the concentration of the reactant at the electrode surface.

Of critical importance to a photochronoamperometric experiment is the wavelength of the light used to irradiate the sample. Photoelectrochemical responses typically arise from the transfer of electrons that have been photoexcited by some

mechanism across the electrode/electrolyte interface, and the transition of electrons from the ground state to specific excited states in pigments such as chlorophyll are initiated by photons of specific energy. Thus, irradiating the system with light of various wavelengths allows for the investigation of heterogeneous electron transfer events that result from the different electronic transitions of the photoactive species in the system. In addition, control over the wavelength of the radiation allows only certain excitations to occur, such as those exhibited by the analyte in question, and to avoid unwanted electronic transitions such as those that may occur in solvent molecules or electrochemical mediators. By measuring the photocurrent responses to various wavelengths, a "photocurrent action spectrum" is obtained. Comparing this action spectrum to the absorption spectrum of the system allows for the assignment of photocurrent to the various system components. For example, if the photocurrent action spectrum follows the absorption spectrum of the redox couple in the electrolyte rather than the absorption spectrum of photoactive pigments in the system, one infers that the majority of the photocurrent produced by the system could be attributed to photoexcitation of the redox couple.

Photochronopotentiometry

Photochronopotentiometry, like photochronoamperometry, involves measuring an electrochemical parameter during periods of varying irradiation, but instead of applying a potential and measuring the current, a constant current is applied and the potential is measured. In an electrochemical system, the electrode potential is related to the surface concentrations of the redox couple by the Nernst equation:

$$E(t) = E^{0'} + \frac{RT}{F} \ln \frac{C_O(0,t)}{C_R(0,t)} \quad (3)$$

where $E^{0'}$ is the formal potential of the working electrode at standard conditions, and $C_O(0,t)$ and $C_R(0,t)$ are the respective concentrations of the oxidized and reduced forms of the mediator at any time t and position $x = 0$, where the system geometry is defined such that $x = 0$ at the electrode surface and increases in the direction of the surface normal. If a zero net current is applied during a photochronopotentiometric experiment, the equilibrium potential of the system is measured. Since there is no net heterogeneous charge transfer under these conditions, photoinduced changes in the measured potential imply that the surface concentrations of the redox couple have changed. For example, if an increase in the equilibrium potential is observed in response to irradiation, equation (3) indicates that the surface concentration of the oxidized form of the redox couple has increased. Such an effect has been observed for PSI multilayer films, wherein photoinduced redox reactions between the reaction centers of the PSI in the film and the redox couple result in a net change of the concentrations of the reduced and oxidized forms of the redox couple near the electrode surface.

Cyclic Voltammetry

Cyclic voltammetry is a potential sweep method in which the potential applied to the working electrode is varied with time while measuring the current. Typically, the potential is varied from an initial potential, E_i, to a final potential, E_f, and then returned to the initial potential E_i, hence the term "cyclic." If the system in question contains a redox couple whose formal potential is between E_i and E_f, peaks in the measured current will be

observed. For example, if $E_i < E_f$, the oxidation of the redox couple, measured as anodic current, will be observed during the forward scan, and reduction of the redox couple, measured as cathodic current, is observed during the reverse scan. Expressions for the potential dependence of the rates of a redox couple undergoing one-step, single-electron transfer reactions of the form $O + e^- \longleftrightarrow R$ at an electrode surface were developed by Butler and Volmer.[2] These expressions are given by

$$r_f = k^0 \exp\left[-\alpha\ f\left(E - E^{0'}\right)\right] C_O(0,t) \tag{4}$$

for reduction of the redox couple and

$$r_b = k^0 \exp\left[(1-\alpha\ ) f\left(E - E^{0'}\right)\right] C_R(0,t) \tag{5}$$

for the oxidation of the redox couple, where r_f and r_b are the rates of reduction and oxidation, respectively[a], f is defined as F/RT where F is Faraday's constant, R is the gas constant, T is the absolute temperature, E is the applied potential, and α, k^0, and $E^{0'}$ are the transfer coefficient, standard rate constant, and formal potential of the redox couple, respectively. As the working electrode potential approaches the formal potential of the redox couple, the rate of electron transfer between the electrode and the redox couple will increase because the thermodynamic driving force for the heterogeneous reaction supplied by the electrode is also increasing. As the electrode continues past the formal potential of the redox couple, the reaction rate continues to increase until the reaction becomes diffusion-limited, at which point a peak in the current is observed due to the depletion of heterogeneous reactant in the vicinity of the electrode. The boundary value solution to Fick's law for a totally reversible redox couple has been solved numerically

[a] The reduction and oxidation reactions are often referred to as "forward" and "backward" reactions, respectively, hence the subscripts on the reaction rates.

(see Chapter 6 of Bard and Faulkner[3] for a discussion of the solution) to yield the following expression for the peak current, i_p, measured during a cathodic potential sweep:

$$i_p = (2.69 \times 10^5) n^{3/2} A D_O^{1/2} C_O^* v^{1/2} \quad (6)$$

where n is the number of electrons transferred, v is the scan rate, and D_O and C^* are the diffusion coefficient and bulk concentration of the of the redox couple, respectively. This equation is useful for back calculating unknown parameters in a system from cyclic voltammograms. The photocatalytic effect of a PSI multilayer is demonstrated via cyclic voltammetry in Chapter 6, in which higher peak currents are observed when light is shone on the electrode, and the results are interpreted in the context of equation (6).

Electrochemical Impedance Spectroscopy

Electrochemical impedance spectroscopy, or EIS, is a technique in which the applied potential is modulated by a small magnitude about the equilibrium potential over a range of frequencies and the corresponding impedance is measured. The results are compared to equivalent circuits depicting physical aspects of the electrochemical system in question, such as the solution resistance, double layer capacitance, and charge transfer resistance. The utility of this technique arises from the fact that the contributions to the impedance by these electrochemical phenomena vary across different frequency regimes, which allows them to be decoupled. At high frequencies (ca. > 10^5 Hz), the solution resistance of the electrolyte dominates the impedance. At low frequencies (ca. 10^{-1} - 10^2 Hz), impedances associated with the transfer of charge across the electrode/electrolyte interface can be investigated if the heterogeneous reaction is limited by charge transfer

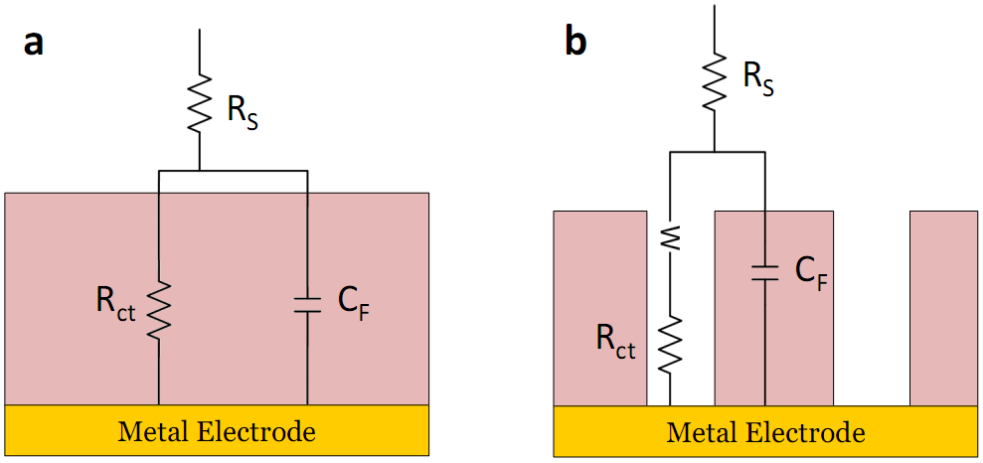

Figure 2.2. Equivalent Circuit Diagrams used in Electrochemical Impedance Spectroscopy. (a) A typical Randle's circuit includes a solution resistance, denoted R_S, a film capacitance, C_F, and a charge transfer resistance, R_{ct}, that accounts for the film resistance, interfacial charge transfer resistance, and interfacial double-layer capacitance. **(b)** A mixed kinetic and charge transfer equivalent circuit includes a Warburg impedance to account for frequency regimes in which charge transfer is limited by diffusion of the redox couple, often through defects in a film.

kinetics. Furthermore, if the electrode is modified by a film, impedances to faradaic current imparted by the film are also measured at low frequencies. Impedances at intermediate frequencies are typically associated with charging of the electric double layer. Electrochemical systems in which the faradaic processes are limited by semi-infinite diffusion rather than charge-transfer kinetics exhibit a Warburg impedance. Impedances that arise from electrochemical phenomena that are analogous to certain types of circuit elements produce a phase shift in the current signal in the frequency domain with respect to the potential modulation, which provides an additional means for contributions to the electrochemical impedance to be differentiated. Impedances behaving as ideal capacitors cause the current signal to lag behind the voltage signal by 90°, while those that behave as resistors produce a current that is in phase with the

potential. In Chapter 3, EIS is used to investigate the modification of nanoporous gold electrodes by various SAMs.

Scanning Electron Microscopy

In scanning electron microscopy (SEM), a focused beam of electrons is rastered across a sample in vacuum and an image is obtained by collecting electrons that are scattered by the sample. Electron microscopy can be used to resolve features much smaller than those resolved by optical spectroscopy because the wavelength of the electrons used to image the sample can have wavelengths much smaller than that of visible light. The wavelength of the electrons is controlled by the voltage at which they are accelerated towards the sample; thus, higher accelerating voltages produce electrons of shorter wavelength, which allows for the resolution of smaller features. Electrons emitted from the source, called primary electrons before reaching the sample, undergo several types of interactions with the sample that contribute to the image recorded by the detector. Electrons that reach the sample can be scattered by elastic and/or inelastic collisions by electrons in atomic or molecular orbitals, and primary electrons can also be scattered by elastic collisions with atomic nuclei. Electrons that lose little or no energy during their collisions with the sample are likely to escape to the sample and reach the detector, while those that lose a large portion of their kinetic energy via an elastic collision will remain in the sample. By convention, scattered electrons with energies < 50 eV are referred to as secondary electrons and are produced by collisions within the first few nanometers of the surface of the sample, while scattered electrons with energies > 50 eV are called backscattered electrons and typically result from inelastic collisions with

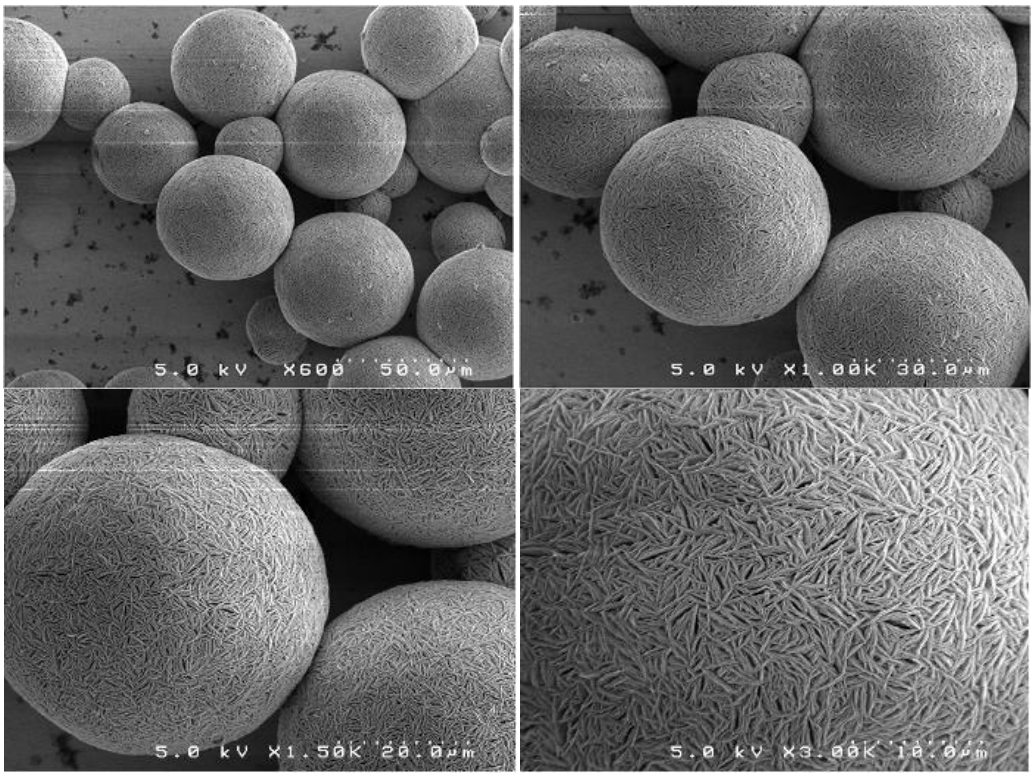

Figure 2.3. Representative SEM Images. SEM images of the surface of dissembled cell fabricated as described in Chapter 5 reveal the nanoscale texture of the microscale agglomerates that deposited on the cathode.

atomic nuclei and have energies comparable to that of the primary electrons.[4] Bright regions in an SEM image correspond to regions of the sample that produce more scattered electrons that reach the detector relative to a darker region from which fewer scattered electrons are emitted to the detector. This contrast can arise from several characteristics of the sample. A material composed of atoms with a relatively high atomic number appears brighter than a material composed of smaller atoms because the larger atomic nuclei scatter more electrons to the detector. Furthermore, a material with a heterogeneous distribution of atoms of differing atomic numbers, such as a composite material or multiphase alloy, can also display variations in contrast because areas of higher relative atomic density will scatter more electrons than areas of relatively sparse

atomic distribution. Differences in the surface geometry of materials of identical composition can also cause variations in contrast. For example, in the cross section SEM image of a nanoporous gold film on a nonporous gold substrate shown in Figure 3.3 in Chapter 3, the nanoporous gold appears significantly brighter than the nonporous substrate because the high surface area imparted by the porosity allows more secondary electrons to escape the solid.

Scanning Probe Techniques

Atomic Force Microscopy

Atomic force microscopy, or AFM, is a scanning probe technique in which a sharp tip on the end of a cantilever is scanned over a substrate, and forces between the substrate and the tip are measured by monitoring the deflection of the cantilever. This technique can provide information about the topography of the sample on the scale of a few microns down to several nanometers and can even provide atomic resolution in some cases. An AFM provides a basic advantage over other hghi-resolution imaging techniques such as scanning tunneling microscopy in that the sample does not need to be electronically conductive, which allows the application of AFM to biological systems and other systems composed primarily of insulating materials such as glasses and ceramics. There are several modes in which an AFM is commonly operated: contact mode, tapping mode, and phase mode. In contact mode, the tip remains in contact with the sample as it is scanned over the surface, and the topography is measured directly by monitoring the beam deflection. During tapping mode (sometimes called dynamic force mode), the cantilever is oscillated such that it occasionally contacts the sample, hence the term

"tapping." This method nearly eliminates frictional forces associated with lateral movement of the tip and can provide improved resolution on rough samples or substrates on which the features of interest are weakly attached and prone to being pushed or dragged by the tip. Phase mode is similar to tapping mode in that the tip is oscillated during data collection; however, the phase shift of the oscillation frequency with respect to that of the oscillation driving force is measured. Another variation of AFM, called Kelvin Force Probe Microscopy (KFPM), uses a conductive tip to measure variations in the electric field at the surface of a sample. This method has been employed by Frolov and coworkers to measure the photovoltage produced by monolayers[5] and multilayers[6] of PSI complexes. In this thesis, tapping mode AFM is employed to characterize the topography of the surface of the PSI multilayer on the cathode of the photoelectrochemical device presented in Chapter 5.

Profilometry

Profilometry is similar to contact mode AFM but is used to measure features on the order of tens of nanometers to hundreds of microns. The technique also employs a tip on the end of a cantilever and uses variations in the cantilever deflection to determine the topography of the sample as the tip is scanned. Unlike AFM in which the tip is rastered across the sample to produce a 3-dimensional image of the topography of the surface, profilometry is usually used to perform single line scans. In this thesis, profilometry was used to measure the thickness of PSI multilayer films in Chapters 5 and 6 by measuring the change in height when the tip was scanned from the bare substrate proceeding into the film.

Optical Spectroscopy

UV-Absorbance Spectroscopy

Absorbance of photons with wavelengths in the UV and visible range can often promote electrons in molecular or atomic orbitals of the absorbing material to excited states. The energies of both the ground state and excited state are specific to the system in which they are observed; hence, the energy supplied by the absorbed photon that is required to initiate the electronic transition is also specific. Varying the wavelength of the photons irradiating the system and measuring the absorbance of these photons provides information about the electronic transitions allowed by the system in question. Absorbance, $A(\lambda)$, is defined as

$$A(\lambda) = -\log_{10}\left(\frac{I(\lambda)}{I_0(\lambda)}\right) \tag{7}$$

where $I_0(\lambda)$ is the intensity of light of wavelength λ before passing through the sample, and $I(\lambda)$ is the intensity after passing through the sample. According to the Beer-Lambert law, absorbance is related to the concentration of the absorbing molecules as well as the optical path length by

$$A = \varepsilon bc, \tag{8}$$

where ε and c are the molar extinction coefficient and concentration of the absorbing pigment, respectively, and b is the optical path length. These relationships can be used to calculate the concentration of absorbing molecules in a solution or film. Some photoinitiated electronic transitions, such as that displayed by the P_{700} reaction center of PSI, result in a change in the oxidation state of the absorbing pigment(s), which subsequently changes the absorbance spectrum of the sample. These phenomena have

given rise to a technique referred to as differential absorbance spectroscopy, which has been applied extensively to spectroscopically elucidate the mechanisms of photosynthesis (see Schlodder, 2009[7] for an informative review of these methods). Differential absorbance spectroscopy was used to calculate the concentrations of P_{700} reaction centers in the PSI preparations used in this work, and the Beer-Lambert law was employed in Chapter 6 to back-calculate an extinction coefficient of PSI complexes in vacuum-assembled multilayer films.

Infrared Absorption Spectroscopy

Infrared (IR) absorption spectroscopy is used to investigate the types of bonds and functional groups present in a sample that contains organic molecules. Vibrational modes of the covalent bonds of organic molecules may be excited by the absorption infrared photons, and the energy of the absorbed photon corresponds to the specific type of bond and vibrational mode excited. Hence, varying the wavelength of the photons across the IR spectrum and measuring the absorbance of the sample provides information about which types of bonds are present. IR spectroscopy can be extended to films of organic molecules on reflective substrates by allowing the beam to reflect off the substrate at a glancing angle. This technique, called reflectance-absorption infrared spectroscopy (RAIRS), probes vibrational modes that give rise to electronic dipoles that oscillate in a direction parallel to the surface normal. In this thesis, RAIRS was used to detect protein adsorbed on metallic surfaces by monitoring Amide I and II absorption bands typical of proteins observed at ca. 1667 and 1546 cm^{-1}, respectively. The Amide I bond is attributed to stretching of C=O bonds, and the Amide II band is assigned to

bending of N-H bonds.[8] These absorption bands can be further deconvoluted into contributions from β sheets, β turns, α helices, and unordered helices, which provides additional information regarding the secondary structure of the absorbing protein.[9]

Photosystem I Extraction and Purification

The process of extraction of PSI complexes from spinach used in this thesis essentially consists of two general steps: the extraction of thylakoid membranes from the spinach leaves and the isolation and purification of PSI complexes from the thylakoids. Thylakoids were extracted via maceration and centrifugation using the methods of Reeves and Hall[10] with several adaptations,[11] and the isolation and purification of PSI complexes from the thylakoids was accomplished by additional centrifugation, column chromatography by the methods of Baba *et al.*[12] and Shiozawa *et al.*,[13] and dialysis. This process is shown schematically in **Figure 2.4**. First, spinach purchased from a local grocery store (I usually bought organic baby spinach from Sam's Club) is deveined using a scalpel. I usually cut ~ 10% more than the extraction procedure requires in an effort to maximize the final yield. After this tedious process, the cut spinach is further macerated in a blender with a grinding buffer. The ground up spinach/buffer mixture is then subjected to several filtering steps through cheese cloth, and the filtrate is collected in centrifuge tubes. The pellet resulting from the initial centrifugation step contains the thylakoids, and the supernatant is discarded. The pellet is re-suspended and subjected to a second centrifugation step that forces the thylakoid membranes and other unwanted proteins into the pellet, while PSI particles remain in

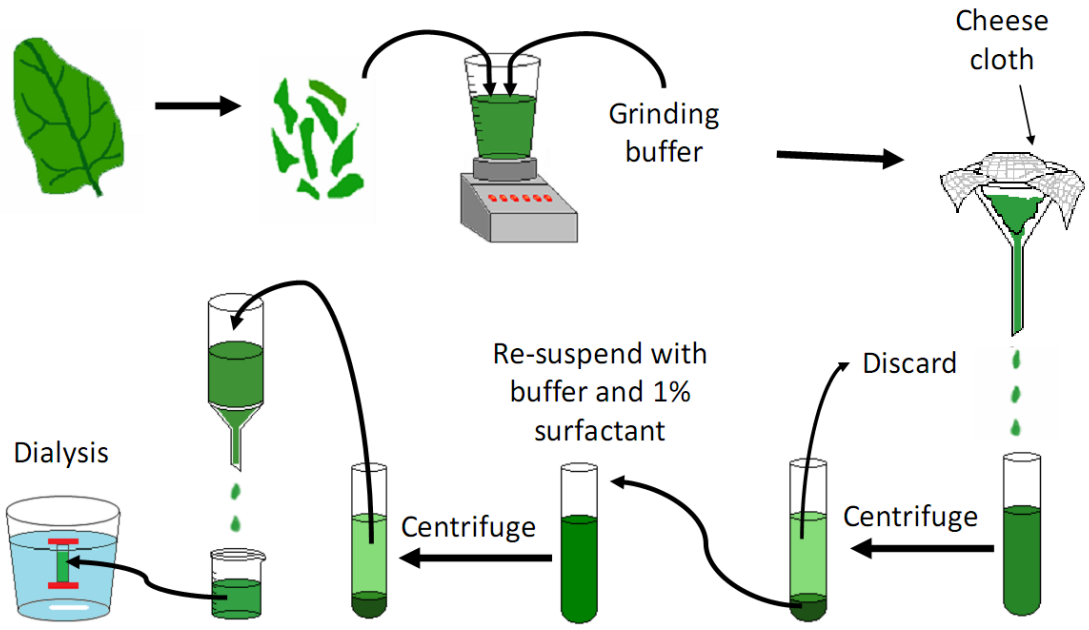

Figure 2.4. Photosystem I Extraction Procedure.

solution. This solution is then loaded onto a hydroxylapatite chromatography column. Hydroxylapatite contains both negatively charged phosphate groups and positively charged calcium-containing groups that interact electrostatically with charged and dipolar groups, mainly amine and carboxyl groups found on the protein. Once the spinach extract is loaded on the column, it is rinsed with a buffer of low ionic strength. During this period, PSI binds to the column and this process can be observed as the hydroxylapatite gel changes from white to green. The column is continually washed with buffer until the effluent is clear, at which point the column has been saturated with PSI complexes and appears uniformly emerald green. To elute the bound PSI, the column is washed with a buffer of high ionic strength which causes ions in the buffer to out-compete PSI for the electrostatic binding interactions on the hydroxylapatite. This effluent is collected and stored in a -80 C freezer. The final purification step, dialysis,

was adopted in approximately August of 2009, and substantially reduced the concentrations of salt and surfactant in the PSI preparation. This procedure consists of placing 1-2 mL of the PSI suspension, which is still in the elution buffer, into a section of dialysis tubing, and the tubing is clamped shut at either end. The tubing is then placed in a container of deionized water and stirred gently for ~ 24 h. During this process, the salt and surfactant molecules migrate through the tubing, essentially diluting the concentration of these components to the volume of the container in which dialysis is performed. The reduction of these concentrations allows for the formation of thick, dense, PSI multilayers that are not water soluble as described in Chapter 6.

Numerical Methods and Matlab Simulation

A kinetic model for the photocatalytic effect of a PSI monolayer is presented in Chapter 4 of this thesis, where the electrochemical theory upon which the model is based is discussed in great detail; however, the numerical methods and computational algorithms employed in order to solve the derived system of partial differential equations (PDEs) and subsequently extract parameters from experimental data are non-trivial, and such will be the focus of this section. The PDEs presented in Chapter 4 define an initial-boundary value problem of one space variable and one time variable, and as such are suitable for Matlab's pde solver function called `pdepe`. This function has five essential inputs: `pdefun`, a function that defines the components of the PDE and how they are related, `icfun`, a function that defines and evaluates the initial conditions, `bcfun`, a function that defines and evaluates the boundary conditions, `xmesh`, a vector specifying

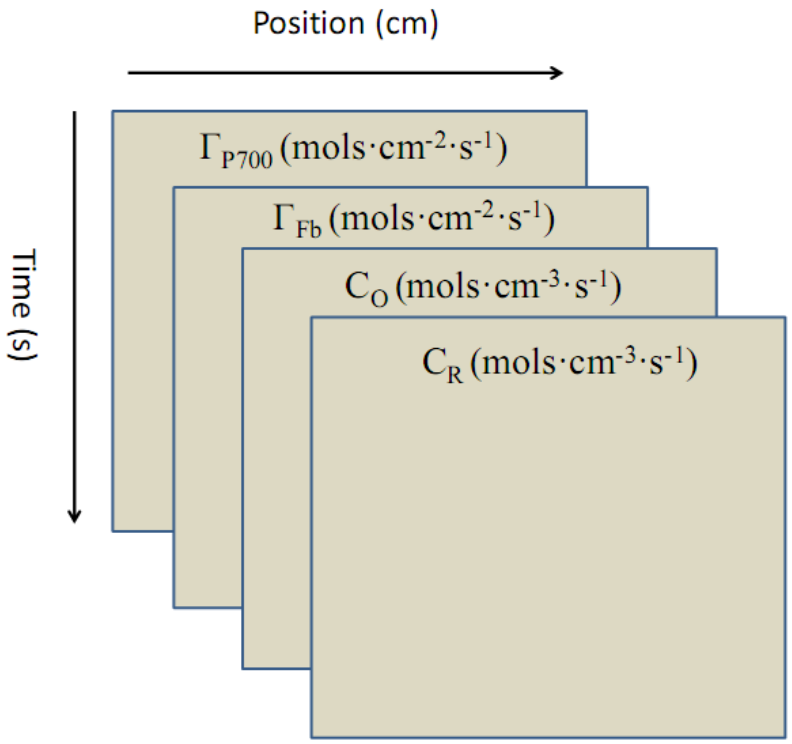

Figure 2.5. Data Structure of the Solution Produced by `pdepe` for the Simulation in Chapter 4. The solution returned by the function is a 3-dimensional matrix that contains a value for each concentration of interest at every requested time and space value.

the points at which a numerical solution is requested for every value in `tspan`, and `tspan`, a vector specifying the points at which a solution is requested for every value in `xmesh`. Each of the functional inputs to the PDE solver must be defined as individual functions, and they are called by the solver function iteratively as it converges on a solution. For example, for the simulation presented in Chapter 4, the function `bcfun` contains the heterogeneous reaction rate expressions (i.e. the boundary conditions at x = 0) and is called by the solver to evaluate the rate expressions for each point in time at which the solution is requested. The solution produced by the solver is a three-dimensional matrix that describes the value of interest for each position in `xmesh` and at

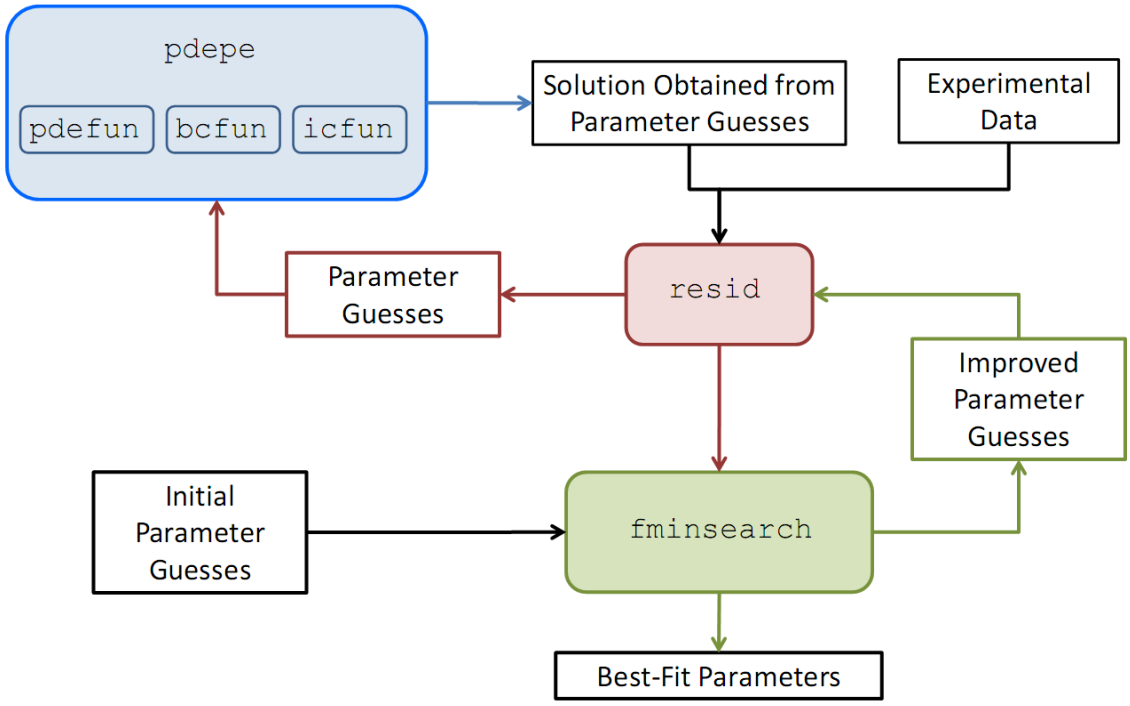

Figure 2.6. Program Flowchart for the Custom Parameter Extraction Algorithm. Initial guesses for the model parameters are supplied to the minimizing function, `fminsearch`. The minimizing function then calls the function `resid` which passes the guesses supplied by `fminsearch` to the pde solver `pdepe`. The solver numerically solves the system using the parameter guesses and returns the output to `resid` which back-calculates a current density and calculates the residual between the simulated and experimental current densities. This residual is passed back to `fminsearch`, which generates new guesses in an attempt to minimize the output of `resid`. The process continues until the parameter guesses are obtained that provide the lowest residual between the simulated and experimental current densities, and these parameters are returned as the parameters of best fit.

each time in `tspan` (**Figure 2.5**). Since the current measured in a chronoamperometric experiment is only dependent upon the surface concentrations of the redox couples, the current was back calculated from the values of the solution at $x = 0$. Once a simulated current density was calculated, it was compared to experimental data using a custom fitting routine that iteratively varies the parameters in the simulation to minimize the difference between the current density predicted by the simulation and that measured

experimentally at corresponding conditions. This approach consisted of defining a function, which we will call `resid`, to calculate the least-squares difference between the experimental and simulated current densities, and using Matlab's minimizing function `fminsearch` to minimize the value of `resid` by varying the model parameters. I learned how to implement this extremely useful coding strategy from Brad Reisfeld, who is presently an assistant professor in the Chemical and Biological Engineering Department at Colorado State University. This technique is shown schematically in **Figure 2.6**. While this approach is quite robust, it can be extremely sensitive to initial guesses, especially when fitting multiple parameters simultaneously, because the residual function often exhibits many local minima. For the application described in Chapter 4, this technique was very computationally intensive because the entire system of PDE's was solved numerically for each iteration of the minimizing function; however, the approach was eventually successful as demonstrated later in this thesis. The power of this technique lies in its generality. While many parameter extraction packages minimize residuals between experimental data and algebraic models, the form of the simulation required by the fitting algorithm described in this section is arbitrary as long as it produces output that can be compared to experimental data. This characteristic allows for extension of the algorithm to much more complex models, even those consisting of systems of equations that do not have an analytical solution such as the PDE system derived in Chapter 4.

Works Cited

1. Cottrell, F.G., Z.Physik.Chem, 1902, **42**: p. 385-431.

2. Butler, J.A.V., *Studies in heterogeneous equilibria. Part II.—The kinetic interpretation of the Nernst theory of electromotive force.* Transactions of the Faraday Society 1924. **19**: p. 729, 734.

3. Bard, A.J. and L.R. Faulkner, *Electrochemical Methods: Fundamentals and Applications*. 2nd ed. 2001, New York: Wiley

4. Brundle, C.R., C.A.J. Evancs, and S. Wilson, eds. *Encyclopedia of Materials Characterization*. 1992, Butterworh-Heinemann: Stoneham, MA.

5. Frolov, L., et al., *Fabrication of a photoelectronic device by direct chemical binding of the photosynthetic reaction center protein to metal surfaces.* Advanced Materials, 2005. **17**(20): p. 2434-+.

6. Frolov, L., et al., *Fabrication of oriented multilayers of photosystem I proteins on solid surfaces by auto-metallization.* Advanced Materials, 2008. **20**(2): p. 263-+.

7. Schlodder, E., *Introduction to optical methods in photosynthesis.* Photosynthesis Research, 2009. **101**(2-3): p. 93-104.

8. Siverstein, R.M., G.C. Bassler, and T.C. Morrill, *Spectroscopic Identification of Organic Compounds*. 4th ed. 1981: John Wiley & Sons.

9. Kincaid, H.A., et al., *Entrapment of Photosystem I within Self-Assembled Films.* Langmuir, 2006. **22**(19): p. 8114-8120.

10. Reeves, S.G. and D.O. Hall, *Higher Plant Chloroplasts and Grana: General Preparative Procedures (Excluding High Carbon Dioxide Fixation Ability Chloroplasts).* Methods in Enzymology, 1980. **69**: p. 85-94.

11. Ciobanu, M., et al., *Photosystem I Patterning Imaged by Scanning Electrochemical Microscopy.* Langmuir, 2005. **21**: p. 692-698.

12. Baba, K., et al., *Photoinhibition of photosystem I electron transfer activity in isolated photosystem I preparations with different chlorophyll contents.* Photosynthesis Research, 1996. **47**(2): p. 121-130.

13. Shiozawa, J.A., R.S. Alberte, and J.P. Thornber, *P700-Chlorophyll a-Protein - Isolation and Some Characteristics of Complex in Higher Plants.* Archives of Biochemistry and Biophysics, 1974. **165**(1): p. 388-397.

14. Porra, R.J., *The chequered history of the development and use of simultaneous equations for the accurate determination of chlorophylls a and b.* Photosynthesis Research, 2002. **73**(1-3): p. 149-156.

CHAPTER III

FUNCTIONALIZED NANOPOROUS GOLD LEAF ELECTRODE FILMS FOR THE IMMOBILIZATION OF PHOTOSYSTEM I

Introduction

Recent studies have successfully demonstrated that the remarkable functionality of Photosystem I can be accessed in both solid-state nanoelectronic[1-5] and "wet" photo-electrochemical devices.[6, 7] Gold surfaces are ideal substrates for the bottom-up assembly of such devices, particularly in electrochemical applications, because of gold's broad potential window and the ease by which it is modified with various ω-terminated alkyl thiols to provide a versatile array of functional surfaces. Previous investigations have demonstrated how careful selection of the terminal functional groups of self-assembled monolayers (SAMs) on gold can be used to tune the surface energy,[8] provide a substrate for biological macromolecules[9, 10], or serve as polymerization initiators.[11-13] For many of these applications, including photoelectrochemical cells, the performance of thin films can be favorably altered by translation from a flat, two-dimensional surface to a three-dimensional architecture with nanoscale features[14], which can both increase the available surface area and add infrastructure to the system. Several routes to achieve such surfaces patterned with columns[15, 16], tubes[17], and pores[18] have been described previously; for applications where uniform features are not required, but a high surface area is still desirable, gold nanoparticles can be deposited.[6, 19] An alternative to the aforementioned techniques is offered by nanoporous gold leaf (NPGL), a free standing mesoporous thin film that results from

selectively dissolving silver atoms from commercially available Ag-Au alloyed leaf in concentrated nitric acid.[20] This fabrication process is ideal for many applications because it efficiently incorporates inexpensive materials that are convenient for re-scaling, and it can be performed under ambient conditions without the need for sophisticated processing equipment.[21]

In this chapter we report the fabrication and characterization of electrode films in which NPGL is attached to planar gold and glass supports. The resulting NPGL electrode films are ultimately intended to provide a substrate for the attachment of PSI to impart photonic energy conversion capabilities to the electrode, and the surface area enhancement provided by the mesoporous network of the NPGL is expected to accommodate a greater number of PSI complexes per geometric area then a planar electrode. Previously, Terasaki *et al.* have demonstrated that a high surface area electrode prepared by gold nanoparticle deposition allowed a higher number density of PSI complexes on the electrode surface, resulting in an increased photocurrent response when compared to a planar electrode in the same electrochemical system.[6] NPGL electrode films provide several advantages to nanoparticle aggregate electrodes in that they provide better lateral conductivity and offer more control over feature size which allows for a greater percentage of the electrode surface area to be made accessible to both PSI and the external circuit. Here, we report a PSI-catalyzed photocurrent enhancement contributed by an increase in PSI/electrode interfacial area, and present evidence of the successful integration of functional PSI complexes into a scalable NPGL architecture fabricated from a material that costs ~ 6 cents/cm^2 of geometric surface area.

Nanoporous Gold Leaf Electrode Fabrication

We have developed a simple electrode fabrication scheme (**Figure 3.1**) with several adaptations to the technique developed by Ding *et al.* that makes use of a graphite roller.[20] First, the as-received gold/silver leaf was cut into portions slightly larger than the final desired sample size to allow the NPGL to completely cover the substrate surface. Next, tweezers were used to gently place the leaf on a glass microscope slide, and the slide was slowly dipped into a beaker of concentrated nitric acid (Figure 3.1a). As the leaf floated freely on the surface of the acid (Figure 3.1b), the glass slide was removed. After the dealloying had proceeded for the desired time, the leaf was removed from the acid with a glass slide by first dipping the slide into the beaker at an angle approximately 20° from the surface normal, extending it beneath the NPGL, and then gently withdrawing it. As the slide was removed, the free-floating leaf adhered smoothly to the surface (Figure 3.1c), and it was then transferred to a beaker of deionized water (Figure 3.1d) where it was again floated for rinsing. The leaf was removed from the air-water interface with a pre-cut portion of a gold-coated silicon wafer (Figure 3.1e) that was pre-modified with 1,6-hexanedithiol; as the sample was left to dry, the free thiols on the surface of the SAM bonded to the NPGL surface, fastening it firmly to the planar gold substrate (Figure 3.1f). This technique was adapted to attach NPGL to glass surfaces as well; the attachment was achieved by using a glass slide modified with 3-mercaptopropyl trimethoxysilane to remove the NPGL from the air-water interface (Figure 3.1g and e) after the rinsing step. In both cases, evidence of the adhesion to the substrate was visually observable and appeared as a front of slightly lighter-colored NPGL propagating down the sample as the water was pushed away from the surface.

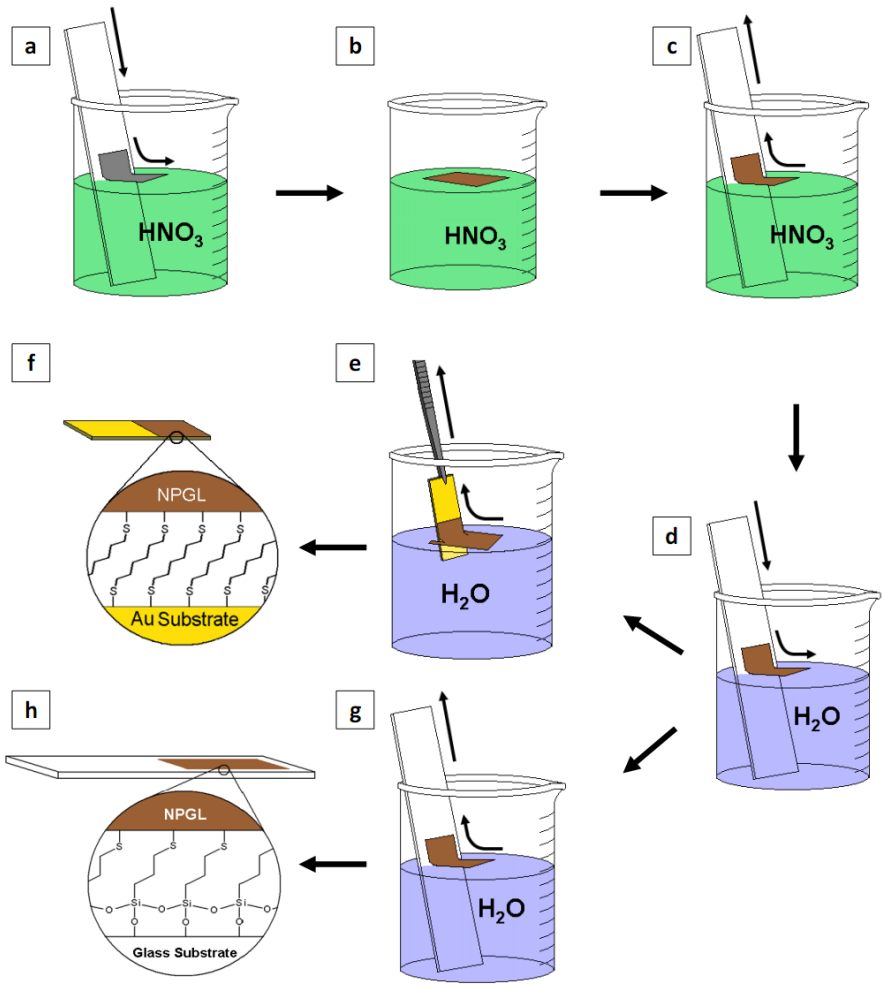

Figure 3.1. NPGL Electrode Fabrication Scheme. **(a)** Gold-silver leaf is transferred from a glass slide to the surface of concentrated nitric acid. **(b)** The leaf is allowed to float on the surface of the nitric acid for a desired time during which the silver is dealloyed. **(c)** The dealloyed leaf is removed from the surface of the nitric acid using a glass slide. **(d)** The leaf is transferred to the surface of deionized water for rinsing. **(e)** The leaf is removed from the air-water interface with a gold substrate (on a silicon support) modified with 1-6 hexanedithiol. **(f)** Free thiol groups secure the NPGL onto the surface of the substrate. **(g)** For attachment to glass substrates, a glass slide modified by mercaptopropyltrimethoxysilane is used to remove the leaf from the water after the rinsing step. **(h)** The free thiols of the silane monolayer bond to the NPGL.

This electrode fabrication scheme extends the innovative work described by Ding and Erlebacher[20] to a scalable, cost-effective means to achieve high-surface-area, gold substrates with nanoscale features using techniques and materials that are easily accessible.

Characterization by Scanning Electron Microscopy

Scanning Electron Microscopy (SEM) images of an electrode surface with a dealloying time of approximately 3 h (**Figure 3.2**) reveal that the mesoporous structure of the NPGL was preserved after the leaf was attached to the flat surface of the gold substrate. The obvious contrast difference between the bright NPGL layer and the darker underlying flat gold layer shown in the cross sectional image (Figure 3.2a) can be credited to the relative ease by which secondary electrons escape the highly porous structure on the surface. The plan view image (Figure 3.2b) reveals that the majority of the pores have diameters between 50 and 100 nm, but some of the smallest pores have diameters of less than 30 nm. Approximating a PSI complex as an oblate spheroid with major and minor axes of 14 nm and 10 nm respectively[22], we postulate that the majority of the pores are of adequate dimensions to allow multiple PSI complexes to attach to the interior surfaces; however, some of the smaller pores could likely be filled or effectively "clogged" by a single PSI rendering the underlying surface area inaccessible. SEM images of NPGL electrodes after dealloying times of 15 min, 1h, and 24 h are presented in **Figure 3.3** which reveal the coarsening effect of prolonged dealloying times that serve to increase the feature size of the NPG and reduce its surface area.

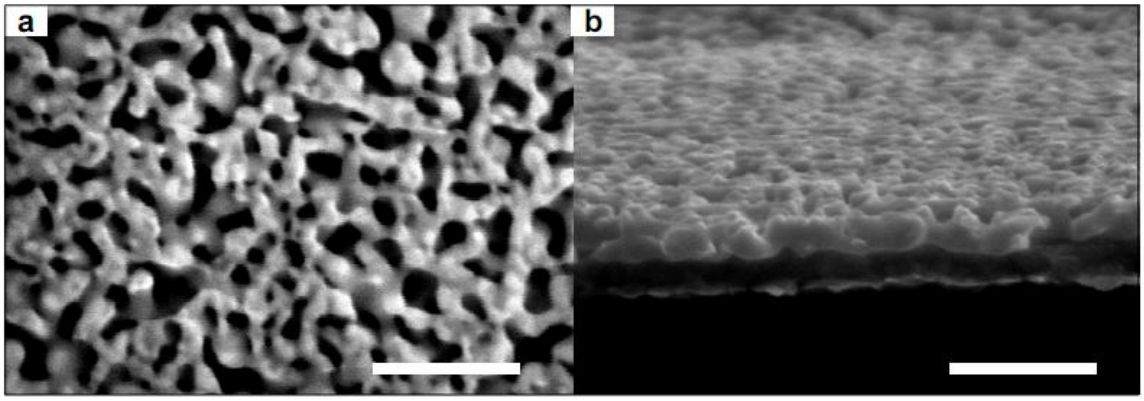

Figure 3.2, Scanning Electron Microscopy Images of an NPGL Electrode Film on a Au Support. (a) Plan view of electrode surface, scale bar 300 nm. **(b)** Cross-section of electrode surface, scale bar 300 nm.

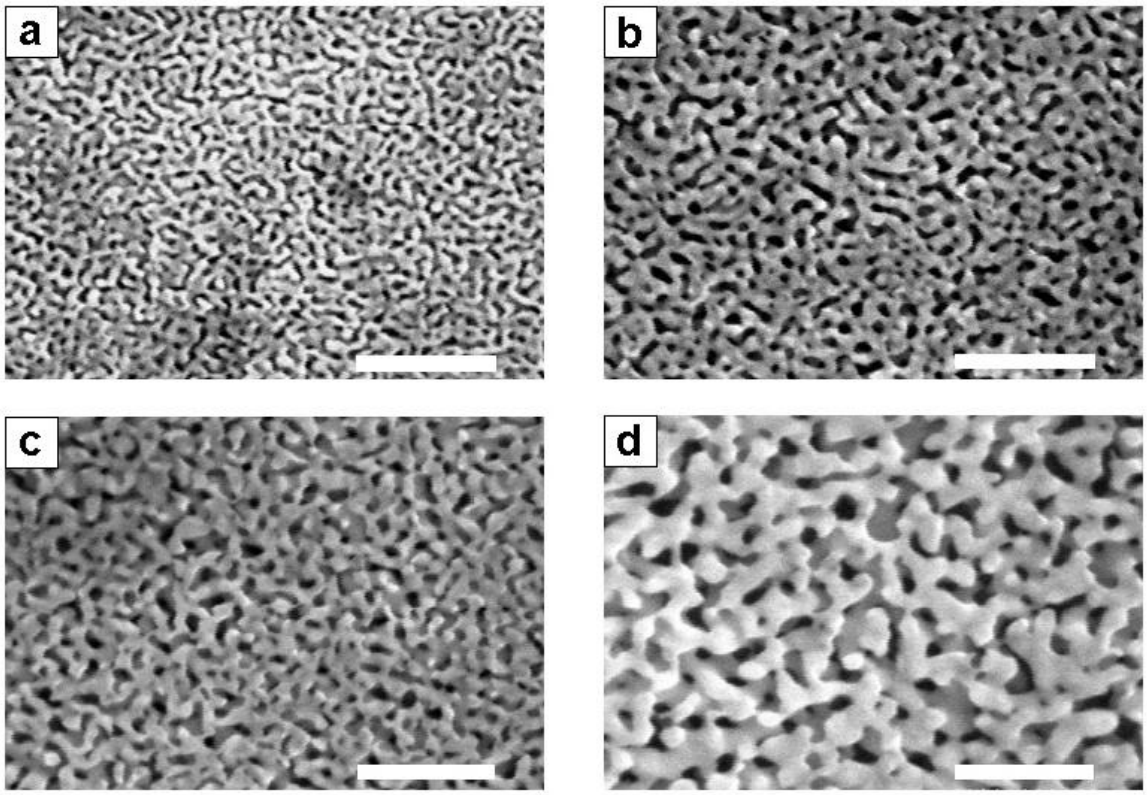

Figure 3.3. SEM images of NPGL at different dealloying times. (a) 15 min dealloying time. **(b)** 1h dealloying time. **(c)** 3h dealloying time. **(d)** 24h dealloying time. All scale bars 500 nm.

Electrode Surface Area Enhancements as Determined by Cyclic Voltammetry

Underpotential deposition (UPD) of silver ions from a sulfuric acid solution was performed to determine the extent to which the enhanced surface area of the newly fabricated electrode was electronically accessible and hence suitable for additional electrochemical applications. **Figure 3.4** shows the cyclic voltammograms (CVs) of NPGL-modified electrodes created by various dealloying times, as well as a planar gold electrode plotted on the same axes for comparison. The cathodic (positive) current peaks are due to the reduction of silver ions from solution resulting in their deposition onto the electrode surface to form a sub-monolayer of silver atoms. Similarly, the anodic (negative) current peak corresponds to the oxidation and removal of the previously deposited silver atoms. An enlarged view of the CV for the planar electrode (Figure 3.4 inset) clearly displays the well defined features expected for Ag UPD on polycrystalline gold,[23] but these features are dwarfed by those of the NPGL electrodes when they are shown together. The integrated charge under these reduction and oxidation peaks varies directly with the available surface area of the electrodes[24]. Comparing the integrated charge for NPGL electrodes with dealloying times of 15 min, 1 h, 3 h, and 24 h to that obtained from a planar electrode revealed that the NPGL electrodes provided surface areas approximately 18.9, 11.6, 9.4, and 4.6 times greater than the flat electrode, respectively. This trend is consistent with the reduction in surface area resulting from the surface-diffusion driven coarsening process that progresses as the leaf is exposed to nitric acid as described previously [25].

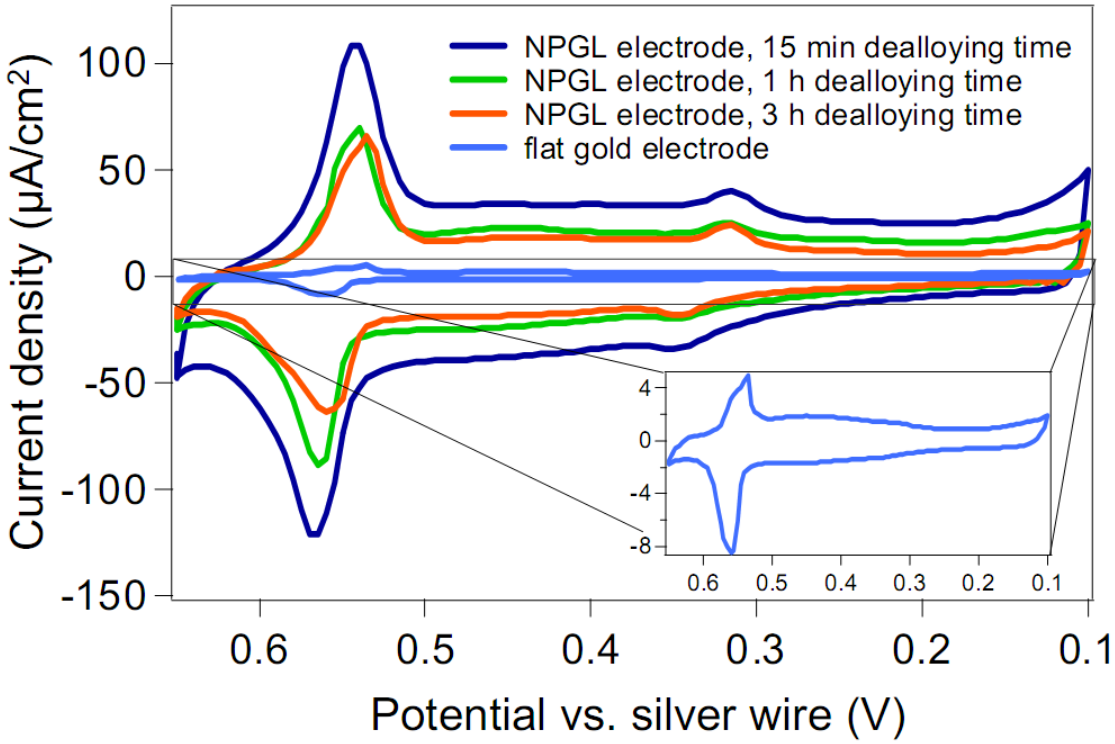

Figure 3.4. Cyclic Voltammograms of NPGL Electrodes After Various Dealloying Times. Current peak areas decrease with longer dealloying times, indicating a reduction in surface area due to pore-widening. **Inset:** Enlarged view of the CV for a planar electrode (control) to display well-defined features.

Electrode Surface Modification and Characterization

To explore the extent to which the versatility of a planar gold electrode was retained by the NPGL electrodes, the surfaces of the latter were exposed to ethanolic solutions containing ω-terminated alkyl thiols of interest to form of a variety of SAMs. Contact angles of water (θ_a) and several parameters obtained via electrochemical impedance spectroscopy (EIS) were measured to confirm the presence of the SAMs at the surface and throughout the mesoporous electrode film, respectively (**Table 3.1**). A series of methyl-terminated SAMs were formed on the NPGL surface and exhibited advancing water contact angles of 119° – 120°. These values are roughly 6-10° higher than those

exhibited by the same SAMs on 2D surfaces, reflecting the effect of the roughness introduced by the mesoporous film on the contact angles as established by Wenzel[26]. Contact angles were generally consistent with the Wenzel equation in that those of hydrophobic and hydrophilic SAMs on NPGL were higher and lower, respectively, than the contact angles measured for the same SAMs on 2-D surfaces. These values are consistent with the presence of the SAMs at the outer facets of the structures but do not necessarily reveal information about the extent of thiol adsorption within the pores.

In order to probe the surface properties throughout the porosity of the NPGL film, we obtained EIS spectra in the presence of $K_3Fe(CN)_6$ and $K_4Fe(CN)_6$ in 0.1 M Na_2SO_4. These data were collected for NPGL attached to glass supports to ensure that the measurements were representative of the NPGL film rather than the underlying gold surface (if an NPGL/Au electrode had been used). The n-alkanethiolate SAMs contributed a significant charge transfer resistance and a greatly reduced film capacitance as determined by fitting the spectra with a Randle's equivalent circuit model (shown schematically in **Figure 3.5a**) to extract these parameters. Film capacitances (C_F) measured for these surfaces displayed a decreasing trend with increasing number of CH_2 units in the adsorbate, affirming an effective increase in film thickness for alkanethiolate SAMs of increasing chain length as previously demonstrated on a 2-D surface.[27] Charge transfer resistance (R_{CT}) measurements displayed a relatively large variance with the -SC_8 and -SC_{10} SAMs exhibiting statistically lower resistances than those obtained for SAMs prepared from longer chain alkanethiols, which has also been reported for n-alkanethiolate SAMs on 2-D surfaces.[27] In contrast to the barrier performance of the n-alkanethiolate films, NPGL surfaces modified with 2-aminoethanethiol, and those

further modified with terephthaldialdahyde (TPDA) (**Figure 3.6a and b**) exhibited impedance similar to a bare NPGL electrode. For these systems, the charge transfer resistance and the film capacitance contributions to impedance were much less significant than those exhibited by the alkanethiolate coatings, which caused the electrochemical impedance in these systems to be dominated by diffusion of the redox probes to the surface. These spectra were fit to a mixed kinetic and charge transfer equivalent circuit model which included a Warburg impedance (*W*) (Figure 3.5b). The observation that that the TPDA-functionalized monolayer introduces little impedance to charge transfer at the electrode surface is a characteristic result of the poorly packed 2-aminoethanethiolate precursor SAM.[28] The relative ease by which charge can transfer through the TPDA-modified SAM, combined with its ability to covalently bind exposed lysine residues of proteins, suggests its utility for applications involving electron transfer to PSI reaction centers.

Table 3.1. Contact Angles and Electrochemical Properties of Modified NPGL Electrode Films.[b]

NPGL Surface Modification	θ_a (°)	C_F (μF)	log R_{CT} (log Ω·cm^{-2})	W (Ω ·s$^{-1/2}$)
Bare NPGL	96 ± 1	—	—	214 ± 39
SC_8 SAM	120 ± 3	2.6 ± 0.3	4.4 ± 0.2	—
SC_{10} SAM	120 ± 3	2.3 ± 0.6	4.3 ± 0.2	—
SC_{12} SAM	119 ± 4	1.5 ± 0.2	5.0 ± 0.5	—
SC_{14} SAM	109 ± 4	1.3 ± 0.3	4.9 ± 0.4	—
SC_{16} SAM	119 ± 6	1.2 ± 0.4	4.9 ± 0.1	—
SC_{18} SAM	123 ± 4	1.1 ± 0.2	5.0 ± 0.4	—
SC_2NH_2 SAM	19 ± 5	—	—	201 ± 66
TPDA Functionalized SAM	35 ± 6	—	—	215 ± 78
PSI Immobilized	90 ± 3	—	0.9 ± 0.2	253 ± 63

[b] Reported values and errors reflect the mean and standard deviations of the measurements, respectively.

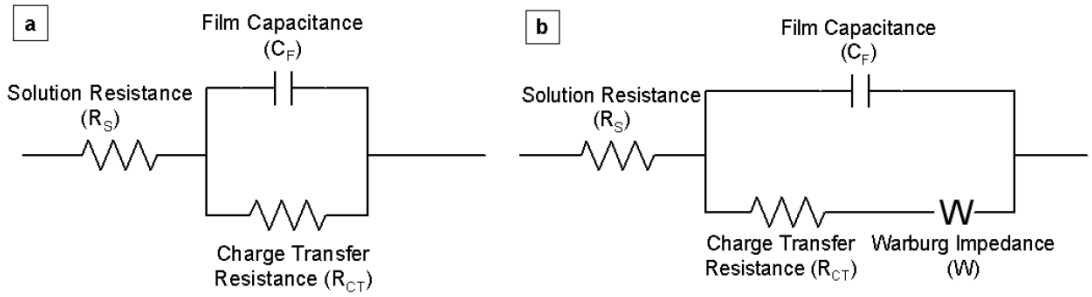

Figure 3.5. Electrochemical Impedance Equivalent Circuit Models. (a) Randle's equivalent circuit model. **(b)** Mixed kinetic and charge transfer equivalent circuit model including a Warburg Impedance**.**

Photosystem I Immobilization and Photocurrent Responses

To anchor PSI directly onto the electrode, the TPDA-functionalized surface was exposed to a phosphate-buffered solution containing PSI suspended in Triton X-100 surfactant. Accessible lysine residues on the outer portions of the protein bind covalently to the terminal aldehydic groups of the SAM,[29] anchoring the protein to the NPGL surface (Figure 3.6c). The presence of PSI on the surface of the NPGL was evident by an increase in the contact angle from ~ 30º on the TPDA modified surface to ~ 90º after the protein complex's immobilization. The reflectance-absorption infrared spectrum (RAIRS) of the PSI modified NPGL (Figure 3.6d) clearly shows the characteristic Amide I and II bands at approximately 1664 and 1546 cm^{-1}, respectively, further confirming the presence of PSI on the electrode surface.[10] Immobilization of PSI also affects the EIS spectrum by introducing a measurable charge transfer resistance while still retaining Warburg impedance behavior of the TPDA-modified SAM precursor at low frequencies.

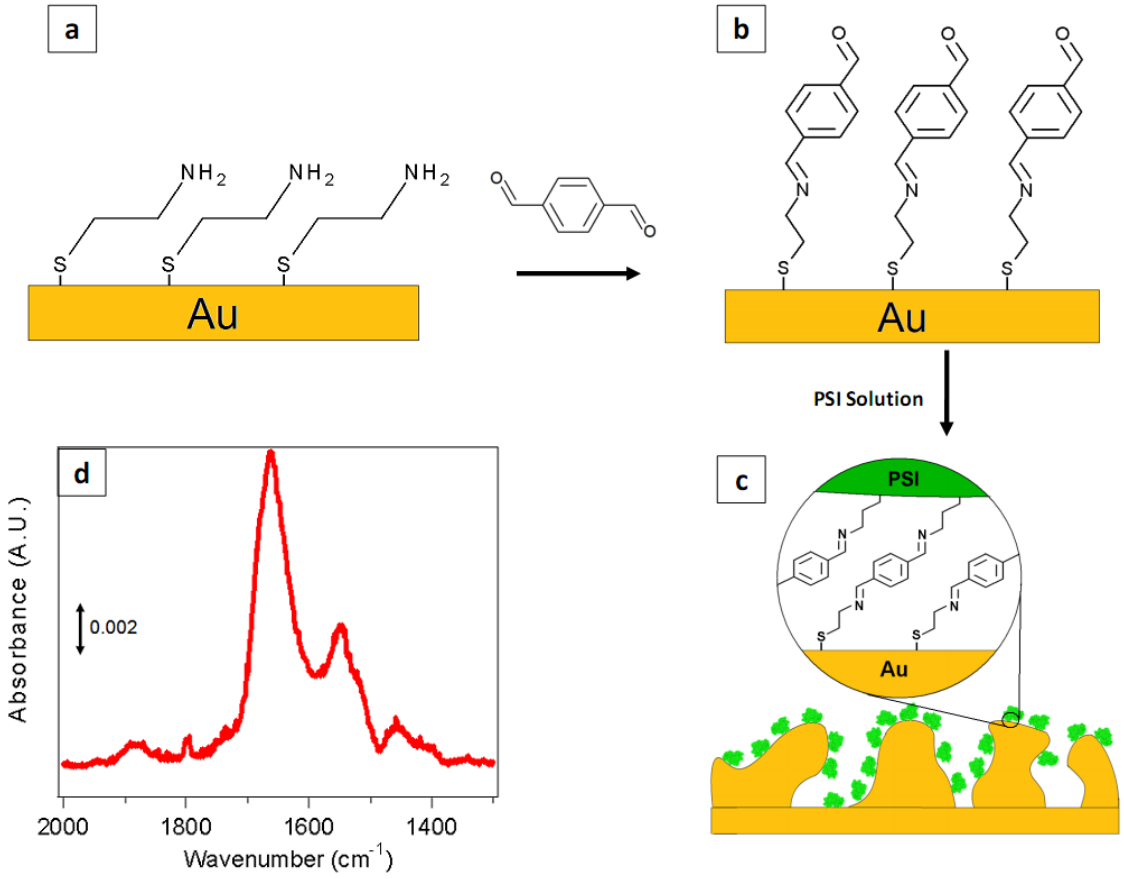

Figure 3.6. Photosystem I attachment Scheme and RAIR Spectrum of PSI-Modified NPGL Surface. (a) The NPGL surface is modified by 2-aminoethanethiol. **(b)** Exposure to TPDA provides the surface with aldehydic terminal groups. **(c)** Exposed lysine residues on PSI covalently bind the protein complex to the electrode surface. **(d)** RAIR spectrum of PSI-modified NPGL surface; characteristic Amide I and II peaks are observed near 1667 and 1546 cm^{-1}, respectively.

Photochronoamperometric measurements were taken for both electrodes in a phosphate buffer solution containing dichloroindophenol (DCIP) as an electrochemical mediator and sodium ascorbate as a sacrificial reagent. Upon irradiation, energy from incident photons is collected by chlorophylls oriented throughout the protein and transferred to the P700 reaction center within PSI. This energy causes the reaction center to achieve an excited state (denoted P700*), after which it initiates charge separation by promoting an electron to an elevated energy level. The excited electron leaves the P700 reaction center in an electron deficient state (denoted $P700^{+}$) as it transfers across the protein complex to reduce the iron-sulfur complex F_B where the electron can be transferred to an electrochemical mediator in solution. In order for the process to begin again, the $P700^{+}$ reaction center must be reduced back to P700. When this reduction is achieved by electrons from the conduction band of the underlying gold substrate, a cathodic current response is measured by the potentiostat. The difference between the current measured when the cell is dark and that measured when the electrode is irradiated is referred to as the photocurrent response of the cell. Typical photocurrent responses for PSI films attached to a 2D electrode and an NPGL electrode (3 h dealloying time) are shown in **Figure 3.7a**. The NPGL electrode displayed ~3 fold enhancement in photocurrent with respect to 2D electrode due to the increased number density of PSI complexes bound to the porous substrate. The magnitude of this photocurrent enhancement for the NPGL electrode is not as great as the surface area enhancement determined by Ag UPD in the cyclic voltammetry experiment; this observation arises because the major axis of a PSI complex is comparable to the diameter of some of the smaller NPGL pores as previously mentioned, and if a PSI were to attach near such a

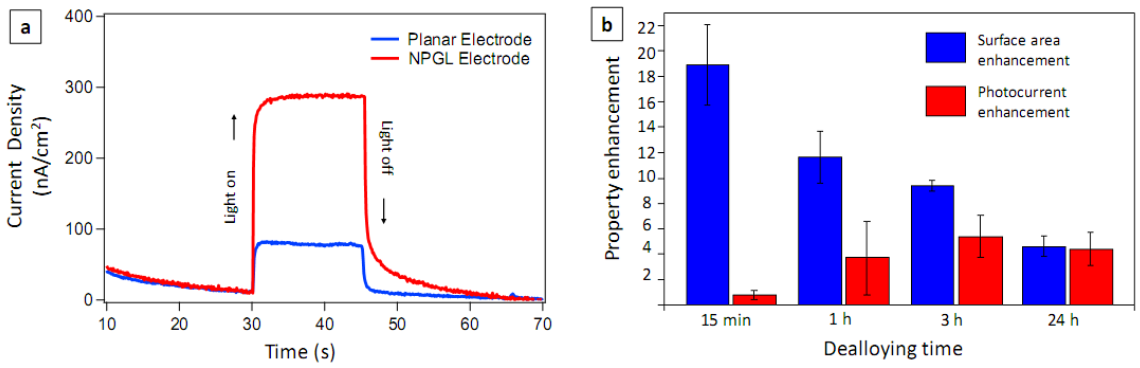

Figure 3.7. Photocurrent Responses of PSI-Modified NPGL Electrodes. (a) Photochrono-amperometric data for a planar gold electrode and an NPGL electrode (3 h dealloying time). **(b)** Photocurrent and surface area enhancements provided by NPGL films of various dealloying times with respect to planar gold electrodes. Mean values are reported and the standard deviations are shown as error bars. Although large surface area enhancements are achieved at short dealloying times, the pore sizes are too small to allow multiple PSI complexes to attach inside the pores. Dealloying times of 3 h and longer yield electrodes whose surface area and photocurrent enhancements are similar in magnitude, suggesting that the majority of the surface area is accessible to PSI.

pore, it could block potential binding sites deeper inside the pore. Figure 3.7b shows photocurrent enhancements provided by PSI-modified NPGL electrodes of varying dealloying times, presented alongside the surface area enhancements determined by the UPD of silver. Although the greatest surface area enhancements are achieved at short dealloying times because of the relatively small pore sizes, these pores are too small to offer interior binding sites to the larger PSI complexes. At dealloying times of 1 h and longer, many of the pores are of adequate dimensions to accommodate multiple PSI complexes, resulting in an increase in the number of PSI complexes bound per unit of geometric area, thus producing photocurrent enhancements of roughly 3-7 fold with respect to the planar electrodes. Dealloying times of 24 h consistently produced

electrodes with similar surface area and photocurrent enhancements, suggesting nearly all of the surface area introduced to the electrode by the NPGL film is accessible to PSI.

Photocurrent Responses at Varying Light Intensities.

The response of these electrodes to varying intensities of polychromatic visible light must be assessed should they be used in photocatalytic applications that utilize solar energy. As preliminary investigation of this behavior, PSI-modified planar and NGPL electrodes (1 h dealloying time) were irradiated with several different intensities of white light. The intensity at the surface of the electrode was measured with a light meter and the corresponding photocurrent response was recorded. This experiment was repeated for three identically prepared NPGL samples and four identically prepared planar samples and the results are presented in **Figure 3.8**. These photocurrent responses display an increasing trend with light intensity, indicating that the photocurrents observed over this range of intensities are influenced not only by the kinetics governing the interaction of PSI's electron donating and accepting reaction centers with the electrochemical mediators and the underlying electrode, but are also largely dependent upon the rate of photoexcitation of P700 reaction centers. As stated by the Beer-Lambert Law, absorbance varies directly with the concentration of the absorbing species, thus the relatively sharp response to increasing light intensities by PSI adsorbed onto the NPGL films is consistent with the larger PSI/electrode interfacial areas, which effectively raises the proteins concentration per geometric area allowing for increased light absorption and photocurrent production. These results also demonstrate that the photocurrent

enhancements provided by the NPGL electrode films are preserved over the range of intensities employed in this study.

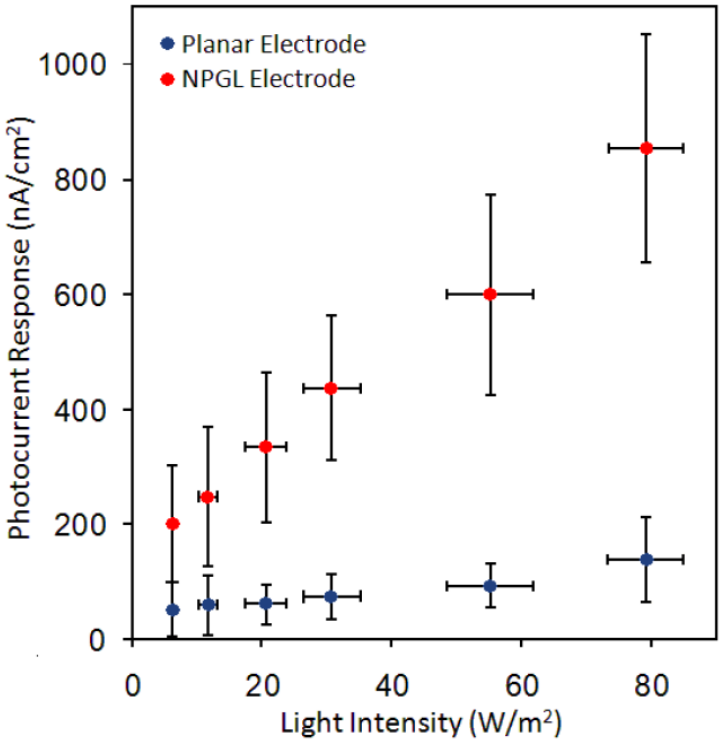

Figure 3.8. Photocurrent Responses at Various Intensities of White Light. Points represent mean values with vertical and horizontal error bars showing the standard deviations of the photocurrent responses and light intensities, respectively, measured at six different lamp intensity settings (n = 3 for NPGL electrodes, n = 4 for planar electrodes).

Conclusions

In summary, we have presented a method to fabricate nanoporous gold leaf electrode films, attach them to gold and glass supports, and impart photonic energy conversion capabilities to them by modification with Photosystem I. We have demonstrated that the average feature size and hence surface area of these NPGL electrodes can be adjusted, and that they can be modified by various SAMs to exhibit different electrochemical

behaviors and surface properties. The immobilization of PSI on the surface of NPGL electrodes as opposed to planar electrodes provided an increase in PSI-catalyzed photocurrent in the presence of electrochemical mediators. This photocurrent enhancement was dependent upon the dealloying time used in the electrode fabrication process, with dealloying times of 3 h and longer producing feature sizes that render the majority of the surface area accessible to PSI. The robust electrode fabrication method presented herein can easily be extended to a myriad of applications beyond those described in this work, making 3-D mesoporous surfaces readily available through straightforward, bench-top laboratory techniques.

Methods

Gold Leaf Dealloying.

100 nm thick Monarch 12 Karat White Gold (fineartstore.com) was cut to ~1.5 x 1.5 cm and floated on approximately 40 ml of concentrated nitric acid (Fisher) in a 50 ml glass beaker for various dealloying times to yield NPGL. Au/Si supports were prepared by thermally evaporating 125 nm of Au (J&J Materials) onto silicon wafers (Montico Silicon, <100> orientation, 100 mm diameter, 500-550 mm thick) with a 10 nm adhesion layer of Cr (R.D. Mathis). Samples were cut to approximately 1.3 cm x 2 cm. The gold surface was then exposed to a 20 mM solution of hexanedithiol (Aldrich) in ethanol (Pharmco – AAPER) for 24 h. Glass supports were prepared by exposing glass microscope slides (Fisher) to a 5 mM solution of mercaptopropyltrimethoxysilane (Acros) in hexane (Fisher) at 60° C for 1 h. NPGL was then collected on the surface of the

substrates as shown in Figure 3.1 and described in the discussion of the fabrication process in this chapter.

Scanning Electron Microscopy.

SEM images were taken with a Hitachi S-4200 Scanning Electron Microscope using an accelerating voltage of 15 kV.

Cyclic Voltammetry.

Cyclic voltammetry was performed with a Gamry Instruments CMS300 electrochemical system using an aqueous solution of 0.1 M sulfuric acid (EMD) and 0.6 mM silver sulfate (Aldrich) with an Ag/AgCl reference and a gold counter electrode. Voltage was cycled from 0.65 to 0.05 V with a scan rate of 20 mV/s . The fourth cycle is presented in this work.

SAM Formation, TPDA Modification, and PSI Immobilization.

SAMs on gold surfaces were formed by exposing the electrode surface to 1 mM ethanolic solutions of the thiol adsorbate for 12 h; samples used in the EIS analysis were exposed at least 50 h to allow ample time to reduce the density of defect sites within the monolayer. Octanethiol, decanethiol, dodecanethiol, hexadecanethiol, and octadecanethiol were purchased from Aldrich; tetradecanethiol was purchased from Fluka; aminoethanethiol was purchased from Acros. Amine-terminated SAMs on NPGL were modified with TPDA by exposing the surface to 1 mM solutions of terephthaldialdehyde (Aldrich) for 1 h. PSI attachment was accomplished by exposing

the TPDA-modified surface to a solution of approximately $1.5x10^{-7}$ mol L^{-1} of PSI, as measured by P700 content, in elution buffer (0.2 M Na phosphate, 0.05 wt/vol% Triton X-100) for 48-72 h at 4º C, after which, the samples were rinsed with deionized water and dried with nitrogen.

Contact Angle Measurements.

Advancing contact angles of deionized water were measured using a Rame-Hart goniometer. Three measurements were taken on different locations for at least 2 independently prepared samples. Reported values and errors reflect the mean and standard deviations of the measurements, respectively.

Electrochemical Impedance Spectroscopy.

EIS was performed with a Gamry Instruments CMS300 impedance system using electrochemical cell consisting of 1 mM $K_3Fe(CN)_6$ and 1 mM $K_4Fe(CN)_6$ in 0.1 M Na_2SO_4(aq) as an electrolyte, an Ag/AgCl reference electrode, a gold counter electrode, and the sample of interest as the working electrode. The frequency of a 10 mV rms AC voltage was varied from 10^{-1} to 10^5 Hz , with 10 points per decade recorded. Data were fit to equivalent circuit models using the Gamry E-chem Analyst software package. Reported values and errors reflect the mean and standard deviations, respectively, of at least three independently prepared samples.

PSI Extraction.

Commercial baby spinach leaves were used for the isolation of thylakoid membranes by the method of Reeves and Hall[30] with modifications as described recently.[31] A hydroxylapatite column was used for additional separation and isolation of native PSI involved as described by Shiozawa *et al.*[32] and Lee *et al.*[33] The effluent PSI suspension was stored at -80 °C. The P700 reaction center concentration of the elution buffer used in this study was determined to be approximately 9 μM by monitoring the changes in UV-vis absorbance as described by Baba *et al.*[34]

Reflectance-Absorption Infrared Spectroscopy.

RAIRS was performed with a Bio-Rad Excalibur FTS-3000 infrared spectrometer, using p-polarized light at an incident angle approximately 80° from the surface normal. The instrument was operated in single reflection mode. 1000 scans were accumulated for each sample, using a sample of bare NPGL attached to a gold substrate as a background. A water spectrum was subtracted from that spectrum obtained from the PSI-modified NPGL, and the difference is presented in this work.

Photochronoamperometry.

Photochronoamperometric data were collected using a CH Instruments CHI660a electrochemical workstation with a Faraday cage. A three electrode cell was used with the PSI-modified NPGL as the working electrode, platinum mesh as the counter electrode, and Ag/AgCl as the reference electrode. Planar PSI-modified Au electrodes were prepared identically and served as working electrodes in order to calculate photocurrent

enhancements contributed by the NPGL. All photochronoamperometric data were taken at a bias of -0.1 V vs. Ag/AgCl, in a mediator solution consisting of 250 µM dichloroindophenol (Acros), 5 mM sodium ascorbate (Aldrich), 100 mM NaCl (Fisher) in a pH 7 phosphate buffer (Fisher). The electrodes were illuminated with a Gebrauch KL 2500 LCD. Light intensity was measured using a SPER Scientific 840022 Advanced Light Meter.

Works Cited

1. Das, R., et al., *Integration of photosynthetic protein molecular complexes in solid-state electronic devices.* Nano Letters, 2004. **4**(6): p. 1079-1083.

2. Frolov, L., et al., *Fabrication of a photoelectronic device by direct chemical binding of the photosynthetic reaction center protein to metal surfaces.* Advanced Materials, 2005. **17**(20): p. 2434-+.

3. Frolov, L., et al., *Fabrication of oriented multilayers of photosystem I proteins on solid surfaces by auto-metallization.* Advanced Materials, 2008. **20**(2): p. 263-+.

4. Carmeli, I., et al., *Photovoltaic activity of photosystem I-based self-assembled monolayer.* Journal of the American Chemical Society, 2007. **129**(41): p. 12352-+.

5. Carmeli, I., et al., *A photosynthetic reaction center covalently bound to carbon nanotubes.* Advanced Materials, 2007. **19**(22): p. 3901-+.

6. Terasaki, N., et al., *Fabrication of novel photosystem I-gold nanoparticle hybrids and their photocurrent enhancement.* Thin Solid Films, 2006. **499**(1-2): p. 153-156.

7. Terasaki, N., et al., *Bio-photo sensor: Cyanobacterial photosystem I coupled with transistor via molecular wire.* Biochimica Et Biophysica Acta-Bioenergetics, 2007. **1767**(6): p. 653-659.

8. Laibinis, P.E., et al., *Thin Films*, ed. A. Ulman. Vol. 24. 1998, Boston: Academic Press.

9. Lee, I., J.W. Lee, and E. Greenbaum, *Biomolecular electronics: Vectorial arrays of photosynthetic reaction centers.* Physical Review Letters, 1997. **79**(17): p. 3294-3297.

10. Kincaid, H.A., et al., *Entrapment of photosystem I within self-assembled films.* Langmuir, 2006. **22**(19): p. 8114-8120.

11. Huang, W.X., et al., *Functionalization of surfaces by water-accelerated atom-transfer radical polymerization of hydroxyethyl methacrylate and subsequent derivatization.* Macromolecules, 2002. **35**(4): p. 1175-1179.

12. Jennings, G.K. and E.L. Brantley, *Physicochemical properties of surface-initiated polymer films in the modification and processing of materials.* Advanced Materials, 2004. **16**(22): p. 1983-1994.

13. Berron, B.J., E.P. Greaybill, and G.K. Jennings, *Growth and Structure of Surface-Intitated Poly(n-alkylnorbornene) Films.* Langmuir, 2007. **23**(23): p. 11651-11655.

14. Sun, T.L., et al., *Reversible switching between superhydrophilicity and superhydrophobicity.* Angewandte Chemie-International Edition, 2004. **43**(3): p. 357-360.

15. Martin, C.R., *Nanomaterials - a Membrane-Based Synthetic Approach.* Science, 1994. **266**(5193): p. 1961-1966.

16. Sander, M.S. and L.S. Tan, *Template-assisted assembly of arrays of nanoscale particles and molecular islands on surfaces.* Abstracts of Papers of the American Chemical Society, 2003. **226**: p. U761-U761.

17. Wirtz, M. and C.R. Martin, *Template-fabricated gold nanowires and nanotubes.* Advanced Materials, 2003. **15**(5): p. 455-458.

18. Prikulis, J., et al., *Optical spectroscopy of nanometric holes in thin gold films.* Nano Letters, 2004. **4**(6): p. 1003-1007.

19. Turkevich, J., P.C. Stevenson, and J. Hillier, *A study of the nucleation and growth processes in the synthesis of colloidal gold.* Discussions of the Faraday Society, 1951. **11**: p. 55 - 75.

20. Ding, Y., Y.J. Kim, and J. Erlebacher, *Nanoporous gold leaf: "Ancient technology"/advanced material.* Advanced Materials, 2004. **16**(21): p. 1897-+.

21. Erlebacher, J., et al., *Evolution of nanoporosity in dealloying.* Nature, 2001. **410**(6827): p. 450-453.

22. Amunts, A., O. Drory, and N. Nelson, *The structure of a plant photosystem I supercomplex at 3.4 Å resolution.* Nature, 2007. **447**(7140): p. 58-63.

23. Chen, C.H., S.M. Vesecky, and A.A. Gewirth, *In situ atomic force microscopy of underpotential deposition of silver on gold(111).* J. Am. Chem. Soc., 1992. **114**(2): p. 451-458.

24. Myland, J.C. and K.B. Oldham, *Quasireversible cyclic voltammetry of a surface confined redox system: a mathematical treatment.* Electrochemistry Communications, 2005. **7**(3): p. 282-287.

25. Erlebacher, J., *An Atomistic Description of Dealloying* Journal of the Electrochemical Society, 2004. **151**(10): p. C614-C626.

26. Wenzel, R.N., *Resistance of Solid Surfaces to Wetting by Water.* Industrial and Engineering Chemistry, 1936. **28**(8): p. 988-994.

27. Jennings, G.K., et al., *Effect of chain length on the protection of copper by n-alkanethiols.* Langmuir, 1998. **14**(21): p. 6130-6139.

28. Wallwork, M.L., et al., *Complex chemical force titration behavior of amine-terminated self-assembled monolayers.* Langmuir, 2001. **17**(4): p. 1126-1131.

29. Rozkiewicz, D.I., B.J. Ravoo, and D.N. Reinhoudt, *Reversible covalent patterning of self-assembled monolayers on gold and silicon oxide surfaces.* Langmuir, 2005. **21**(14): p. 6337-6343.

30. Reeves, S.G. and D.O. Hall, *Higher Plant Chloroplasts and Grana: General Preparative Procedures (Excluding High Carbon Dioxide Fixation Ability Chloroplasts).* Methods in Enzymology, 1980. **69**: p. 85-94.

31. Ciobanu, M., et al., *Photosystem I Patterning Imaged by Scanning Electrochemical Microscopy.* Langmuir, 2005. **21**: p. 692-698.

32. Shiozawa, J.A., R.S. Alberte, and J.P. Thornber, *P700-Chlorophyll a-Protein - Isolation and Some Characteristics of Complex in Higher Plants.* Archives of Biochemistry and Biophysics, 1974. **165**(1): p. 388-397.

33. Lee, J.W., W. Zipfel, and T.G. Owens, *Quenching of Chlorophyll Excited-States in Photosystem-I by Quinones - Stern-Volmer Analysis of Fluorescence and Photochemical Yield.* Journal of Luminescence, 1992. **51**(1-3): p. 79-89.

34. Baba, K., et al., *Photoinhibition of photosystem I electron transfer activity in isolated photosystem I preparations with different chlorophyll contents.* Photosynthesis Research, 1996. **47**(2): p. 121-130.

CHAPTER IV

A KINETIC MODEL OF THE PHOTOCATALYTIC EFFECT OF A PHOTOSYSTEM I MONOLAYER ON A PLANAR ELECTRODE SURFACE

Introduction

In this chapter, I develop a mechanistic model for the photocatalytic effect produced by a monolayer of PSI complexes adsorbed onto a planar electrode surface and compare the simulated current density produced by the model to experimental chronoamperometric data. Previous studies have shown that PSI complexes assembled at electrode interfaces may interact electrochemically directly with the electrode surface as well as with electrochemical mediators in the electrolyte.[1-4] The heterogeneous electron transfer events that occur in these systems may be precisely monitored by analytical electrochemical methods, which makes the PSI-modified electrode system an ideal platform for analysis of the protein's photocatalytic behavior by the application of a mechanistic model. A model for the steady state electron transfer between PSI complexes suspended in solution and cytochrome c(6) assembled at the electron surface was previously developed by Proux-Delrouyre and colleagues[5]. While the study demonstrated an insightful method by which electrochemical measurements, mainly cyclic voltammograms, may be used to extract information about the steady-state kinetics and bioenergetics of biological redox couples, it did not describe direct electrochemical interactions between PSI and the electrode surface, nor did it investigate the transient behavior of the system displayed when the irradiation conditions change abruptly. Much of the attraction of PSI is that its rapid, photoinduced electron transfer capabilities may be interfaced with non-biological materials. Thus, additional quantitative characterization of

the photoelectrochemical behavior of systems that make use of PSI complexes adsorbed at an electrode/electrolyte interface is pertinent to the design of future biohybrid technologies and devices that utilize PSI, and such is the focus of the present chapter.

Model Description

A schematic of a PSI monolayer on an electrode surface is shown in **Figure 4.1**. Chlorophylls oriented within PSI absorb energy from photons and transfer it to a special pair of chlorophylls that make up the P_{700} reaction center. Receipt of this energy causes the reaction center to achieve an excited state denoted P_{700}^{*}, which is quickly oxidized to P_{700}^{+} as it releases an electron into an energy cascade of intra-protein cofactors made up of chlorophylls and phylloquinones that transfer the electron to iron sulfur complexes located on the stromal side of the protein. The terminal electron acceptor of the electron transfer chain of PSI is an iron sulfur complex denoted F_B, which is reduced to F_B^- when the electron arrives. In natural photosynthesis, F_B^- is oxidized by chloroplast ferredoxin, and electrons are resupplied to P_{700}^{+} by plastocyanin. However, in the absence of PSI's naturally occurring redox partners, the reduction potentials of F_B^- and P_{700}^{+} (-0.58 and +0.49 V vs NHE, respectively) allow them to react with many xenobiotic compounds including viologens,[6] metal salts, and coordination compounds.[7, 8] The $K_3Fe(CN)_6/K_4Fe(CN)_6$ redox couple was chosen for this study because its redox potential (~ 0.36 - 0.45 V vs NHE)[9] allows its oxidized and reduced forms to react with F_B^-

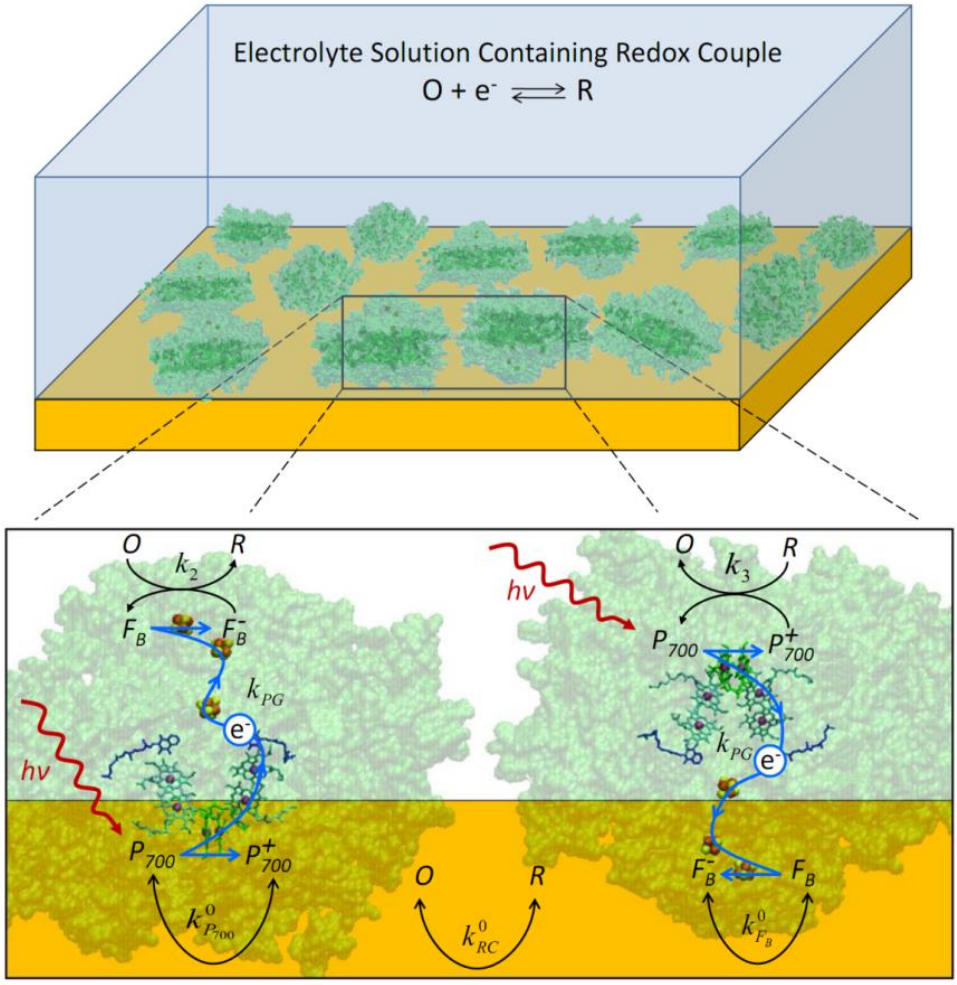

Figure 4.1. Schematic of a PSI-Modified Electrode. A monolayer of PSI complexes on an electrode surface will photocatalyze redox reactions in the presence of an electrolyte that contains a redox couple that is suitable to act as an electrochemical mediator. **Zoom Window: Redox Reactions and Electron Transfer Pathways at the Surface of a PSI-Modified Electrode.** In dark conditions, current flows due to heterogeneous reactions of the redox couple. When the electrode is irradiated, energy from photons is collected by chlorophylls coordinated within PSI and transferred to the special pair of chlorophylls that compose the P_{700} reaction center. The reaction center is quickly oxidized to P_{700}^+ as it releases an electron into an energy cascade of intra-protein cofactors that transfer the electron to PSI's terminal electron acceptor, an iron-sulfur complex denoted F_B, which is reduced to F_B^-. An oxidized P_{700}^+ may be reduced back to P_{700} by a reduced mediator; similarly, a reduced F_B^- may be oxidized back to F_B by an oxidized mediator. The PSI complex on the left is oriented such that its P_{700} reaction center is electronically accessible to the underlying electrode, while that on the right is oriented such its F_B iron sulfur complex is electronically accessible to the electrode. Atomic coordinates for the representations of PSI complexes used in this figure were contributed by Amunts *et al.*,[10] PDB entry 2O01.

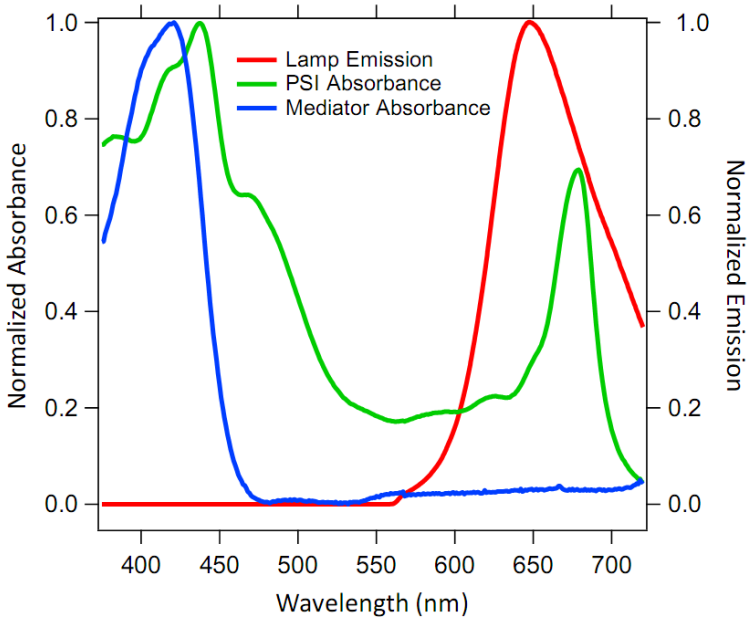

Figure 4.2. Emission Spectrum of Light Source and Absorption Spectra of PSI and Redox Couple. Although both PSI and the redox couple absorb strongly in the blue region of the visible spectrum, irradiation of the electrode using a lamp equipped with a red filter excites only chlorophyll pigments bound in the antenna complexes of PSI. This eliminates contributions to photocurrent produced by photoexcitation of the redox couple.

and P_{700}^{+}, respectively. In addition, this electrochemical mediator does not undergo photoinduced electronic transitions at energies that correspond to photons of wavelength greater than ~ 470 nm (see **Figure 4.2**); thus, irradiating the system with a light source equipped with a red filter will minimize photocurrent contributions from photo excitation of the redox couple. For simplicity during the discussion of the remainder of this chapter, the oxidized form of this redox couple, $K_3Fe(CN)_6$, will be referred to as *O*, and the reduced form, $K_4Fe(CN)_6$, will be referred to as *R*.

The net current density measured from a PSI-modified electrode during a chronoamperometric experiment is determined by the rates of the heterogeneous redox

reactions occurring at the electrode and thus, contains contributions from electron transfer between the electrode and the redox couple in the electrolyte as well as electron transfer between the electrode and the adsorbed PSI complexes. These reactions were modeled using an interface balance similar to the method described by Deen,[11] wherein conservation statements for the heterogeneous reactants are evaluated at the electrode/electrolyte interface. This approach was extended to an electrode modified by a PSI monolayer by considering the system to contain three redox couples: the mobile electrochemical mediator consisting of the *O*/*R* redox couple, and two adsorbed redox couples, P_{700}^{+} / P_{700} and F_B / F_B^{-}, that correspond to the reaction centers of PSI complexes. These redox couples were assumed to participate in heterogeneous electron transfer reactions with the electrode and with each other as shown schematically in Figure 4.1, and kinetic descriptions of these interactions are developed in the remainder of this section. The electrode was considered an infinite planar surface, and *x* was designated as the direction parallel to the surface normal, with $x = 0$ at the electrode/electrolyte interface.

Some discrepancy exists between the dimensions of PSI as measured by TEM,[12] AFM,[13] and STM,[14] yet all of these studies place the major axis of the protein between 6 and 14 nm, and the minor axis between 5 and 12 nm. For this model, we assumed the footprint of a single PSI complex in a dense monolayer to be ~80 nm^2, which corresponds to an ellipse of major and minor axes 12 and 8.5 nm respectively, and an approximate surface concentration, denoted Γ_{PSI}, of 2 x 10^{-12} mol/cm^2. Dense monolayers of PSI were prepared in this study by exposing a suspension of the protein to gold surfaces that were modified by a SAM of aminoethanethiol that was

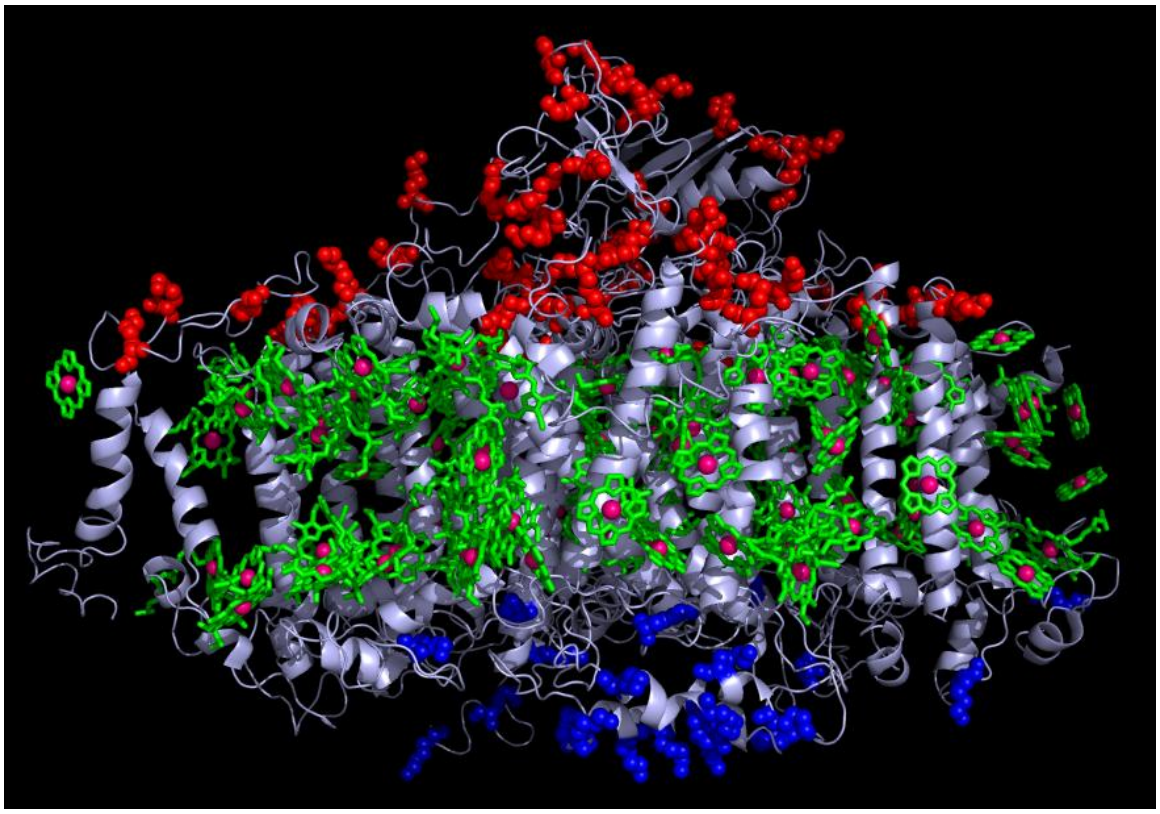

Figure 4.3. Structural Model of PSI Highlighting Location of Lysine Residues. The attachment scheme employed to immobilize PSI on the electrode surface covalently binds lysine residues on the protein to functional groups of the SAM. Lysine residues located on the stromal side of PSI are highlighted in red, while those on the lumenal side are shown in blue. The orientation of PSI complexes on the electrode surface was assumed to be proportional to the distribution of these residues on the protein. Atomic coordinates for the representations of PSI complexes used in this figure were contributed by Amunts *et al.*,[10] PDB entry 2O01.

functionalized with terephthaldialdehyde. The aldehyde terminal groups of this SAM form covalent bonds with the lysine residues on the exterior of PSI, which anchors the protein to the electrode surface.[2, 3] Lysine residues are found on the hydrophilic regions of PSI, on both the stromal and lumenal regions as shown in **Figure 4.3**. Excluding the light-harvesting subunits, plant PSI has ~ 88 lysine residues, 24 of which are located on the lumenal side, and the remaining 64 are found on the stromal side. Based on this attachment scheme, we assumed that the P_{700} site of PSI complexes bound

to the surface via a lysine residue on the lumenal side (highlighted in blue in Figure 4.3) was electronically accessible to the electrode (see PSI complex on left of Figure 4.1 zoom window), and that the F_B site of PSI complexes bound to the surface via lysine residues on the stromal side (highlighted in red in Figure 4.3) was electronically accessible to the electrode (see PSI complex on right of Figure 4.1 zoom window). In addition, the orientation of PSI complexes in the monolayer was assumed to be proportional to the number of lysine residues on each side, thus 27% were assumed oriented with their P_{700} sites accessible to the electrode, and 73% were oriented with their F_B sites accessible. We further assumed that each PSI complex contained one P_{700} reaction center that could exist in either the ground (or reduced) state simply denoted P_{700}, or the oxidized state denoted P_{700}^{+}. Similarly, each PSI was assumed to contain one F_B FeS complex that could exist in the reduced F_B^{-} state, or the oxidized F_B ground state. These assumptions yield the following relationship between the surface concentrations of the different states of PSI's reaction centers (in units of mols·cm^{-2}) and the surface concentration of PSI complexes:

$$\Gamma_{P_{700}^{+}} + \Gamma_{P_{700}} = \Gamma_{PSI} \tag{9}$$

$$\Gamma_{F_B^{-}} + \Gamma_{F_B} = \Gamma_{PSI} \tag{10}$$

While there has been controversy concerning whether the F_A FeS complex can act as the terminal electron acceptor in PSI in addition to, or instead of, F_B (see reference [15] for a review of the electron transfer between the FeS complexes of PSI), electron transfer

within PSI is generally accepted to proceed as $F_X \rightarrow F_A \rightarrow F_B$,[16] and was thusly assumed in this model.

Photogeneration of the F_B^- and P_{700}^+ sites requires the absorption of photons by chlorophylls within PSI, as well as P_{700} reaction centers in the reduced state to donate electrons into their corresponding electron transfer chains, and F_B sites in the oxidized state to receive these electrons. While, in reality, this event is not an elementary step and proceeds via an electron transfer chain made up of several co-factors and FeS intermediates, for the purpose of this analysis, the overall reaction was simplified to

$$P_{700} + F_B + h\nu \longrightarrow P_{700}^+ + F_B^- \tag{11}$$

We[3] and others[4] have observed the photocurrent responses of PSI modified electrodes to be proportional to the intensity of the irradiation incident at the electrode surface. Thus, considering the photogeneration reaction as described by equation (11) is advantageous because it allows photons in this system to be treated as reactants on a molar basis. For irradiation by light of a single wavelength λ, we propose a general rate expression to describe the photogeneration of F_B^- and P_{700}^+ sites in units of [mols·cm^{-2}·s^{-1}] given by:

$$r_1(\lambda) = N_\lambda \theta_\lambda \eta_{IQ} k_{PG} \Gamma_{P_{700}} \Gamma_{F_B} \tag{12}$$

where N_λ is the flux of photons of wavelength λ at the electrode surface in units of [mols·cm^{-2}·s^{-1}], θ_λ is the fraction of those incident photons that are absorbed by the PSI complexes on the electrode surface, and η_{IQ} is the internal quantum efficiency of PSI (i.e. the probability that the absorbed photon will initiate charge separation, which is conservatively estimated as 95% [17, 18]), and k_{PG} is a proportionality constant with

units of [$cm^4 \cdot mol^{-2}$] that relates the photonic flux to the photogeneration of F_B^- and P_{700}^+ sites. The photoresponses presented in this study were generated with a polychromatic light source equipped with a red filter, and the intensity of light at the electrode surface was measured to be 27.5 mW/cm^2. The emission spectrum of the filtered light exhibited a maximum at 648 nm; thus, the photonic flux N_λ incident the electrode was calculated from the intensity at the electrode surface by the expression

$$N_\lambda = \frac{P\lambda}{hcN_A} \tag{13}$$

where P is the intensity of the light reaching the electrode in units of $W \cdot cm^{-2}$, h is Plank's constant, c is the velocity of light, N_A is Avogadro's constant, and λ was assumed to be 648 nm for all photons to yield a photonic flux of 1.5×10^{-7} $mol \cdot cm^{-2} \cdot s^{-1}$. The fraction of photons of wavelength λ absorbed by the PSI monolayer, θ_λ is related to the absorbance of the film at λ by the expression

$$\theta_\lambda = 1 - \frac{I(\lambda)}{I_0(\lambda)} = 1 - 10^{-A(\lambda)} \tag{14}$$

where $I_0(\lambda)$ is the intensity of light of wavelength λ before passing through the PSI film, $I(\lambda)$ is the intensity after passing through the film, and $A(\lambda)$ is the absorbance of the PSI film at wavelength λ which is defined as

$$A(\lambda) = -\log_{10}\left(\frac{I(\lambda)}{I_0(\lambda)}\right) \tag{15}$$

The absorbance of a PSI monolayer in the visible region was below the detection limit of the spectrometer and thus, could not be measured; however, the absorbance in the region of the lamp emission spectrum was estimated to an order of magnitude using the Beer-

Lambert law, $A = b\varepsilon c$, with the previously published extinction coefficient of 57,000 $M^{-1} \cdot cm^{-1}$ for the red peak of chlorophyll *a* bound within PSI complexes[19], using a corresponding volumetric concentration estimated by assuming a film thickness of 7 nm[2]. These assumptions correspond to a volumetric concentration of 3 mM for the PSI film, which yields an absorbance of ~10^{-4}, and leads to an approximate absorbance fraction, θ, of 2 x 10^{-4} in the red region from equation (14). Substituting equations (9) and (10) into (12) to ensure the number of photogenerated F_B^- and P_{700}^+ sites does not exceed the number of reaction centers provided by PSI complexes present in the system, one obtains the following expression for the rate of photogeneration of F_B^- and P_{700}^+ sites:

$$r_1(\lambda) = N_\lambda \theta_\lambda \eta_{IQ} k_{PG} \left(\Gamma_{PSI} - \Gamma_{P_{700}^+}\right)\left(\Gamma_{PSI} - \Gamma_{F_B^-}\right) \tag{16}$$

Consumption of F_B^- and P_{700}^+ sites may occur by their oxidation and reduction, respectively, by the redox couple and by the electrode directly. In addition, charge recombination between F_B^- and P_{700}^+ may consume these photogenerated states; however, this process is orders of magnitude slower than photoinduced charge separation[20] and was thus considered to be negligible in the present model. The reduction of a mediator in the oxidized state by F_B^- is described by the following chemical equation and corresponding rate expression:

$$F_B^- + O \xrightarrow{k_2} F_B + R \tag{17}$$

$$r_2 = k_2 \Gamma_{F_B^-} C_{O,(x=0)} \tag{18}$$

where $C_{O,(x=0)}$ is the concentration of the oxidized form of the redox couple at the electrode surface, which requires that the rate constant k_2 carry units of [$cm^3 \cdot mol^{-1} \cdot s^{-1}$].

Similarly, the oxidation of a mediator in the reduced state by P_{700}^{+} is described by the following chemical equation and rate expression:

$$P_{700}^{+} + R \xrightarrow{k_3} P_{700} + O \tag{19}$$

$$r_3 = k_3 \Gamma_{P_{700}^{+}} C_{R,(x=0)} \tag{20}$$

where k_3 also carries units of [$cm^3 \cdot mol^{-1} \cdot s^{-1}$]. In addition to the above redox reactions, PSI's reaction centers can interact with the electrode surface directly, provided that the protein complexes are oriented such that their reaction centers are electronically accessible. The chemical equation that describes the electron transfer events between the F_B / F_B^- couple and the electrode is given by

$$F_B \xleftrightarrow[electrode]{k_{F_B}^0} F_B^- \tag{21}$$

where $k_{F_B}^0$ is the standard rate constant of the couple. The rate expressions for the oxidation of F_B^- and reduction of F_B by the electrode were obtained using a Butler-Volmer expression to account for the dependence of the rate upon the electrode potential to yield

$$r_4 = k_{F_B}^0 \exp\left[-\alpha_{F_B} f\left(E - E_{F_B}^{0'}\right)\right] \chi_{down} \Gamma_{F_B} \tag{22}$$

for the reduction of F_B by the electrode and

$$r_5 = k_{F_B}^0 \exp\left[\left(1-\alpha_{F_B}\right) f\left(E - E_{F_B}^{0'}\right)\right] \chi_{down} \Gamma_{F_B^-} \tag{23}$$

for the oxidation F_B^- of by the electrode, where χ_{down} is the fraction of PSI complexes oriented with their electron transport vectors pointing into the electrode, α_{F_B} is the transfer coefficient of the F_B / F_B^- redox couple, *f* is defined as *F/RT* and carries units of

[V^{-1}], and the term $\left(E - E_{F_B}^{0'}\right)$ is the difference between the formal potential for the redox couple and the applied electrode potential.[21] Similarly, the chemical equation describing the interactions of the P_{700}^{+} / P_{700} couple and the electrode can be written as

$$P_{700}^{+} \xleftarrow[electrode]{k_{P_{700}}^{0}} P_{700}, \tag{24}$$

which yields the Butler-Volmer rate expressions

$$r_6 = k_{P_{700}}^{0} \exp\left[-\alpha_{P_{700}} f\left(E - E_{P_{700}}^{0'}\right)\right] \chi_{up} \Gamma_{P_{700}^{+}} \tag{25}$$

and

$$r_7 = k_{P_{700}}^{0} \exp\left[\left(1-\alpha_{P_{700}}\right) f\left(E - E_{P_{700}}^{0'}\right)\right] \chi_{up} \Gamma_{P_{700}} \tag{26}$$

for the reduction P_{700}^{+} and oxidation of P_{700} by the electrode, respectively, where $k_{P_{700}}^{0}$ and $\alpha_{P_{700}}$ are the standard rate constant and transfer coefficient of the couple, respectively, and χ_{up} is the fraction of PSI complexes oriented with the electron transport chains pointing away from the electrode surface. These expressions describing the generation and consumption of PSI's reaction centers may be combined to yield the following time-dependent conservation statements for F_B^{-} and P_{700}^{+}, respectively:

$$\begin{aligned}\frac{d\Gamma_{F_B^-}}{dt} = {} & N_\lambda \theta_\lambda \eta_{IQ} k_{PG} \left(\Gamma_{PSI} - \Gamma_{P_{700}^{+}}\right)\left(\Gamma_{PSI} - \Gamma_{F_B^-}\right) + k_{F_B}^{0} \exp\left[-\alpha_{F_B} f\left(E - E_{F_B}^{0'}\right)\right] \chi_{down} \Gamma_{F_B} \\ & - k_2 \Gamma_{F_B^-} C_{O,(x=0)} - k_{F_B}^{0} \exp\left[(1-\alpha_{F_B}) f\left(E - E_{F_B}^{0'}\right)\right] \chi_{down} \Gamma_{F_B^-}\end{aligned} \tag{27}$$

$$\begin{aligned}\frac{d\Gamma_{P_{700}^{+}}}{dt} = {} & N_\lambda \theta_\lambda \eta_{IQ} k_{PG} \left(\Gamma_{PSI} - \Gamma_{P_{700}^{+}}\right)\left(\Gamma_{PSI} - \Gamma_{F_B^-}\right) + k_{P_{700}}^{0} \exp\left[\left(1-\alpha_{P_{700}}\right) f\left(E - E_{P_{700}}^{0'}\right)\right] \chi_{up} \Gamma_{P_{700}} \\ & - k_3 \Gamma_{P_{700}^{+}} C_{R,(x=0)} - k_{P_{700}}^{0} \exp\left[-\alpha_{P_{700}} f\left(E - E_{P_{700}}^{0'}\right)\right] \chi_{up} \Gamma_{P_{700}^{+}}\end{aligned} \tag{28}$$

Assuming that there is no photogeneration of these reaction centers before $t = 0$ yields the corresponding initial conditions

$$\Gamma_{F_B^-}\Big|_{t=0} = 0 \tag{29}$$

and

$$\Gamma_{P_{700}^+}\Big|_{t=0} = 0 \tag{30}$$

In order to completely specify the system, similar conservation statements must be developed for the concentrations of the reduced and oxidized form of the redox couple. Considering the electrode an infinite planar surface and assuming that no homogeneous reactions occur within the system, the 1-dimensional continuity equation for oxidized and reduced mediators, respectively, is given by

$$\frac{\partial C_O}{\partial t} = -D_O \frac{\partial^2 C_O}{\partial x^2} \tag{31}$$

and

$$\frac{\partial C_R}{\partial t} = -D_R \frac{\partial^2 C_R}{\partial x^2} \tag{32}$$

where the x is the dimension normal to the electrode surface, and D_O and D_R are the diffusion coefficients of the oxidized and reduced forms of the redox couple, respectively. Before any reactions take place, the concentrations of the reduced and oxidized forms of the redox couple are assumed equal to their initial bulk concentrations C_O^* and C_R^* everywhere within the electrolyte, which yields the initial conditions

$$C_O\big|_{t=0} = C_O^* \tag{33}$$

and

$$C_R\big|_{t=0} = C_R^* \tag{34}$$

The assumption that the concentrations of the redox couple very far away from the electrode surface remain unaffected by the heterogeneous reactions occurring at $x = 0$ yields the boundary conditions

$$C_O\big|_{x=\infty} = C_O^* \tag{35}$$

and

$$C_R\big|_{x=\infty} = C_R^* \tag{36}$$

The boundary conditions at the electrode surface are described by equating the flux of the redox couples at the electrode surface to the net rate of their heterogeneous electrochemical reactions. The reactions of the redox couple with the electrode surface directly can be described by the chemical equation

$$O \underset{electrode}{\overset{k_{RC}^0}{\longleftrightarrow}} R \tag{37}$$

with the corresponding rate equations

$$r_8 = k_{RC}^0 \exp\left[-\alpha_{RC} f\left(E - E_{RC}^{0'}\right)\right] C_{O,(x=0)} \tag{38}$$

and

$$r_9 = k_{RC}^0 \exp\left[\left(1-\alpha_{RC}\right) f\left(E - E_{RC}^{0'}\right)\right] C_{R,(x=0)} \tag{39}$$

where k_{RC}^0, α_{RC}, and $E_{RC}^{0'}$, are the standard rate constant, transfer coefficient, and formal potential of the redox couple, respectively. In dark conditions, the boundary conditions for equations (31) and (32) at the electrode surface are specified by equating the flux of the redox couple to the rates of the reactions described in equations (38) and (39); however, irradiation of the electrode initiates charge separation within PSI complexes at

the electrode surface, which prompts the redox reactions to occur between PSI's reaction centers and the redox couple as described by equations (9-12). Equating the surface reaction rate expressions (18), (20), (38), and (39) to the flux of the redox couple at the electrode surface, one obtains the boundary conditions for equations (31) and (32) at $x = 0$:

$$\begin{aligned} -D_O \left.\frac{\partial C_O}{\partial x}\right|_{x=0} &= k_{RC}^0 \exp\left[(1-\alpha_{RC})\, f\left(E - E_{RC}^{0'}\right)\right] C_{R,(x=0)} + k_3 \Gamma_{P_{700}^+} C_{R,(x=0)} \\ &\quad - k_{RC}^0 \exp\left[-\alpha_{RC}\, f\left(E - E_{RC}^{0'}\right)\right] C_{O,(x=0)} - k_2 \Gamma_{F_B^-} C_{O,(x=0)} \end{aligned} \tag{40}$$

$$\begin{aligned} -D_R \left.\frac{\partial C_R}{\partial x}\right|_{x=0} &= k_{RC}^0 \exp\left[-\alpha_{RC}\, f\left(E - E_{RC}^{0'}\right)\right] C_{O,(x=0)} + k_2 \Gamma_{F_B^-} C_{O,(x=0)} \\ &\quad - k_{RC}^0 \exp\left[(1-\alpha_{RC})\, f\left(E - E_{RC}^{0'}\right)\right] C_{R,(x=0)} - k_3 \Gamma_{P_{700}^+} C_{R,(x=0)} \end{aligned} \tag{41}$$

The time dependent solution of these equations can be used to back-calculate the net electron flux across the electrode/electrolyte interface. This electron flux corresponds to the current density that would be measured during a chronoamperometric experiment and is calculated as

$$j_{net} = F\left[\sum \text{rate of heterogenous reduction events} - \sum \text{rate of heterogenous oxidation events}\right] \tag{42}$$

$$= F\begin{pmatrix} k_{P_{700}}^0 \exp\left[-\alpha_{P_{700}}\, f\left(E - E_{P_{700}}^{0'}\right)\right] \chi_{up} \Gamma_{P_{700}^+} + k_{RC}^0 \exp\left[-\alpha_{RC}\, f\left(E - E_{RC}^{0'}\right)\right] C_{O,(x=0)} \\ + k_{F_B}^0 \exp\left[-\alpha_{F_B}\, f\left(E - E_{F_B}^{0'}\right)\right] \chi_{down} \Gamma_{F_B} - k_{F_B}^0 \exp\left[(1-\alpha_{F_B})\, f\left(E - E_{F_B}^{0'}\right)\right] \chi_{down} \Gamma_{F_B^-} \\ - k_{RC}^0 \exp\left[(1-\alpha_{RC})\, f\left(E - E_{RC}^{0'}\right)\right] C_{R,(x=0)} - k_{P_{700}}^0 \exp\left[(1-\alpha_{P_{700}})\, f\left(E - E_{P_{700}}^{0'}\right)\right] \chi_{up} \Gamma_{P_{700}} \end{pmatrix} \tag{43}$$

Note that this equation only contains contributions from electrochemical reactions that directly involve the electrode surface.

Experimental Data Set

To extract the kinetic parameters that govern the previously described model, we performed chronoamperometric experiments performed over a range of working electrode potentials (**Figure 4.4**). Equimolar concentrations of each species of the redox couple were used, and the resulting equilibrium potential of the electrolyte solution was observed to be 0.212 V vs. Ag/AgCl, which is very close to the formal potential of the redox couple (~0.227 V vs. Ag/AgCl)[9] as predicted by the Nernst Equation. Defining the overpotential as $\eta = E_W - E_{eq}$, where E_W is the working electrode potential and E_{eq} is the equilibrium potential, all experiments performed at positive overpotentials display an anodic (negative) baseline current, while those performed at negative overpotentials display a cathodic (positive) baseline current. The curvature observed in the current density measured during these experiments results from the formation of gradients in the concentration of the heterogeneous reactant that propagates away from the electrode as the reactant is consumed at the surface, and causes the current to decrease approximately as $t^{-1/2}$.[22] During each experiment, the electrode was irradiated from t = 50 -70 s. From these data, I observed that the direction and magnitude of the photocurrent depends upon the overpotential, with anodic responses observed at $\eta \leq$ -0.022 V, and cathodic responses at $\eta \leq$ -0.042 V.

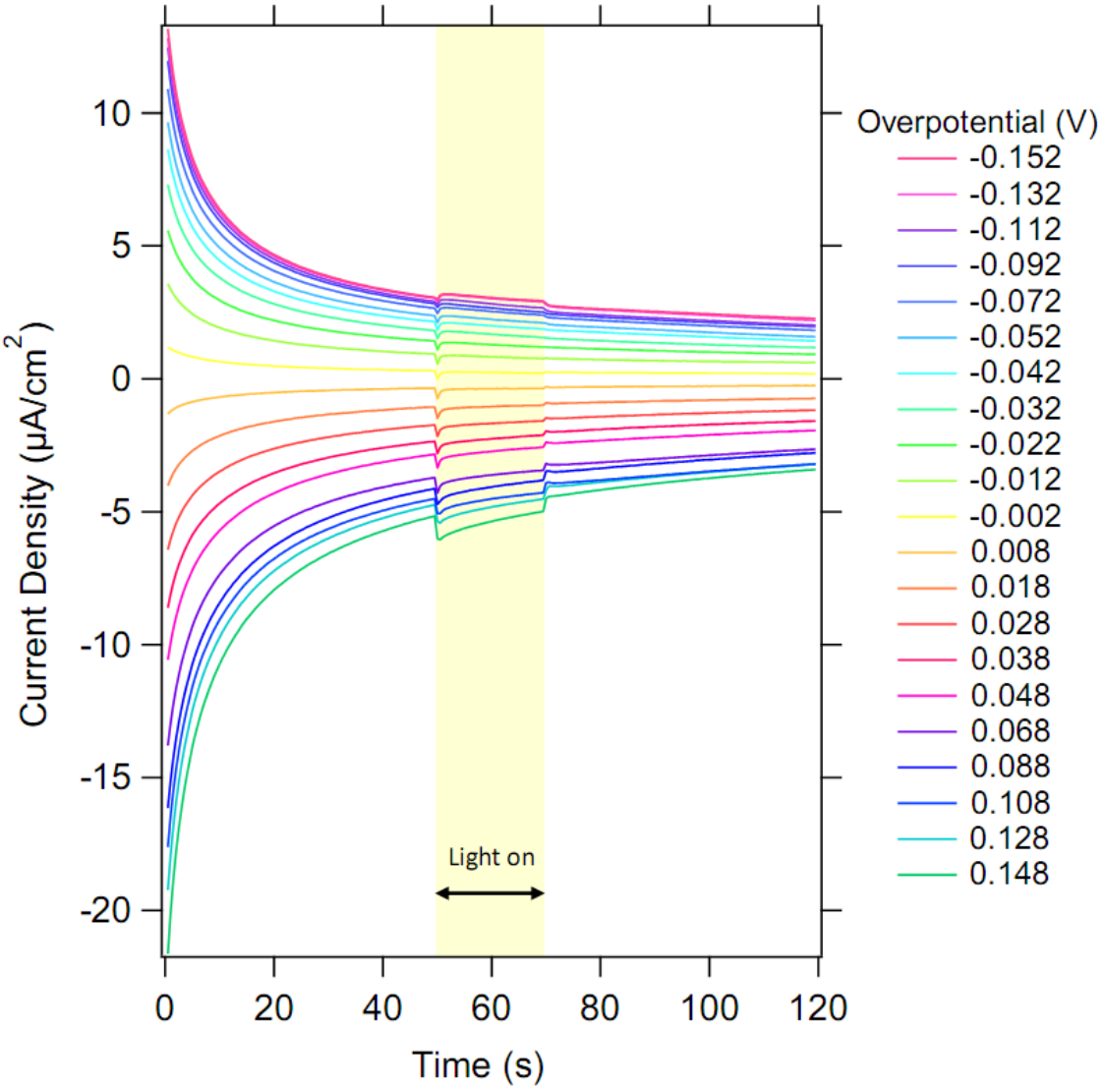

Figure 4.4. Experimental Data Set. Chronoamperometric experiments were performed over a range of overpotentials using a working electrode modified with a PSI monolayer. Irradiation of the electrode produced photocurrents whose magnitude and direction were dependent on the overpotential. Negative overpotentials cause positive, or cathodic, baseline currents to flow, while positive overpotentials induce negative, or anodic, baseline currents. Kinetic parameters were empirically obtained from this data set by iteratively varying the parameters to minimize the residual between the simulated and experimental current densities.

Numerical Solution and Parameter Extraction Results

This system of partial differential equations was solved using Matlab's numerical PDE solver `pdepe`. The solutions to these equations are surfaces that correspond to the concentrations of the reduced and oxidized forms of the redox couple throughout space and time (**Figure 4.5**). The surface concentrations, i.e. the concentrations at $x = 0$, obtained from the solutions to these equations were used to calculate a simulated current density by equation (43). Kinetic parameters were extracted from experimental data by using the Matlab function `fminsearch` to minimize the residual between the measured current density and the simulated current density at corresponding conditions by iteratively varying the unknown kinetic parameters in the model. Parameters were obtained from the experiments performed at each overpotential, and the mean and standard deviations of these parameters are presented in **Table 4.1**.

Table 4.1 Extracted Parameters

Parameter	Chemical Equation	Parameter Value [units]
k_{PG}	$P_{700} + F_B + h\nu \xrightarrow{k_{PG}} P_{700}^+ + F_B^-$	1.8 ± 0.5 x 10^{23} [$cm^4 \cdot mol^{-2}$]
k_{RC}^0	$O \xleftarrow[electrode]{k_{RC}^0} R$	9.6 ± 0.5 x 10^{-4} [$cm \cdot s^{-1}$]
$k_{F_B}^0$	$F_B^- \xleftarrow[electrode]{k_{F_B}^0} F_B$	53 ± 4 [s^{-1}]
$k_{P_{700}}^0$	$P_{700}^+ \xleftarrow[electrode]{k_{P_{700}}^0} P_{700}$	1.2 ± 0.1 x 10^2 [s^{-1}]
k_2	$F_B^- + O \xrightarrow{k_2} F_B + R$	7.8 ± 2.0 x 10^{11} [$cm^3 \cdot mol^{-1} \cdot s^{-1}$]
k_3	$P_{700}^+ + R \xrightarrow{k_3} P_{700} + O$	7.4 ± 0.6 x 10^{11} [$cm^3 \cdot mol^{-1} \cdot s^{-1}$]
$E^{0'}_{P_{700}^+/P_{700}}$	-	0.66 ± 0.14 [V vs Ag/AgCl]
$E^{0'}_{F_B/F_B^-}$	-	-0.27 ± 0.17 [V vs Ag/AgCl]

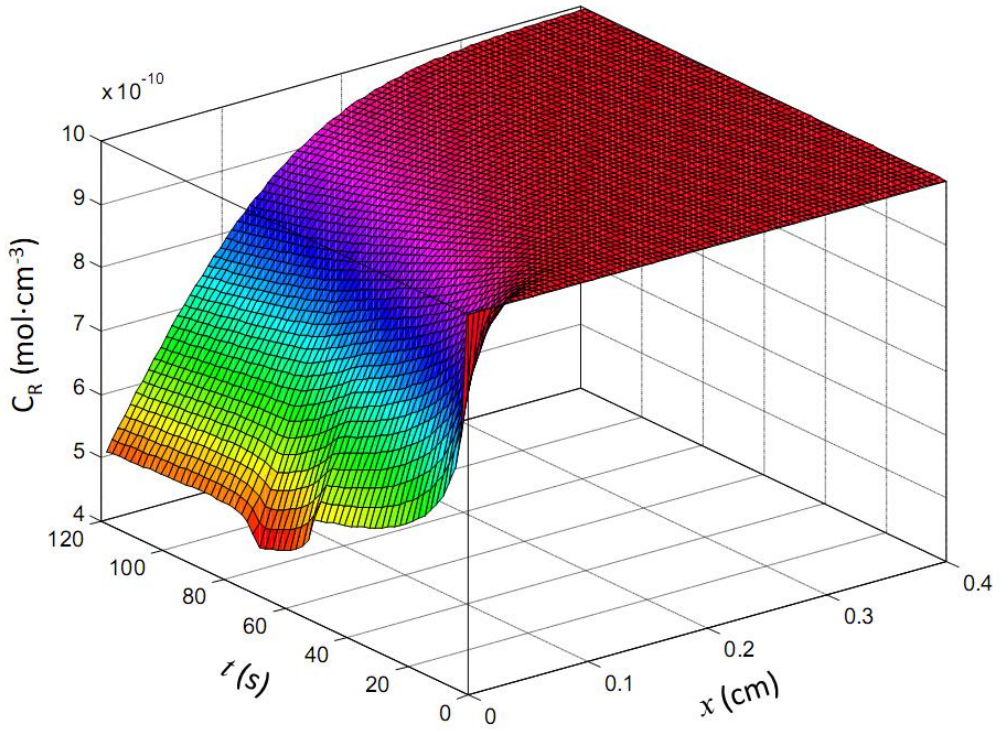

Figure 4.5. Representative Solution to the PDE System. The surface plot shows the solution to the PDE system for the reduced form of the mediator during the simulation of a chronoamperometric experiment of 120 s at a potential of 0.34 V vs Ag/AgCl. Far from the electrode surface, the concentration remains equal to the bulk concentration. At the electrode surface, the concentration decreases due to the heterogeneous consumption of the reactant as current is generated. A faster decay in concentration is observed at x = 0 when the electrode is irradiated (t = 50 – 70 s) due to consumption of the reactant by PSI. This simulation was performed with C_R^* = 1 x 10^{-9} mol/cm^3 to highlight the effect of photocurrent generation on the concentration of the redox couple.

First, kinetic parameters that described the heterogeneous reaction of the redox couple only (i.e. k_{RC}^0 and α_{RC}, the standard rate constant and the charge transfer coefficient of the redox couple, respectively) were obtained from experimental periods during which the electrode was not irradiated. These "dark" experimental conditions allowed for the kinetics that governed the redox couple/electrode reactions to be de-

coupled from interactions between the photogenerated reaction centers of PSI. The standard rate constant for the $K_3Fe(CN)_6/K_4Fe(CN)_6$ in the present system was determined to be $9.6 \pm 0.5 \times 10^{-4}$ cm·s^{-1}, which is lower than previously reported values of $3 – 31 \times 10^{-3}$ cm·s^{-1} for this parameter in similar electrochemical systems at unmodified gold electrodes.[23] Previous studies of the transfer coefficient of the $K_3Fe(CN)_6/K_4Fe(CN)_6$ redox couple in similar systems have reported an overpotential dependence of this parameter, and have developed linear empirical relationships for α_{RC} and the overpotential, η, of the form $\alpha_{RC} = a\eta + b$, with *a* and *b* values ranging from 0.72 – 1.16 V^{-1} and 0.44 – 0.5 respectively.[23-25] Empirically determined values for α_{RC} obtained from the experiments in this work also exhibited an approximately linear dependence on overpotential at small values of η; however, asymptotic behavior was observed at larger overpotentials. To account for this departure from linearity at larger overpotentials, the empirically determined transfer coefficients were fit to a logistic function of the form

$$\alpha_{RC} = \frac{a}{1+\exp\left[-\left(b+c\eta\right)\right]} + d \qquad (44)$$

and the best fit parameters obtained were $a = 0.67$, $b = 1.4$, $c = 45$, and $d = 0.14$. The empirically determined values of α_{RC} are plotted with the logistic model in **Figure 4.6**. The low standard rate constant and strong overpotential dependence of the transfer coefficient observed in this system compared to previously reported values for these parameters for this redox couple at unmodified gold electrodes could be due to electrochemical impedance imparted to the present system by the adsorbed SAM/protein film.

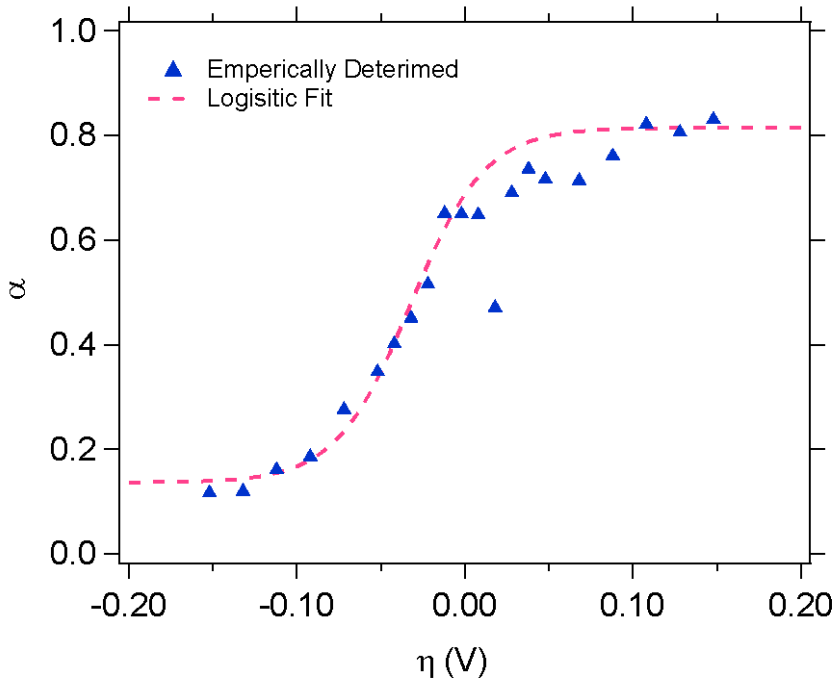

Figure 4.6. Overpotential Dependence of the Transfer Coefficient. Empirically determined values of the transfer coefficient displayed an approximately linear dependence on overpotential at small values of η with asymptotic behavior at larger overpotentials. A logistic function was used to represent these trends.

Once the kinetic parameters that described the heterogeneous reactions of the redox couple were obtained, they were input into the simulation to allow the extraction of the kinetic parameters that governed the reactions involving the photogenerated reaction centers of PSI. The "light" parameters were similarly extracted from the chronoamperometric data by fitting the experiments performed at each potential individually. **Figure 4.7a and b** shows representative experimental data plotted with the simulated current densities obtained using the empirical parameters extracted from the data. One limitation of the present model is that non-faradaic currents associated with charging and reordering of the electronic double layer in response to changes in the local

electronic environment at the electrode surface are not accounted for. These non-faradaic phenomena likely account for disparities between experimental and simulated current densities observed immediately following the onset of irradiation as shown in Figure 4.7a and b. Once parameters were individually obtained from the experiments performed at each overpotential investigated, their mean values (reported in Table 4.1) were input back into the simulation and used to generate a surface plot that displays the simulated current density over the entire range of overpotentials. This plot is presented in Figure 4.7c and the experimental data, also plotted as a surface, are shown in Figure 4.7d.

With the exception of the formal potentials of the P_{700} and F_B reaction centers of PSI (denoted $E^{0'}_{P_{700}^+/P_{700}}$ and $E^{0'}_{F_B/F_B^-}$, respectively), the units of the extracted parameters prohibit their direct comparison to previously reported values in the literature as a result of the nature of the mechanistic model employed in this work. The aforementioned formal potentials were determined to be +0.69 ± 0.14 and -0.28 ± 0.17 V vs. Ag/AgCl for $E^{0'}_{P_{700}^+/P_{700}}$ and $E^{0'}_{F_B/F_B^-}$, respectively. These values are ~ 400 mV more positive than previous reports of these parameters as determined by electron paramagnetic resonance[15] (EPR) and optical redox titrations[26]; however, previous electrochemical measurements of these parameters from PSI in lipid films on electrode surfaces[27] yielded values that were 200 – 300 mV more positive than those obtained by other techniques, and the positive shift was attributed to the changes in local electronic environment of the reaction centers imparted by the polarized electrode and electronic double layer at the electrode/electrolyte interface. As these non-faradic electrochemical processes are neglected in the present model, they are likely responsible for the observation of the positive shift observed in the formal potentials of the reaction centers

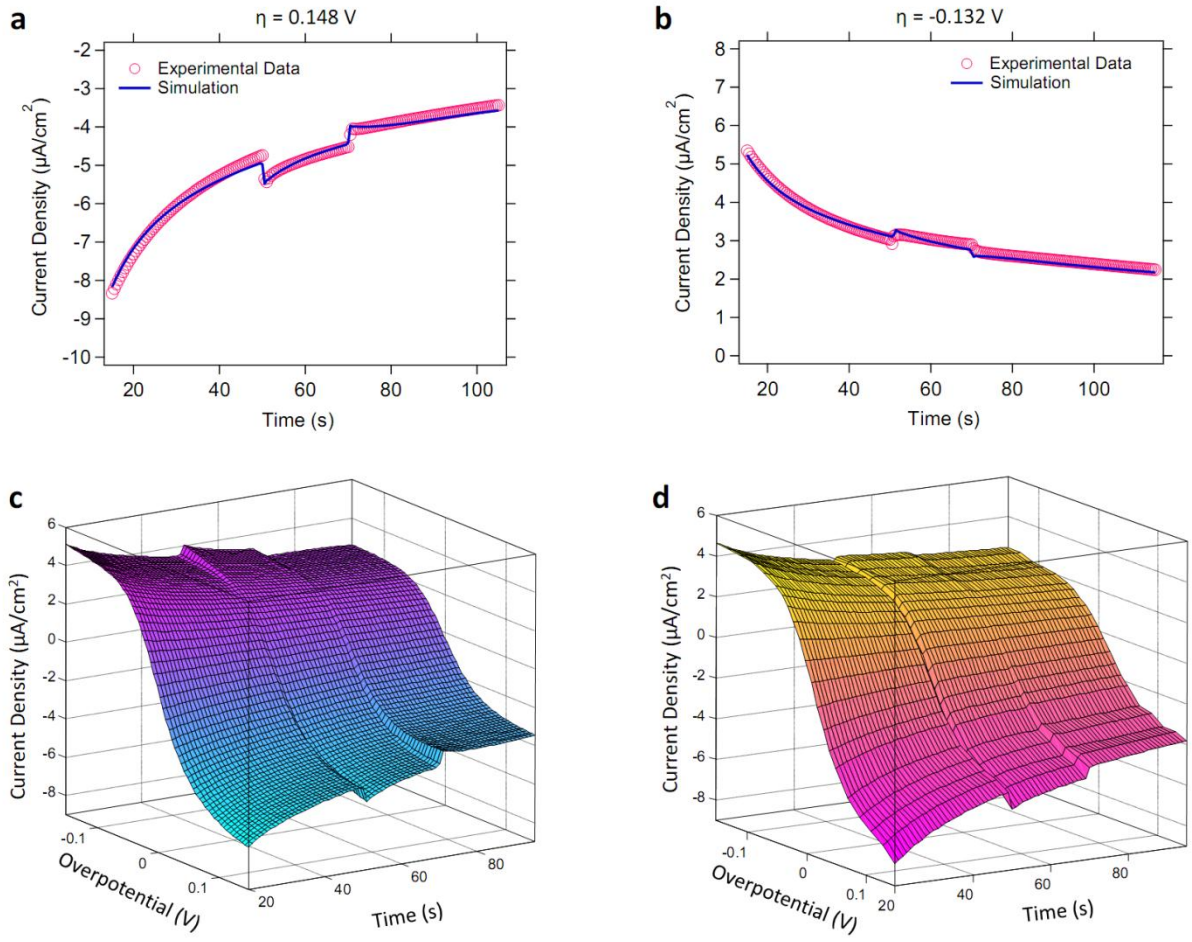

Figure 4.7. Comparison of Simulated and Experimental Current Densities. Simulated current densities produced using parameters extracted from corresponding chronoamperometric experiments are shown in **a** and **b**. Parameters were obtained from each chronoamperometric experiment individually and their mean averages were input into the simulation and used to generate a surface plot that describes the current density continuously over the range of investigated potentials **(c)**. The experimental data are shown as a surface plot for comparison in **(d)**.

of PSI obtained by comparing this simulation to the experimental data set. Nevertheless, the energetic difference between the formal potentials of the reactions centers obtained in this work of ~ 1 V remains consistent with those obtained by other methods in different systems.

Current Contributions and PSI Orientation

Once the simulation parameters were obtained from the experimental data, the simulation was used to investigate the contribution of the various heterogeneous electrochemical reactions to the net current density of the system. The net current density as calculated by equation (43) can be decomposed into contributions of reduction and oxidation of the redox couple, given by equations (38) and (39), respectively, reduction and oxidation of P_{700} reaction centers, given by equations (25) and (26), respectively, and reduction and oxidation of F_B iron-sulfur complexes, given by equations (22) and (23), respectively. This effect was investigated by calculating the individual current density contributions for a simulation performed at an overpotential of 0.088 V using the empirical parameters obtained from the corresponding experiment individually rather than the average parameters in order to more accurately reflect the photocurrent contributions (**Figure 4.8a**). At this overpotential, a net anodic current flows but still contains a cathodic contribution from reduction of the redox couple. Both experiment and simulation display a net anodic photocurrent production at this overpotential; however, the simulation predicts large photocurrent contributions from the PSI film in both anodic and cathodic directions, with a slightly stronger response in the anodic

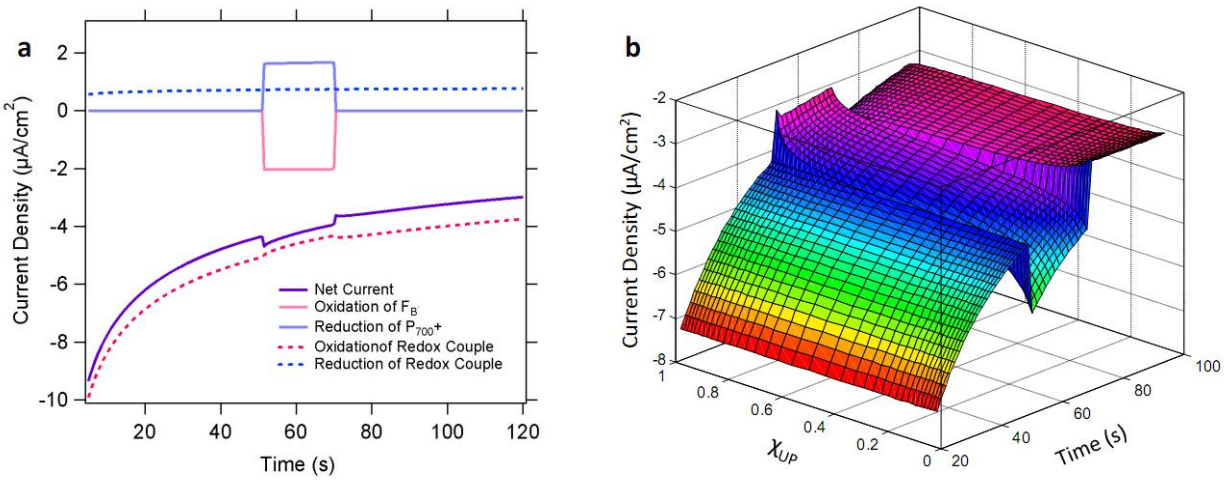

Figure 4.8 Current Density Contributions and Effect of PSI Orientation. (a) At overpotentials where both anodic and cathodic current components contribute to the net current density, the simulation predicts that the majority of the photocurrent produced by the PSI monolayer cancels because of its opposite direction. The simulation shown in (a) was performed using an overpotential of 0.088 V. **(b)** The orientation factors of PSI was varied from $\chi_{up} = 0$ to 1, assuming that $\chi_{up} + \chi_{down} = 1$ in the chronoamperometric simulation at $\eta = 0.088$ V. The model predicts that the net photocurrent density is dictated predominantly by kinetics at this overpotential for orientations between 20% and 80%; however, orienting ≥ 90% of the PSI complexes in a single configuration will produce significant enhancements to photocurrent even at overpotentials where oxidation and reduction of the reaction centers of PSI are both favorable.

direction that gives rise to the anodic net photocurrent. To provide further insight into these competing photocurrents, the effect of the orientation of the PSI complexes on the net photocurrent was investigated by varying the orientation fractions, χ_{up} and χ_{down}. The same simulation at an overpotential of 0.088 V was performed while varying χ_{up}, the fraction of PSI complexes oriented such that their P_{700} reaction centers were electronically accessible to the electrode, from 0 – 1, and the predicted current densities are presented in **Figure 4.8b**. These results show relatively small net photocurrents when only 20% - 80% of the PSI complexes are similarly oriented due to the competing directionalities of the photocurrents, while considerably larger photocurrents are

predicted in both anodic and cathodic directions when 90% or more of the PSI complexes are similarly oriented. These results suggest that net photocurrent is dictated predominantly by electrochemical kinetics in the 20% - 80% orientation regime, but that similarly orienting $\geq$ 90% of the PSI complexes will produce significant photocurrent enhancements even at photocurrents at which the heterogeneous reduction of P_{700}^{+} and oxidation of F_B^{-} are both energetically feasible. This analysis predicts that achieving high degrees of orientation in PSI monolayer systems will produce orders of magnitude more photocurrent than a system in which PSI complexes are randomly oriented and suggests the demonstration of this large photocurrent enhancement as an evidential criterion for orientation strategies claimed to produce orientations of $\geq$ 90%.

Conclusions

In summary, we have developed a mechanistic, kinetic model for the photocurrent production by an electrode modified by a PSI monolayer in the presence of a redox couple. Kinetic and electrochemical parameters were obtained by minimizing the residual between the current densities predicted by the model to chronoamperometric experiments performed over a range of overpotentials. The empirically obtained parameters that described the behavior of the system in dark conditions predicted current densities that were in good agreement with the experimental data; however, the charge transfer coefficient of the redox couple exhibited a strong overpotential dependence. Parameters describing the photoelectrochemical behavior of PSI were also obtained, and the average values of these parameters were used to yield a model that was continuous over the range overpotentials investigated. The completed simulation was then used to

investigate contributions to the current density, predicting that the majority of the photocurrent produced by the PSI monolayer cancels unless ~ 80% or more of the protein complexes are oriented in a similar configuration.

Experimental

Photosystem I Extraction

PSI-40 complexes were extracted from commercial baby spinach as described previously,[28] and then purified by an additional dialysis step. To briefly summarize the procedure, thylakoid membranes were isolated via maceration followed by centrifugation using the method of Reeves *et al.*[29] with several adaptations.[30] PSI complexes were then separated from the thylakoid membranes by additional centrifugation followed by purification using a chromotagraphic column packed with hydroxylapatite.[31, 32] The column effluent was then dialyzed in deionized water for 24 h using 10,000 MWCO dialysis tubing (Spectrapore). The total chlorophyll concentration of the product was determined by the method of Porra *et. al.*[33] to be 7.1×10^{-5} M with a Chl *a* / Chl *b* ratio of 3.3, and the P_{700} concentration was determined using the method of Baba *et. al.*[31] to be 1.6×10^{-6} M, yielding a Chl/P_{700} ratio of 43.

PSI-Modified Electrode Preparation

Au/Si substrates were prepared by thermally evaporating 125 nm of Au (J&J Materials) onto silicon wafers (Montico Silicon, <100> orientation, 100 mm diameter, 500-550 mm thick) with a 10 nm adhesion layer of Cr (R.D. Mathis). Samples were cut

to approximately 1.3 cm x 2 cm. The gold surface was then modified with an aminoethanethiol/TPDA SAM as described in Chapter 3. Dense, covalently attached PSI monolayers were formed via solution adsorption, whereby the modified gold surface was exposed to the dialyzed PSI suspension for 48 h, after which it was rinsed with deionized water and dried with nitrogen.

Photoelectrochemical Characterization

All electrochemical measurements were taken with a CH Instruments CHI660a electrochemical workstation equipped with a Faraday cage. Experiments were performed using a custom-made electrochemical cell in a three-electrode configuration, with the PSI-modified substrate serving as the working electrode, an Ag/AgCl reference electrode, and a Pt mesh counter electrode. The electrolyte solution consisted of 100 μM $K_3Fe(CN)_6$, 100 μM $K_4Fe(CN)_6$, and 0.1 M KCl in pH 7 phosphate buffered solution. The light source employed was a Gebrauch KL 2500 LCD lamp, and a red filter was employed to minimize background photocurrent contributions from the mediator solution. The power output of this light source was measured using an Ophir Orion-TH power meter equipped with a thermal detector head, and the emission spectrum was collected using an Ocean Optics USB 2000 fiber optic spectrometer.

Works Cited

1. Ciobanu, M., et al., *Electrochemistry and photoelectrochemistry of photosystem I adsorbed on hydroxyl-terminated monolayers.* Journal of Electroanalytical Chemistry, 2007. **599**(1): p. 72-78.

2. Faulkner, C.J., et al., *Rapid Assembly of Photosystem I Monolayers on Gold Electrodes.* Langmuir, 2008. **24**(16): p. 8409-8412.

3. Ciesielski, P.N., et al., *Functionalized Nanoporous Gold Leaf Electrode Films for the Immobilization of Photosystem I.* Acs Nano, 2008. **2**(12): p. 2465-2472.

4. Terasaki, N., et al., *Fabrication of novel photosystem I-gold nanoparticle hybrids and their photocurrent enhancement.* Thin Solid Films, 2006. **499**(1-2): p. 153-156.

5. Proux-Delrouyre, V., et al., *Electrocatalytic investigation of light-induced electron transfer between cytochrome c(6) and photosystem I.* Journal of the American Chemical Society, 2003. **125**(45): p. 13686-13692.

6. Ke, B., *Photoreduction Sites for 2,6-Dichlorophenolindophenol in Chloroplasts.* Plant Physiology, 1967. **42**(9): p. 1310-&.

7. Lee, J.W. and E. Greenbaum, *Bioelectronics and Biometallocatalysis for Production of Fuels and Chemicals by Photosynthetic Water-Splitting.* Applied Biochemistry and Biotechnology, 1995. **51-2**: p. 295-305.

8. Lee, J.W., R.T. Collins, and E. Greenbaum, *Molecular ionic probes: A new class of hill reagents and their potential for nanofabrication and biometallocatalysis.* Journal of Physical Chemistry B, 1998. **102**(11): p. 2095-2100.

9. Kolthoff, I.M. and W.J. Tomsicek, *The Oxidation Potential of the System Potassium Ferrocyanide-Potassium Ferricyanide at Various Ionic Strengths.* The Journal of Physical Chemistry, 1935. **39**(7): p. 945-954.

10. Amunts, A., O. Drory, and N. Nelson, *The structure of a plant photosystem I supercomplex at 3.4 Å resolution.* Nature, 2007. **447**(7140): p. 58-63.

11. Deen, W.M., *Analysis of Transport Phenomena*. 1998, Oxford, NY: Oxford University Press.

12. Boekema, E.J., R.M. Wynn, and R. Malkin, *The Structure of Spinach Photosystem-I Studied by Electron-Microscopy.* Biochimica Et Biophysica Acta, 1990. **1017**(1): p. 49-56.

13. Fotiadis, D., et al., *Surface analysis of the photosystem I complex by electron and atomic force microscopy.* Journal of Molecular Biology, 1998. **283**(1): p. 83-94.

14. Lee, J.W., et al., *Chemical Platinization and Its Effect on Excitation Transfer Dynamics and P700 Photooxidation Kinetics in Isolated Photosystem-I.* Biophysical Journal, 1995. **69**(2): p. 652-659.

15. Brettel, K., *Electron transfer and arrangement of the redox cofactors in photosystem I.* Biochimica et Biophysica Acta (BBA) - Bioenergetics, 1997. **1318**(3): p. 322-373.

16. Brettel, K. and W. Leibl, *Electron transfer in photosystem I.* Biochimica Et Biophysica Acta-Bioenergetics, 2001. **1507**(1-3): p. 100-114.

17. Nelson, N. and C.F. Yocum, *Structure and function of photosystems I and II.* Annual Review of Plant Biology, 2006. **57**: p. 521-565.

18. Trissl, H.-W. and C. Wilhelm, *Why do thylakoid membranes from higher plants form grana stacks?* Trends in Biochemical Sciences, 1993. **18**(11): p. 415-419.

19. Müh, F. and A. Zouni, *Extinction coefficients and critical solubilisation concentrations of photosystems I and II from Thermosynechococcus elongatus.* Biochimica et Biophysica Acta (BBA) - Bioenergetics, 2005. **1708**(2): p. 219-228.

20. Lee, J.W., *Excitation transfer dynamics and P700 photooxidation kinetics in isolated photosystem I.* 1993, Cornell University: Ithaca, NY.

21. Bard, A.J. and L.R. Faulkner, *Electrochemical Methods: Fundamentals and Applications*. 2nd ed. 2001, New York: Wiley

22. Cottrell, F.G., Z.Physik.Chem, 1902. **42**(385).

23. Marecek, V., Z. Samec, and J. Weber, *The dependence of the electrochemical charge-transfer coefficient on the electrode potential: Study of the Fe(CN)63-/Fe(CN)64- redox reaction on polycrystalline Au electrode in KF solutions.* Journal of Electroanalytical Chemistry, 1978. **94**(3): p. 169-185.

24. Randles, J.E.B. and S.K. W., *Kinetics of rapid electrode reactions. Part 3.—Electron exchange reactions.* Transactions of the Faraday Society, 1952. **48**: p. 937-950.

25. Angell, D.H. and T. Dickinson, *The kinetics of the ferrous/ferric and ferro/ferricyanide reactions at platinum and gold electrodes : Part I. Kinetics at bare-metal surfaces.* Journal of Electroanalytical Chemistry, 1972. **35**: p. 55-72.

26. Jordan, R., U. Nessau, and E. Schlodder, *Photosynthesis: Mechanism and effects*, ed. G. Garab. Vol. 1. 1998, Dordrecht: Kluwer Academic Publishers.

27. Munge, B., et al., *Electron Transfer Reactions of Redox Cofactors in Spinach Photosystem I Reaction Center Protein in Lipid Films on Electrodes.* Journal of the American Chemical Society, 2003. **125**(41): p. 12457-12463.

28. Kincaid, H.A., et al., *Entrapment of photosystem I within self-assembled films.* Langmuir, 2006. **22**(19): p. 8114-8120.

29. Reeves, S.G. and D.O. Hall, *Higher Plant Chloroplasts and Grana: General Preparative Procedures (Excluding High Carbon Dioxide Fixation Ability Chloroplasts).* Methods in Enzymology, 1980. **69**: p. 85-94.

30. Ciobanu, M., et al., *Photosystem I Patterning Imaged by Scanning Electrochemical Microscopy.* Langmuir, 2005. **21**: p. 692-698.

31. Baba, K., et al., *Photoinhibition of photosystem I electron transfer activity in isolated photosystem I preparations with different chlorophyll contents.* Photosynthesis Research, 1996. **47**(2): p. 121-130.

32. Shiozawa, J.A., R.S. Alberte, and J.P. Thornber, *P700-Chlorophyll a-Protein - Isolation and Some Characteristics of Complex in Higher Plants.* Archives of Biochemistry and Biophysics, 1974. **165**(1): p. 388-397.

33. Porra, R.J., *The chequered history of the development and use of simultaneous equations for the accurate determination of chlorophylls a and b.* Photosynthesis Research, 2002. **73**(1-3): p. 149-156.

CHAPTER V

SELF-CONTAINED PHOTOSYSTEM I-BASED BIOHYBRID PHOTOELECTROCHEMICAL CELLS

Introduction

The PSI-based photoelectrochemical systems discussed thus far have consisted of PSI-modified substrates that were incorporated into electrochemical cells as the working electrode and biased using a potentiostat for the purpose of characterization. In order to demonstrate the feasibility of PSI-based solar energy conversion technologies, a device should be constructed that produces photovoltage and photocurrent without the voltage bias provided by a potentiostat, and is "self-contained" in that the device includes the supplemental electrochemical components previously provided by the characterization cell (i.e. the counter electrode and electrolyte solution). In this chapter, I report the development of such a self-contained device, a photoelectrochemical cell in which a multilayer film of PSI complexes is assembled on the surface of the cathode to produce a photocatalytic effect that drives an electrical current through the cell. I describe how the multilayered protein film may be assembled within the device via a simple, single-step injection process that does not require the use of expensive platinum salts or genetic mutations as did previously reported PSI multilayer fabrication procedures.[1] I describe the relationship between the current and voltage production of the cells and the photoinduced interactions of PSI complexes with electrochemical mediators, and show that the performance of the device is limited by diffusional transport of the electrochemical mediators through the electrolyte. Finally, the long-term stability of the

device is investigated, and I show that the device continues to produce photocurrent for at least 9 months.

Methods

Cell Fabrication.

A schematic of the photoelectrochemical cell is shown in **Figure 5.1**. The base of the cell serves as the cathode and consists of a ~125 nm thick gold layer (J&J Materials) that was thermally deposited onto a silicon support (Montico Silicon, <100> orientation). The anode consists of indium tin oxide (ITO)-coated polyethylene terephthalate (Aldrich), and was modified with a small strip of copper tape (3M) on the surface of the ITO to facilitate the lateral conduction of electrons across the counter electrode. A spacer layer of polydimethylsiloxane (PDMS) (Sylgard) separates the two electrodes and effectively forms a small reservoir sandwiched between the two conductive surfaces. An aqueous electrolyte solution of 5 mM dichloroindophenol (DCIP) (Aldrich), 100 mM ascorbic acid (Asc) (TCI America), and 100 mM NaCl (Fisher) in 5 mM pH 7 phosphate buffer (Fisher) was injected into the reservoir until it was approximately half-filled. The oxidized form of the reversible DCIP/DCIPH_2 redox couple that is present in mixtures of DCIP and Asc[2] is a known oxidant of F_B^-,[3] and the reduced form is known to reduce P_{700}^+.[4] Next, a buffer solution containing ~9 μM PSI complexes suspended by Triton-X 100 surfactant (0.05% wt/vol, Acros), 0.14 M Na_2HPO_4 (Fisher), 0.14 M NaH_2PO_4 (Fisher) in 0.2 M pH 7 phosphate buffer (Fisher) was similarly injected into the cell until the reservoir was filled. The total volume of the reservoir of a typical cell used in this study was approximately 100 μL. Following injection, PSI complexes in

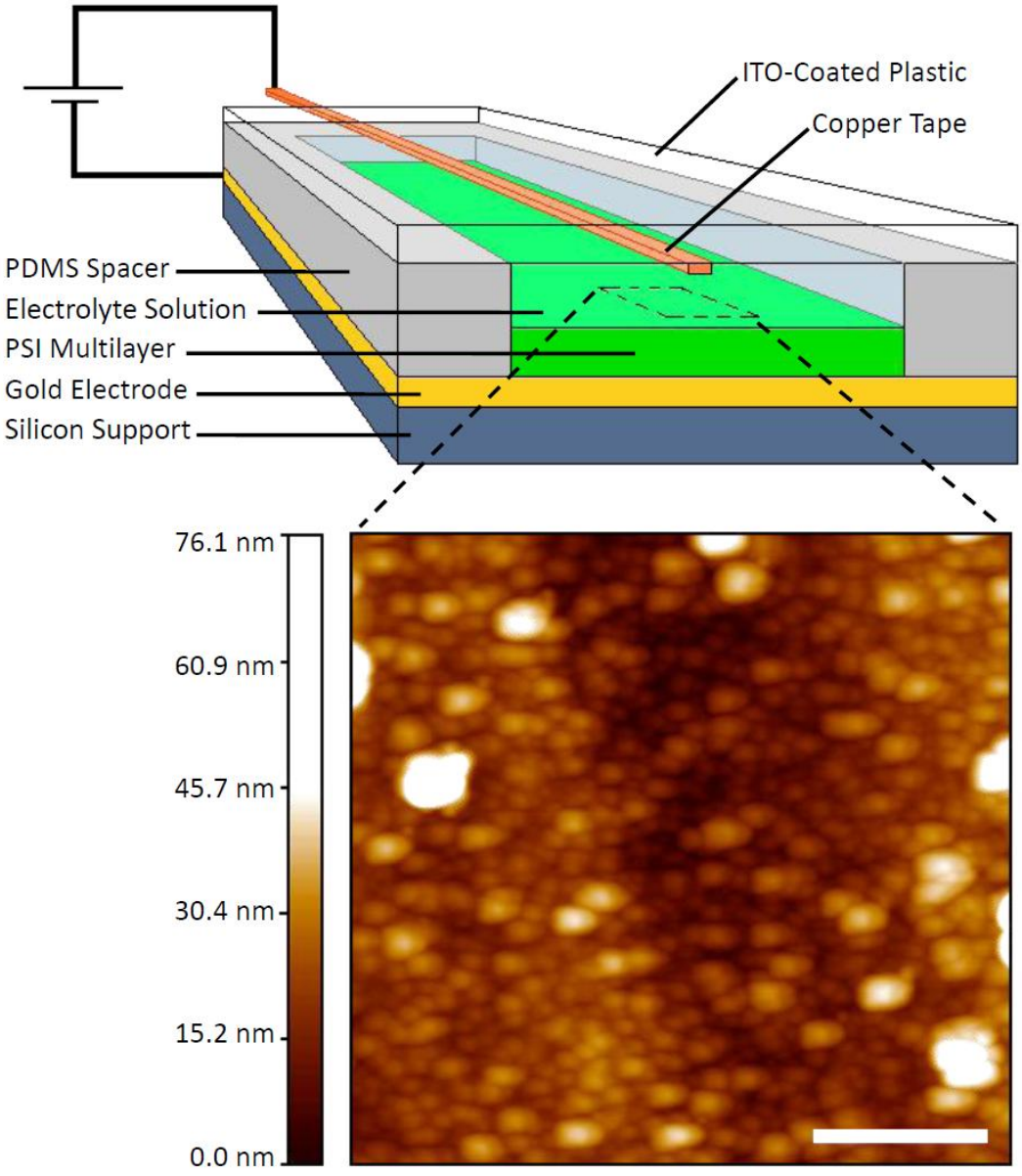

Figure 5.1. Schematic of a PSI-Catalyzed Photoelectrochemical Cell. Inset: AFM image of the surface of a PSI multilayer from a disassembled cell, scale bar 500 nm.

solution assemble at the gold surface over a period of several days, after which the dense multilayer can be seen as a green film on the electrode surface. The inset of Figure 5.1 shows an AFM image of a PSI multilayer from the surface of the cathode of a disassembled cell that was rinsed with DI water and dried with nitrogen. The roughly spherical particles shown in this image vary in diameter from ~10 nm, that is similar to previously reported values of the major axis of PSI complexes,[5] up to several hundred nanometers for the larger particles, that are likely protein/surfactant agglomerates that formed in solution and deposited onto the surface. The PSI multilayer films were typically 1-2 μm thick as measured by profilometry. We have estimated the materials cost for a cell with 1 cm^2 of active electrode area as approximately 10 cents.

Photosystem I Extraction.

PSI-40 particles were extracted as described in the Methods section of Chapter III of this document.

Atomic Force Microscopy.

The AFM image presented in the inset of Figure 5.1 was obtained from the surface of a PSI multilayer that was formed on the cathode of a cell. The cell had been operational for at least 3 weeks before it was disassembled, and the cathode was washed with de-ionized water and dried with nitrogen prior to imaging. AFM images were collected with a JSPM-5200 scanning probe microscope operated in tapping mode. The image presented in Figure 5.1 was obtained from an area of 2.0 x 2.0 μm at a clock speed of 166.7 μs using a feedback filter at a frequency of 1.2 Hz and a loop gain of 8.

Reflectance-Absorption Infrared Spectroscopy.

Spectra were collected with a Bio-Rad Excalibur FTS-3000 infrared spectrometer operated in single reflection mode using p-polarized light at an incident angle approximately 80° from the surface normal; three hundred scans were accumulated for each sample.

Proflilomtetry.

Profilometric thicknesses were obtained using DEKTAK 150 Surface Profiler by performing line scans using a stylus force of 1 mg at a scan rate of 2.5 $\mu m \cdot s^{-1}$ starting near the edge of the multilayer from the cathodes of disassembled cells and proceeding into the film.

Photoelectrochemical Characterization.

All electrochemical measurements were taken with a CH Instruments CHI660a electrochemical workstation equipped with a Faraday cage. The working electrode clip was attached to the gold layer on the cell base, and the counter and reference electrodes were clipped to the copper strip on the ITO-coated cover. The light source employed was a Gebrauch KL 2500 LCD lamp, and the intensity output from six different settings on this lamp was measured with a Coherent Radiation 210 Power Meter by positioning the detector in front of the source at a distance of 1 cm. Samples were also positioned ~1 cm away from the source during characterization to ensure consistent light intensities were reaching the devices. Chronoamperometric data were collected at zero bias between the reference and working electrodes.

Reflectance-Absorption Infrared Spectroscopy

In order to differentiate the PSI multilayer films employed in this device and the PSI-monolayers previously reported, the absorbance in the Amide I and II bands (1666-1669 and 1545-1547 cm^{-1} respectively) of the RAIR spectrum of a PSI monolayer, prepared as described previously,[6] was compared to the absorbance in the same region for a PSI film on the cathode of a disassembled cell (**Figure 5.2**). Previously, we have shown that the peak absorbance of the Amide I band is related to the average film thickness of PSI monolayers as measured by spectroscopic ellipsometry, and could thus be used to aid in the assessment of surface coverage of PSI.[7] The multilayer films within the devices described in this chapter are too thick and rough to obtain accurate thickness measurements via ellipsometry; however, the absorbance of the Amide I and II bands is greatly enhanced with respect to that of a PSI monolayer, indicating that significantly more protein is present on the surface of the disassembled cell than a surface modified with a PSI monolayer.

Profilometry

In order to determine the approximate thickness of the PSI film assembled within the device, profilometry was performed on the cathode of a disassembled cell (**Figure 5.3**). A line scan was collected starting near the edge of the multilayer and proceeding into the film. The film thickness was found to be 1.25 ± 0.6 μm based on the mean and standard deviation of the height of the film recorded by the profilometer. While the AFM image shown in the inset of Figure 5.1 reveals that the nanoscale features of the surface of the film are dominated by roughly spherically shaped particles with diameters ranging from

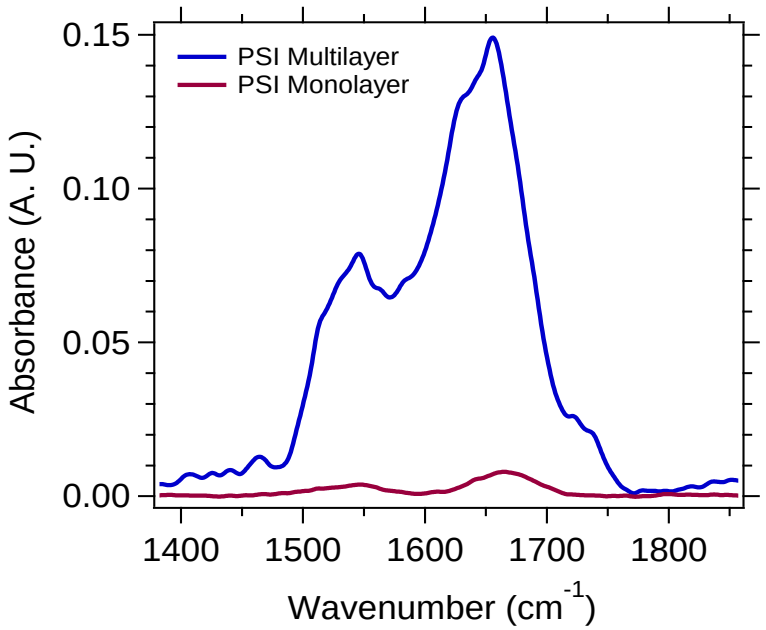

Figure 5.2. Reflectance-Absorption Infrared Spectra of PSI Multilayer and Monolayer Films. PSI multilayer films display dramatically enhanced absorbance with respect to that of a PSI monolayer in the Amide I and II bands of the RAIR spectra.

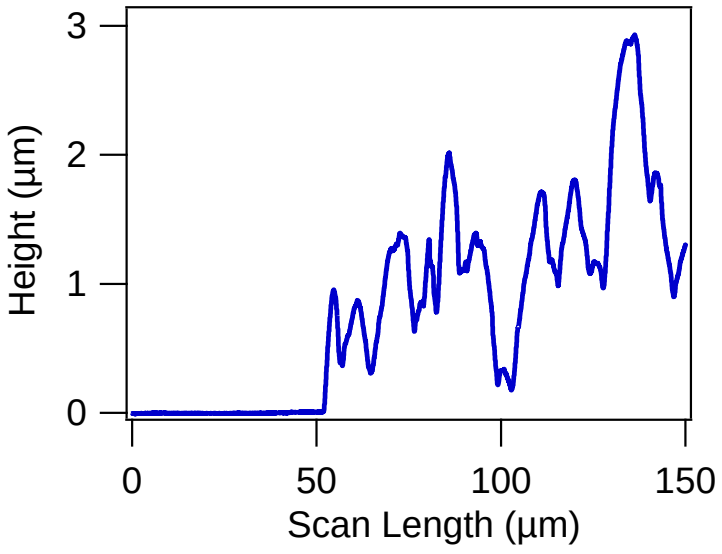

Figure 5.3. Profilometric Line-Scan of a PSI-Multilayer from the Cathode of a Disassembled Cell. The relatively large variation in the film thickness suggests that the spherical particles shown revealed in the AFM imaged are assembled into "hills and valleys" with a lateral size scale of 10-20 µm and heights ranging from 500 nm to 2 µm.

10-200 nm, the relatively large variation in the film thickness shown in Figure 5.3 suggests that these particles are assembled into “hills and valleys” with a lateral size scale of 10-20 μm and heights ranging from 500 nm to 2 μm. These measurements, combined with observation of enhanced absorbance in the Amide I and II bands of the IR spectrum, confirm the presence of a multilayer assembly of PSI complexes on the surface of the cathode of the devices described in this chapter.

We suspect that the spherical particles shown in the AFM image are protein/surfactant agglomerates that form in solution within the reservoir of the cell. In previous studies, PSI monolayers were formed by exposing PSI suspensions to electrode surfaces for 72 hr, after which the samples were rinsed with water to yield PSI monolayers.[6, 8] However, in this present study, PSI multilayer assemblies form within ~ 48 h of injection of the protein suspension and mediator/electrolyte solution into the cell reservoir, and these multilayers remain after rinsing with water when the cell is disassembled. In the context of the previous work, this observation suggests that the driving force for the formation of larger agglomerates arises from the mixture of the two solutions within the reservoir. Upon mixing, the ratio of surfactant to salt is reduced, which decreases the solubility of the protein in the mixture and is a likely cause of the formation of the larger protein/surfactant agglomerates. When these particles become too large to remain in solution they deposit on the cathode surface and pack into a multilayer assembly.

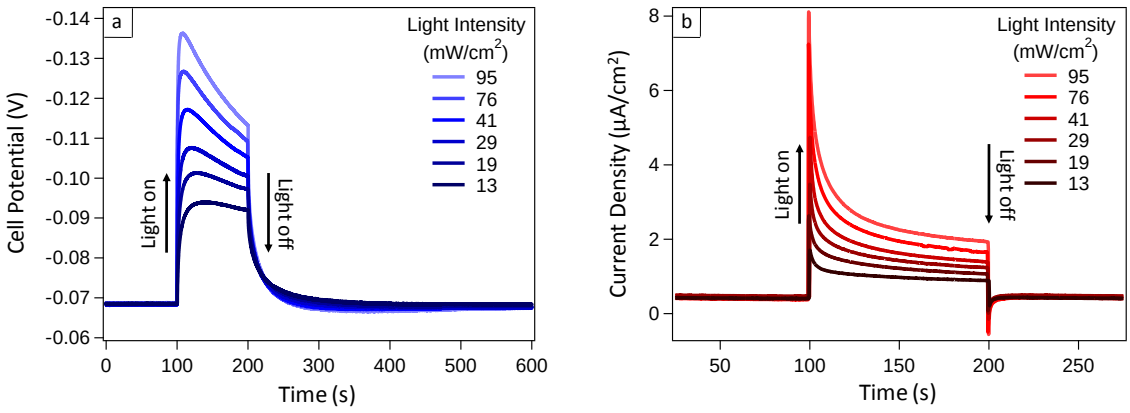

Figure 5.4. Photoresponses of a Typical PSI-Catalyzed Photoelectrochemical Cell at Varying Light Intensities. (a) The open circuit potential of the cell increases when the cell is irradiated due to the change in the concentrations of electrochemical mediators at the electrode surface. **(b)** The photocatalytic effect of the PSI multialyer is observed as an increase in cathodic current when the cell is irradiated. The current decays with time due to the depletion of electrochemical mediators in the vicinity of the electrode surface. The magnitude of the photogenerated increase in both current and voltage is dependent upon the intensity of light irradiating the cell.

Photoelectrochemical Performance

The typical responses of the open circuit potential produced by the cells (i.e. the potential between the Au base electrode and the Cu/ITO counter electrode) to irradiation with light of various intensities are shown in **Figure 5.4a**. During the measurement of the open circuit potential, the potentiostat applies a voltage opposing that supplied by the cell in order to sustain a net current of zero. Thus, the heterogeneous reactions occurring at the electrode surface have a net rate of zero, which allows for the investigation of reactions that occur between mediators and PSI complexes in the multilayer that do not involve charge transfer across the electrode/electrolyte interface but still affect the mediator concentration in the vicinity of the electrode surface. Assuming that the heterogeneous reactions are reversible, single-electron transfer events that occur between the working

electrode and the redox couple, the electrode potential $E(t)$ is related to the concentrations of reduced and oxidized mediators at the electrode surface at time *t* by the Nernstian expression:

$$E(t) = E^{0'} + \frac{RT}{F} \ln \frac{C_O(0,t)}{C_R(0,t)} \quad (1)$$

where $E^{0'}$ is the formal potential of the working electrode at standard conditions, and $C_O(0,t)$ and $C_R(0,t)$ are the respective concentrations of the oxidized and reduced forms of the mediator at any time *t* and position $x = 0$, where the system geometry is defined such that $x = 0$ at the electrode surface and increases in the direction of the surface normal. When the cells are irradiated, charge separation rapidly occurs within PSI complexes in the multilayer which prompts the formation of P_{700}^{+} and F_B^{-} reaction centers as described by Equation 2:

$$P_{700} + F_B \xrightarrow{h\nu} P_{700}^{+} + F_B^{-} \quad (2)$$

The photogeneration of these reaction centers has been shown to produce an electric field at the electrode surface,[9] which may contribute to the steep initial increase in the open circuit potential in response to light as shown in Figure 5.4a. As irradiation persists, redox reactions occur between these P_{700}^{+} and F_B^{-} reaction centers and electrochemical mediators in the vicinity as described by the chemical equations

$$P_{700}^{+} + R \longrightarrow P_{700} + O \quad (3)$$

$$F_B^{-} + O \longrightarrow F_B + R \quad (4)$$

where *O* and *R* represent the oxidized and reduced states of the electrochemical mediators, respectively. The change in the surface concentration of the mediator that results from

these reactions drives the change in the open circuit potential displayed in Figure 5.4a. In the context of equation (1), an increase in the open circuit potential is consistent with the increase in the ratio of $C_O(0,t)$ to $C_R(0,t)$, which indicates that the net effect of PSI-mediator reactions occurring within the multilayer described by equations (3) and (4) is the conversion of *R* to the *O* state. This production of species *O* creates a substantial difference between its concentration near the electrode surface and that in the bulk, and diffusion occurs in response to this concentration gradient. This process is observed as a decrease in the open circuit potential as irradiation continues. When the light is turned off, photogeneration of P_{700}^{+} and F_B^{-} ceases, which quickly halts reactions (3) and (4), and causes the open circuit potential to return to its original value as diffusion from the bulk electrolyte restores $C_O(0,t)$ and $C_R(0,t)$ to their bulk concentrations.

The chronoamperometric behavior of a typical cell is shown in **Figure 5.4b**. In dark conditions, a small cathodic current flows from the gold electrode as electrochemical mediators are reduced at the electrode surface. The observation of this dark current confirms that electrochemical mediators in the oxidized state are initially present at the electrode surface, and further that the PSI multilayer film is permeable to these mediators from the bulk solution. Again assuming that the electrochemical reaction occurring at the electrode surface in dark conditions is a reversible, single-electron transfer event, then the chemical equation describing this reaction can be written simply as $O + e^{-} \longleftrightarrow R$. The net current produced from this reaction at time *t* is the sum of the cathodic and anodic currents, and is given by

$$i_{net}(t) = FA\left[k_{red}C_O(0,t) - k_{ox}C_R(0,t)\right] \qquad (5)$$

where F is the Faraday constant, A is the area of the electrode, and k_{red} and k_{ox} are the heterogeneous rate coefficients for the reduction and oxidation reactions, respectively. When the cell is irradiated, the photocatalytic effect produced by PSI complexes immobilized near the electrode surface produces an increase in cathodic current, which is accompanied by an increased rate of consumption of species O at the electrode surface. This process prompts the formation of a gradient in the concentration of O that propagates away from the electrode surface as time progresses and causes the current to decease as $t^{-1/2}$.[10] Prolonged irradiation results in a buildup of the reduction product R near the electrode surface, which causes an anodic response when the light is turned off as this surplus is oxidized by the electrode.

Similar cathodic photocurrent responses have been observed previously for PSI monolayers on planar[6] and nanoporous[11] electrodes in the same electrochemical mediator system at overpotentials that prompt a cathodic baseline current (i.e. ~0.1V vs Ag/AgCl), and are attributed to the reduction of photoxidized P_{700}^{+} reaction centers that are electronically accessible to the electrode surface.[8] For this reduction to take place, PSI complexes oriented such that their P_{700} reaction centers are electronically accessible to the electrode must be photoexcited to initiate charge separation. The potentiostat measures an increase in cathodic current as P_{700}^{+} centers are reduced by electrons from the electrode surface, and electrons must be continuously shuttled away from the terminal electron acceptor F_B^- by the electrochemical mediators in order for this event to occur repeatedly during extended periods of irradiation. Similarly, at overpotentials that favor oxidation events at the electrode/electrolyte interface, F_B sites proximal to the electrode may

donate photoexcited electrons into the electrode, giving rise to an increase in anodic current in response to irradiation.

The PSI multilayers within the cells described in this work produce cathodic photocurrents that are ~10-20 times larger than those previously reported for PSI monolayers on planar electrodes, which suggests that the multilayer assembly provides photocatalytic mechanisms in addition to the heterogeneous reduction of P_{700}^{+} reaction centers in PSI complexes proximal to the electrode surface. We propose that this enhancement can be primarily attributed to the conversion of reduced electrochemical mediators to the oxidized state by PSI complexes in subsequent layers, which acts to maintain a higher concentration of the oxidized mediator species in the vicinity of the electrode. This re-oxidation of reduced mediators by the P_{700}^{+} reaction centers of PSI complexes in subsequent layers proceeds as described by equation (3) and is shown schematically in **Figure 5.5**. Unlike a monolayer system in which reduced mediators must diffuse to the counter electrode to be re-oxidized, P_{700}^{+} centers in the multilayer assembly provide sites for this to occur in close proximity to the electrode surface, which acts to maintain the concentration of oxidized mediator at the electrode surface and facilitates cathodic currents of greater magnitude. The photoresponse of the open circuit potential implies that $C_O(0,t)$ increases in the absence of net heterogeneous reactions, which supports the assertion that the photocurrent enhancement provided by the present PSI multilayer with respect to that of a monolayer is due to production of oxidized mediators within the multilayer. This proposed mechanism is also consistent with the findings of a study by Proux-Delrouyre and colleagues in which the authors observe a similar photoinduced enhancement of cathodic current produced by PSI complexes dissolved in

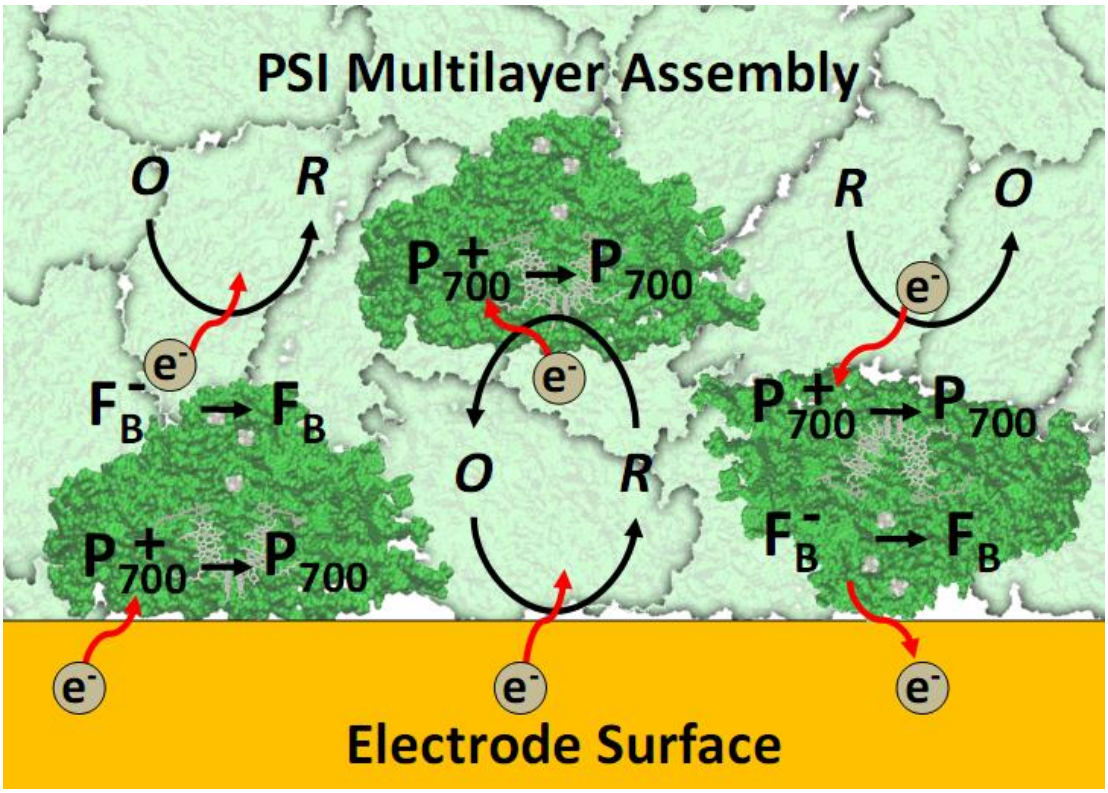

Figure 5.5. Electron Transfer Events between PSI Reaction Centers, Electrochemical Mediators, and the Electrode Surface. Reduced and oxidized mediators may react with PSI's photogenerated P^{+}_{700} and F_B^- reaction centers, respectively, as well as the electrode surface. The reaction centers of PSI may also undergo electron transfer events with the electrode surface directly; however, the observation of a net cathodic current indicates that the dominant reactions occurring at the electrode are the reductions of P^{+}_{700} and oxidized mediators. PSI complexes in subsequent layers contribute to the photoinduced increase in cathodic current by providing sites for the re-oxidation of reduced mediators in close proximity to the electrode, that effectively increases the concentration of oxidized species near the electrode surface and provides more opportunities for heterogeneous reduction events to occur.

the electrolyte and attribute this effect to the regeneration of an oxidized form of an electrochemically mediating protein by PSI. [12]

In order to evaluate of the photoactivity of the electrochemical mediators and supporting electrolyte in the absence of PSI, a cell was fabricated in accordance with the procedure presented earlier in this manuscript; however, instead of injecting the PSI-containing buffer solution, an identical buffer solution that did not contain PSI was

injected. Another cell was similarly fabricated, and a buffer solution that contained only chlorophyll *a* (instead of the chlorophyll-containing PSI complexes) was injected to further highlight the role of the electrochemical functionality of PSI in this photocatalytic system. The total concentration of chlorophyll in the PSI suspension was determined by visible spectroscopy[13] to be 0.78 mM; thus, a concentration of ~0.8 mM was employed so that the control contained roughly the same chlorophyll concentration as the typical PSI-catalyzed cells. **Figure 5.6** presents a comparison of the photocurrent production from these control cells to that of a typical cell in response to irradiation of 29 mW/cm^2. A very small photoresponse was observed from the cell that contained only mediator and electrolyte solution as indicated by a slight change in the current baseline during the periods of illumination. The chlorophyll-containing cell produced a small photocurrent density of < 20 nA/cm^2, which is in excellent agreement with previous results obtained from photoelectrochemical cells consisting of chlorophyll *a* films on metal electrodes.[14] The 50-fold larger photocurrent produced by the PSI-containing cell highlights the benefit of the charge-separation function performed by the electron transfer chain of PSI. Additional studies have reported photocurrents produced by chlorophyll-modified TiO_2 electrodes that are an order of magnitude larger than those produced by the chlorophyll/metal electrodes.[15] In the context of the results of these previous studies and the data presented in Figure 5.6, a similarity is implied between the functions performed by semiconductor materials used by Curri *et al.* and the electron transfer chains of PSI complexes employed in the present system. In both systems, chlorophylls must be coupled to a medium that allows for charge separation to occur in order for significant photocurrents to be generated. In this sense, the multilayer of PSI complexes employed in

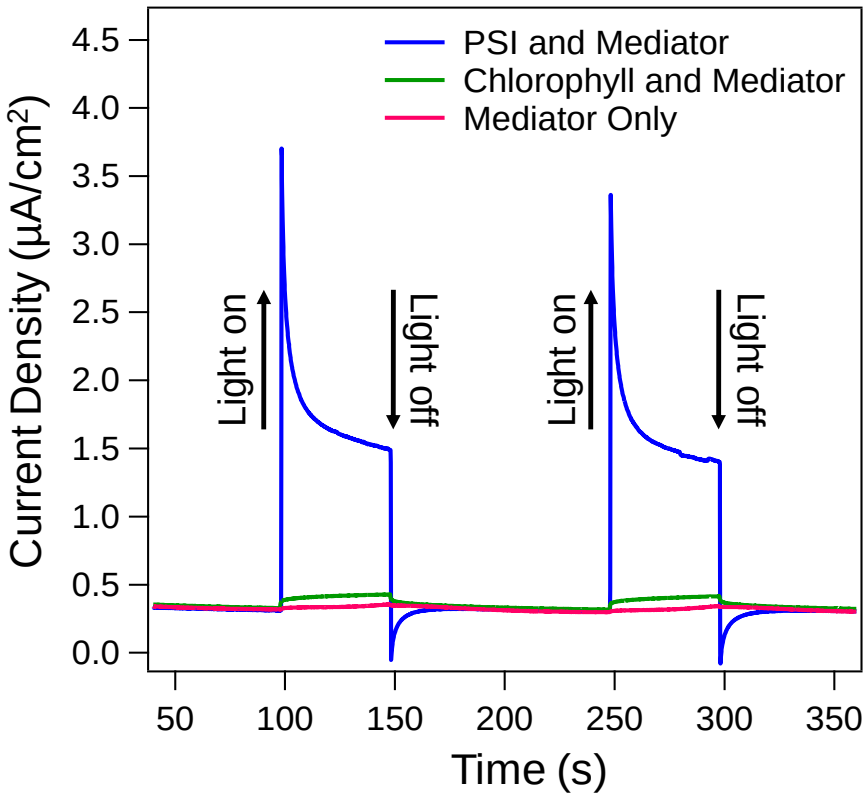

Figure 5.6. Comparison of Photocurrent Response of a Typical PSI-Containing Cell to Experimental Controls. Small dark currents are observed from all cells due to the spontaneous reduction of electron acceptors by the cathode. However, in the absence of PSI and chlorophyll, the electrolyte/mediator solution displays a negligible photoresponse. A cell that contains entire PSI complexes produces ~2 orders of magnitude more photocurrent than one that lacks the protein but contains the same amount of chlorophyll. These responses were generated using a light intensity of 29 mW/cm^2.

the present device could, in some regards, be considered a biological analog to the multilayer of dye-modified semiconductor nanoparticles used in many dye-sensitized solar cells (DSSCs).

Efficiency

The transient nature of the current and voltage production of the cells made the collection of a power curve problematic. However, a rough estimation of the maximum external photoconversion efficiency η_{max} may be estimated from the data presented in Figure 3 simply by multiplying the open circuit potential V_{OC} by the current density J_{SS} (which was collected at zero bias, i.e. short-circuit configuration) and dividing by the intensity P of the light reaching the cell:

$$\eta_{\max}(t) = \frac{J_{SS}(t)\ V_{OC}(t)}{P} \tag{6}$$

These efficiency estimations are plotted in **Figure 5.7** versus the duration of irradiation for each of the six light intensities used. From this analysis we observe that the device efficiency is inversely related to light intensity at irradiations of ~30 s and longer, and furthermore, that the time decay displayed by the current and voltage production of the cells (shown in Figure 3) is clearly represented in the cell efficiency. These observations imply that performance of the current device is limited by the accessibility of electrochemical mediators to PSI complexes adsorbed at the electrode interface, which is dictated by the rate at which these mediators can diffuse through the electrolyte. While the efficiencies of these prototype PSI-catalyzed photoelectrochemical cells are much lower than other photoelectrochemical devices such as semiconductor nanoparticle-based DSSCs, we expect significant improvements will be made through optimization of the device design by reducing the dependence on mediator diffusion. Nevertheless, the photocurrents reported in this study represent an increase of 3 orders of magnitude in less than 3 years based on those we have reported for PSI-modified electrodes.[6, 8, 11]

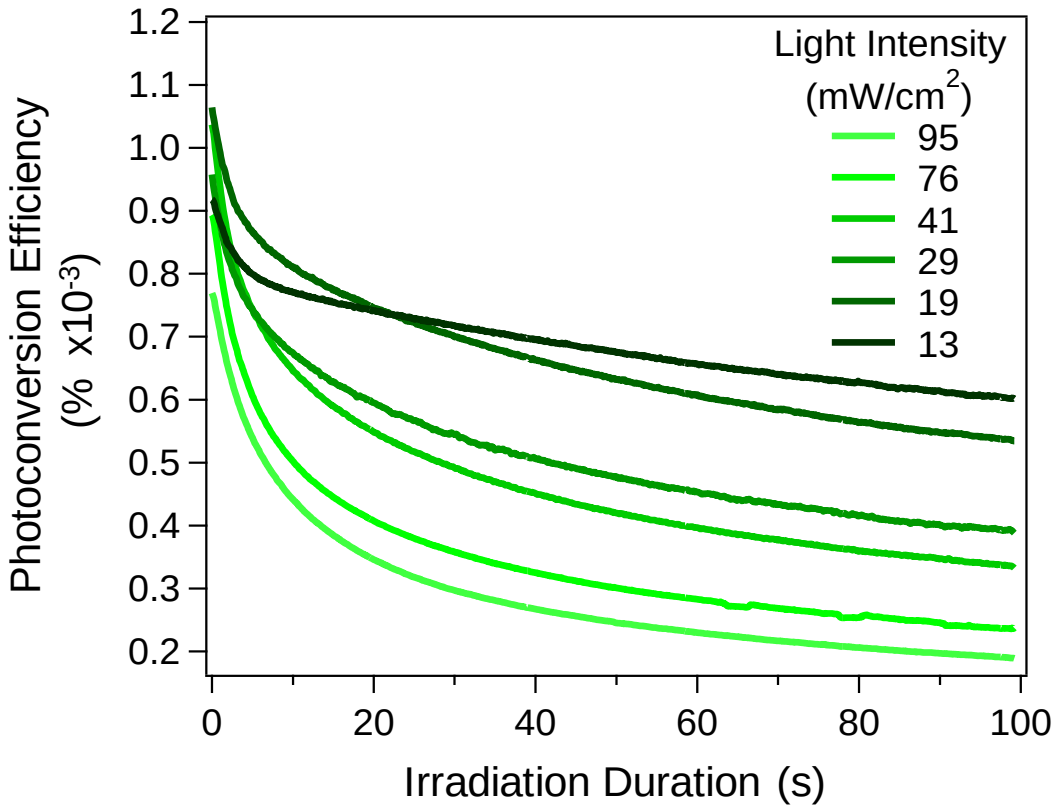

Figure 5.7. External Photoconversion Efficiency. The maximum external photoconversion efficiency can be estimated by taking the product of the photoresponses of the open circuit potential and the short circuit current density. The transient behavior of the current and voltage produced by the cells imply that the efficiency of the device is largely influenced by the diffusion of electrochemical mediators through the cell.

Stability

The stability of these electrochemical cells was evaluated by measuring the photocurrent response produced by the same cell at specific time points over a period of ~280 days, during which the cell was stored in the laboratory at room temperature. The photocurrent response from the cell was measured over a 50 s period of irradiation by white light at an intensity of ~95 mW/cm^2, and the average of this response is plotted against the time it was collected in **Figure 5.8**. The peak photocurrent productivity of the

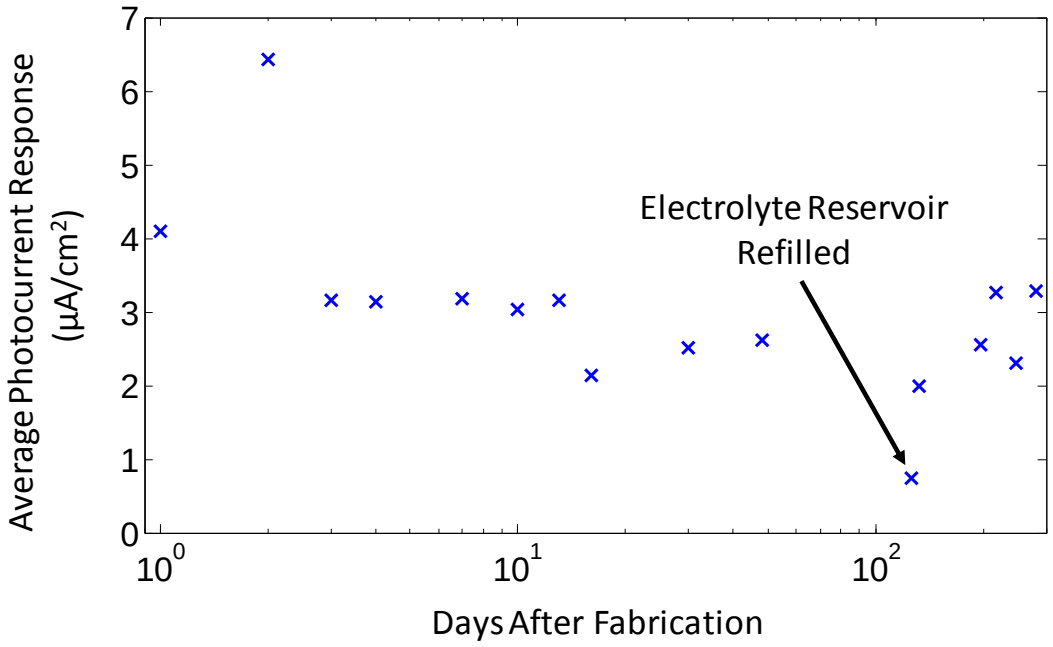

Figure 5.8. Photoelectrochemical Cell Stability. Peak photocurrent production occurs several days after cell fabrication, after which it decreases due to the degradation of PSI complexes that lack adequate stabilizing interactions. An air bubble gradually formed in the electrolyte reservoir of the cell used in this particular study and the reservoir was refilled on day 126, after which the photocurrent production returned to a level similar to that observed 2 weeks after its fabrication. The final data point reported in this plot was collected 281 days after the sample was fabricated.

cells typically occurred 2-4 days after fabrication. During this initial period after the PSI suspension is injected into the cell reservoir, the protein multilayer assembled at the gold surface as PSI complexes in solution found energetically favorable interactions with the hydrophobic and hydrophilic regions of other protein complexes adsorbed on the electrode. Photocurrent production was observed to decrease after the peak was achieved, which we attribute to the degradation of a fraction PSI complexes that were inadequately stabilized; however, a significant portion of PSI complexes remained active for the entire interval over which the stability was monitored as evidenced by the photocurrent production of the

cell months after its fabrication. Throughout the first several months of this study, an air bubble gradually formed within the electrolyte reservoir due to a slightly imperfect seal. On the 126th day after fabrication, fresh electrolyte solution was re-injected into the reservoir, after which the photocurrent production returned to a value similar to that measured two weeks after the cell was constructed. This observation indicates that the number of active PSI complexes in the cell remains relatively constant after the first several weeks up to at least 280 days. While photocurrents were only recorded regularly for the sample whose data are reported in Figure 5.8, all of the cells ($n > 10$) remained photoactive as long as their reservoirs contained electrolyte solution. The electrolyte refilling procedure discussed previously was employed to regenerate several cells in which large air bubbles had formed. These regenerated cells were still photoactive approximately 5 months after fabrication at the last time they were tested.

Conclusions

In summary, we have fabricated biohybrid photoelectrochemical cells in which the functions of light absorption and charge separation are performed by Photosystem I complexes. The cells were constructed by injecting a PSI suspension and a liquid electrolyte that contained electrochemical mediators into a reservoir that is sandwiched between a gold cathode and a Cu-modified ITO anode. After several days, the PSI complexes formed a dense multilayer on the surface of the cathode. Irradiating the cells produced intensity-dependent increases in the voltage and current, and these photoelectrochemical responses exhibited transient behavior that was dominated by diffusion of electrochemical mediators within the cell. We observed that the cells

remained active for over 280 days, during which they were stored in the laboratory at room temperature. The utility of Photosystem I, a biological resource of vast availability, low cost, and robust stability, is demonstrated by the biohybrid device presented in this work.

Works Cited

1. Frolov, L., et al., *Fabrication of oriented multilayers of photosystem I proteins on solid surfaces by auto-metallization.* Advanced Materials, 2008. **20**(2): p. 263-+.

2. Iyanagi, T., I. Yamazaki, and K.F. Anan, *One-Electron Oxidation-Reduction Properties of Ascorbic-Acid.* Biochimica Et Biophysica Acta, 1985. **806**(2): p. 255-261.

3. Izawa, S., *Acceptors And Donors For Chloroplast Electron Transport*, in *Methods in Enzymology*, A. San Pietro, Editor. 1980, Academic Press: New York, NY. p. P413-434.

4. Vassiliev, I.R., et al., *Near-IR absorbance changes and electrogenic reactions in the microsecond-to-second time domain in photosystem I.* Biophysical Journal, 1997. **72**(1): p. 301-315.

5. Lee, J.W., et al., *Chemical Platinization and Its Effect on Excitation Transfer Dynamics and P700 Photooxidation Kinetics in Isolated Photosystem-I.* Biophysical Journal, 1995. **69**(2): p. 652-659.

6. Faulkner, C.J., et al., *Rapid Assembly of Photosystem I Monolayers on Gold Electrodes.* Langmuir, 2008. **24**(16): p. 8409-8412.

7. Kincaid, H.A., et al., *Entrapment of photosystem I within self-assembled films.* Langmuir, 2006. **22**(19): p. 8114-8120.

8. Ciobanu, M., et al., *Electrochemistry and photoelectrochemistry of photosystem I adsorbed on hydroxyl-terminated monolayers.* Journal of Electroanalytical Chemistry, 2007. **599**(1): p. 72-78.

9. Lee, I., et al., *Measurement of electrostatic potentials above oriented single photosynthetic reaction centers.* Journal of Physical Chemistry B, 2000. **104**(11): p. 2439-2443.

10. Bard, A.J. and L.R. Faulkner, *Electrochemical Methods: Fundamentals and Applications*. 2nd ed. 2001, New York: Wiley

11. Ciesielski, P.N., et al., *Functionalized Nanoporous Gold Leaf Electrode Films for the Immobilization of Photosystem I.* Acs Nano, 2008. **2**(12): p. 2465-2472.

12. Proux-Delrouyre, V., et al., *Electrocatalytic investigation of light-induced electron transfer between cytochrome c(6) and photosystem I.* Journal of the American Chemical Society, 2003. **125**(45): p. 13686-13692.

13. Arnon, D.I., *Copper Enzymes In Isolated Chloroplasts. Polyphenoloxidase In Beta Vulgaris* Plant Physiol., 1949. **24**(1): p. 1-15.

14. Karg, V., P. Kis, and G. Nauer, *Photoelectrochemical cells based on polycrystalline chlorophyll α and analogues.* Bioelectrochemistry and Bioenergetics, 1981. **8**(6): p. 691-701.

15. Curri, M.L., et al., *Photochemical sensitisation process at photosynthetic pigments/Q-sized colloidal semiconductor hetero-junctions.* Synthetic Metals, 2003. **139**(3): p. 593-596.

CHAPTER VI

ENHANCED PHOTOCURRENT PRODUCTION BY PHOTOSYSTEM I MULTILAYER ASSEMBLIES

Introduction

Many of the initial studies that investigated the functionality of PSI films assembled onto various substrates focused on monolayers of the protein complex.[1-8] Additional work by our group (discussed in Chapter 3 of this document)[9] and others[10] has shown how photocurrents produced by PSI monolayers in electrochemical systems may be enhanced by decorating nanostructured electrodes with PSI because the increased surface area of the substrates could accommodate more PSI complexes than a planar surface of similar geometric area. Further developments by Frolov *et al.* demonstrated the advantages of multilayer assemblies of PSI by showing that the photovoltage generated by the protein film increased with the number of monolayers that were sequentially deposited;[11] however, preparation of the multilayer required the repetitive deposition of monolayers of genetically mutated PSI complexes and the use of expensive platinum salts. As discussed in Chapter 5, we have developed a photoelectrochemical cell that employs a PSI multilayer to perform the task of light transduction[12] and have shown that the device can produce photocurrents 10-20 times larger than those produced by monolayer systems[3, 4]and 3-4 times larger than the PSI-modified nanoporous electrode system.[9] Formation of the PSI multilayer within the aforementioned photoelectrochemical cell, while thermodynamically spontaneous without the requirement of platinum salts or genetically modified protein, occurred slowly via a

agglomeration/precipitation process that took several days. Furthermore, the process provided poor control over film thickness and was restricted to the closed buffer/electrolyte reservoir within the device.

This chapter presents a fast, general method to assemble multilayer films composed of PSI onto a variety of substrates. The resulting films, akin to the stacked thylakoid structures of leaves, consist of a protein matrix that is permeable to electrochemical mediators and contains a high concentration of photoelectrochemically active redox centers. The deposition procedure, shown schematically in **Figure 6.1,** entails depositing a volume of an aqueous PSI suspension on to a substrate and applying a negative pressure to remove the solvent, leaving a residual PSI-multilayer film on the substrate. The thermodynamic driving force for the formation of these films arises from hydrophobic interactions between neighboring protein complexes in the film. In vivo, the tertiary structure of PSI exhibits a central hydrophobic region that remains within the lipid bilayer of the thylakoid membrane, as well as hydrophilic regions that protrude from either side of the membrane into the aqueous environments of the stroma and lumen of the chloroplast. Prior to the deposition process, the PSI suspension is dialyzed to reduce the concentrations of salt and surfactant in the solution. When this aqueous solvent is removed from the dialyzed PSI solution via the vacuum deposition process, the hydrophobic regions of PSI complexes that were previously stabilized by surfactant now seek stabilizing interactions with the hydrophobic regions of other PSI complexes in the film, which leads to the formation of the dense, resilient film presented in this study. Iterative depositions are similarly performed until the desired film thickness is achieved. While the results presented in this work only contain data obtained from PSI multilayers

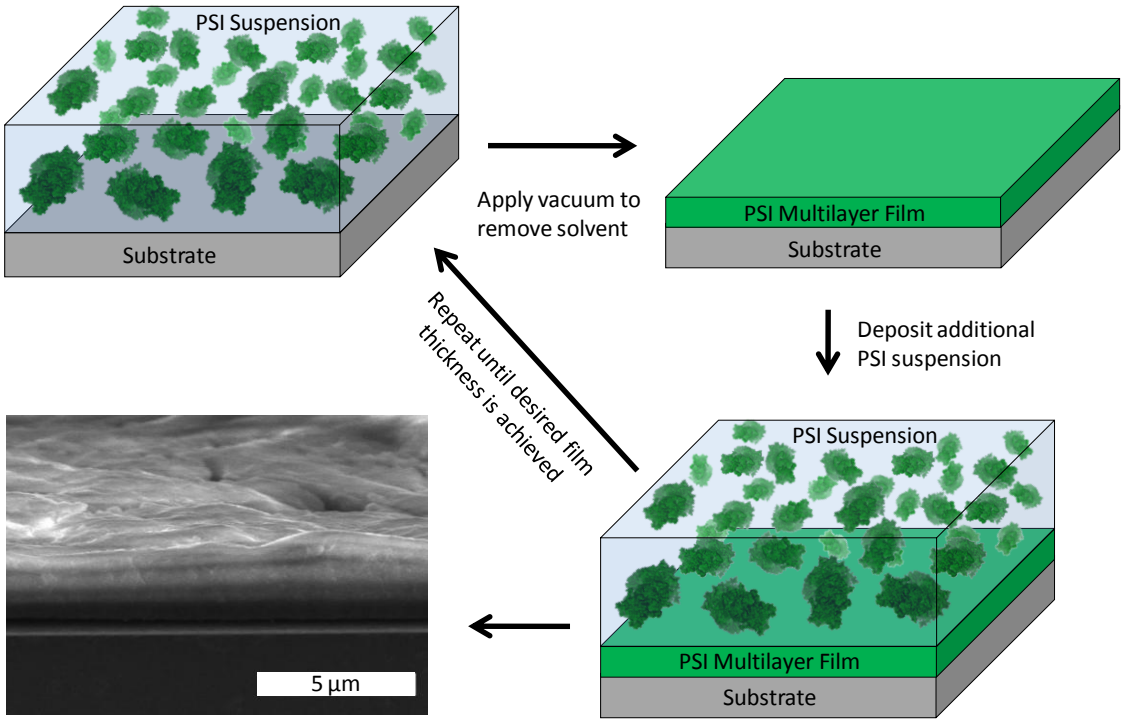

Figure 6.1. PSI Multilayer Preparation by Vacuum-Assisted Assembly. An aqueous suspension of PSI complexes is deposited onto the sample and exposed to a pressure of ~30 mTorr for 10-15 min, yielding a dense film of PSI on the surface. Additional depositions can be "stacked" on the sample using the same technique to produce thicker films. The SEM image in this figure shows the cross section of a film fabricated by 7 deposition steps.

assembled on gold and glass substrates, we have also employed this technique to prepare PSI multilayer films on unmodified surfaces of aluminum foil, indium tin oxide (ITO), silicon (with a native oxide layer), carbon paper, alumina, and polydimethylsiloxane (PDMS).

Film Thickness and Visible Absorbance

The thicknesses of PSI multilayer films produced by various numbers of deposition steps were measured by profilometry. The slope of the line of best fit through these data, shown in **Figure 6.2**, indicates that each deposition step of 75 µl of the PSI suspension, which covered an approximately circular area of 1.8 cm^2 on the substrate, produced an increase in the film thickness by ~390 nm. This value is in excellent agreement with the thickness displayed by the SEM cross-section of a film fabricated by 7 deposition steps (Figure 6.1). Assuming that all of the PSI in the initial volume of solution deposited on the substrate is present in the multilayer film after vacuum deposition, a material balance yields the following expression for film thickness:

$$d = \frac{V_{dep}\left[\mathrm{PSI}\right]_{soln} V_{PSI} N_A}{A_{film}}, \qquad (1)$$

where d is the film thickness, V_{dep} is the initial volume of the PSI solution applied to the substrate, $[PSI]_{soln}$ is the PSI concentration in solution prior to vacuum assembly, N_A is Avogadro's constant, A_{film} is the area covered by the film on the substrate, and V_{PSI} is the volume attributed to single PSI complex in the film, including any residual salt, solvent, and surfactant molecules still associated with the protein after deposition. From (1), we obtain a packing density, V_{PSI}, of 954 nm^3 per PSI complex, which is comparable to

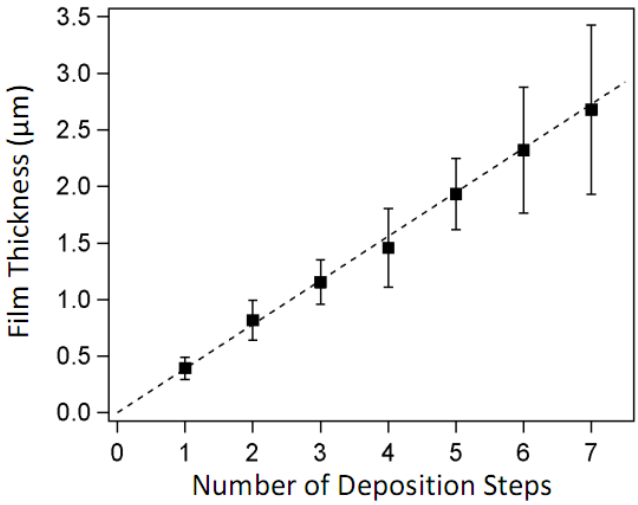

Figure 6.2. Film Thickness. Profilometric measurements indicate that the film thickness increases by ~390 nm with each successive deposition step based on the best fit line through the data points. Points and error bars correspond to the mean and standard deviation, respectively, of the thicknesses obtained from 3 identically prepared samples.

volumes obtained from previous reports of the dimensions of PSI as measured by TEM,[13] AFM,[14] and STM.[15]

The visible absorbance spectra of the multilayered protein films clearly display features typical of PSI complexes as shown in **Figure 6.3**. The absorbance peak located at ~678 nm is characteristic of protein-bound chlorophyll *a*, as opposed to unbound chlorophyll *a* which has an absorption maximum located near 664 nm,[16] which suggests that the majority of these pigments remain bound within the antenna complexes of the photosystems once the multilayer is formed. According to the Beer-Lambert law, absorbance is related to the concentration of the absorbing molecules as well as the optical path length by

$$A = \varepsilon bc, \tag{2}$$

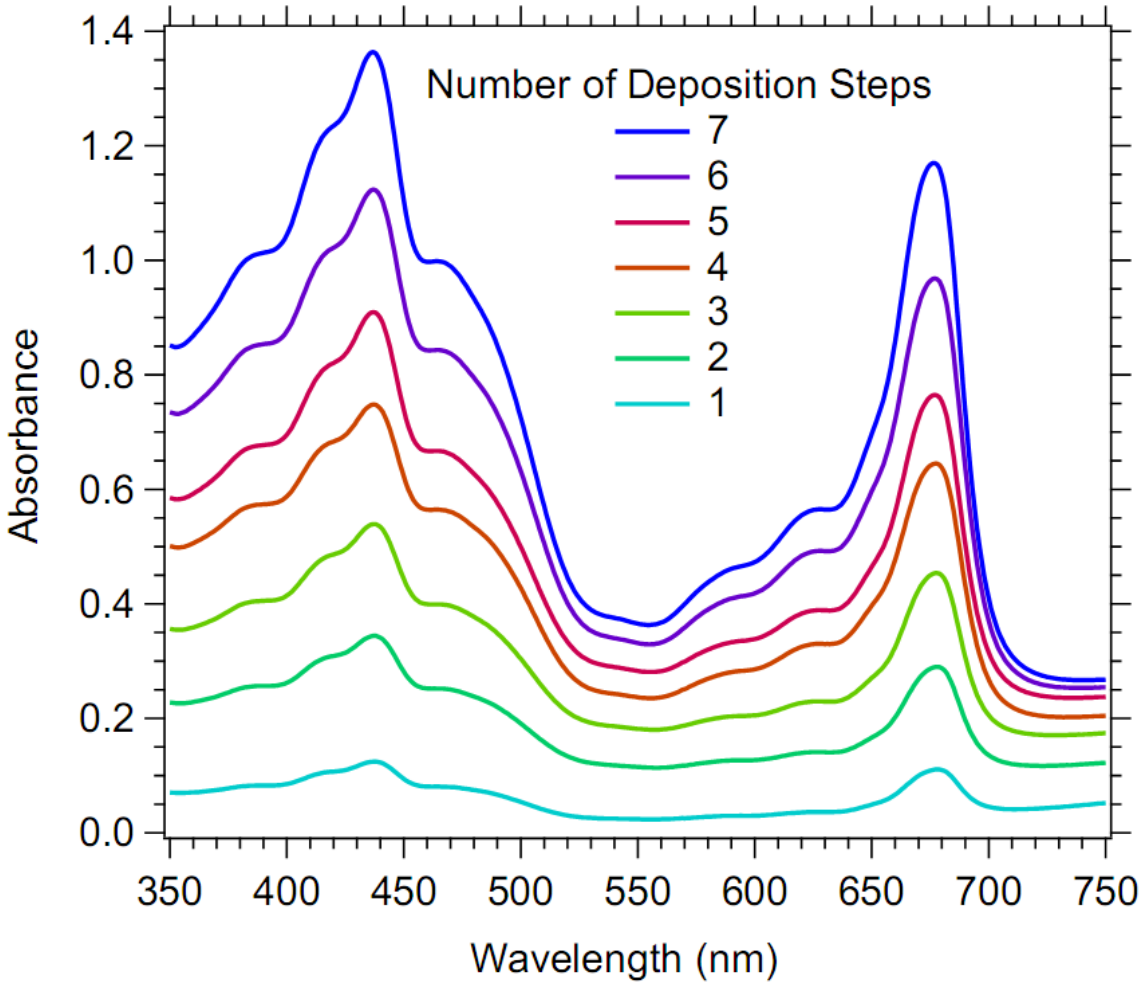

Figure 6.3. Visible Absorbance Spectra of PSI Multilayer Films. The visible absorbance spectra display features typical of PSI complexes. As predicted by the Beer-Lambert law, the magnitude of the absorbance values at peaks that correspond to specific pigments increase linearly with film thickness.

where ε and c are the molar extinction coefficient and concentration of the absorbing pigment, respectively, and b is the optical path length, or film thickness in the case of the present system. Assuming all of the chlorophyll *a* present in the solution is present within the film after the deposition process, the chlorophyll *a* concentration in the multilayer, $[\text{Chl } a]_{film}$, can be estimated as

$$[\text{Chl } a]_{film} = \frac{V_{dep}[\text{Chl } a]_{soln}}{d\ A_{film}}\ , \qquad (3)$$

where $[\text{Chl } a]_{soln}$ is the concentration of chlorophyll *a* in the solution prior to deposition and d is the film thickness. Using the $[\text{Chl } a]_{soln}$ value of 55 μM obtained by the characterization methods of Porra *et al.*,[17] equation (3) yields a value of 60 mol/L for the $[\text{Chl } a]_{film}$. This concentration, along with the thickness data shown in Figure 6.2 and absorbance values at the 678 nm peak shown in Figure 6.3 can be used to calculate a molar extinction coefficient for chlorophyll *a* of 64,000 ± 11,000 $M^{-1}\cdot cm^{-1}$ from equation (2). This value is similar to the previously reported value of 57,000 $M^{-1}\cdot cm^{-1}$ for the molar extinction coefficient of chlorophyll *a* bound within solubilized PSI complexes extracted from *Thermosynechococcus elongatus*.[18]

Photoelectrochemical Characterization

Photochronoamperometric measurements obtained from films fabricated by 1, 3, 5, and 7 deposition steps highlight the effect of increasing film thickness on the photocurrent production of the films as shown in **Figure 6.4a**. During these experiments, a constant overpotential of +0.1 V (~0.3 V vs Ag/AgCl) was applied to the working electrode upon which the PSI film was assembled, and the current density flowing through the electrode was recorded in light and dark conditions. In dark conditions at this

positive overpotential, an anodic baseline current (reported as negative by convention) flows due to the heterogeneous oxidation of $[Fe(CN)_6]^{4-}$. The observation of this baseline current in dark conditions confirms that the multilayer film is permeable to the electrolyte solution and the redox couple. When the electrode is irradiated, charge separation occurs within PSI complexes in the multilayer, producing P_{700}^{+} and F_B^{-} reaction centers throughout the film according to

$$P_{700} + F_B \xrightarrow{h\nu} P_{700}^{+} + F_B^{-} \quad . \tag{4}$$

Direct electron transfer between the electrode and the reaction centers of surface-bound PSI complexes has been previously demonstrated by us[3, 4, 9] and others;[8, 10, 19] however the photocurrents produced by the present system are orders of magnitude larger than those produced by the aforementioned monolayer systems due to the photocatalytic effect afforded by the multilayer assembly. Photogenerated reaction centers of PSI complexes within the multilayer react with the redox couple as

$$F_B^{-} + \left[\mathrm{Fe(CN)_6}\right]^{3-} \longrightarrow F_B + \left[\mathrm{Fe(CN)_6}\right]^{4-} \tag{5}$$

and

$$P_{700}^{+} + \left[\mathrm{Fe(CN)_6}\right]^{4-} \longrightarrow P_{700} + \left[\mathrm{Fe(CN)_6}\right]^{3-} \quad . \tag{6}$$

These photoinduced redox reactions are shown schematically in the zoom window of **Figure 6.5**. The diffusional transport of the products of these reactions through the film is governed by processes similar to those that occur in dye-sensitized solar cells (DSSC),[20] in that the net flux of charge across the electrode interface prompts the

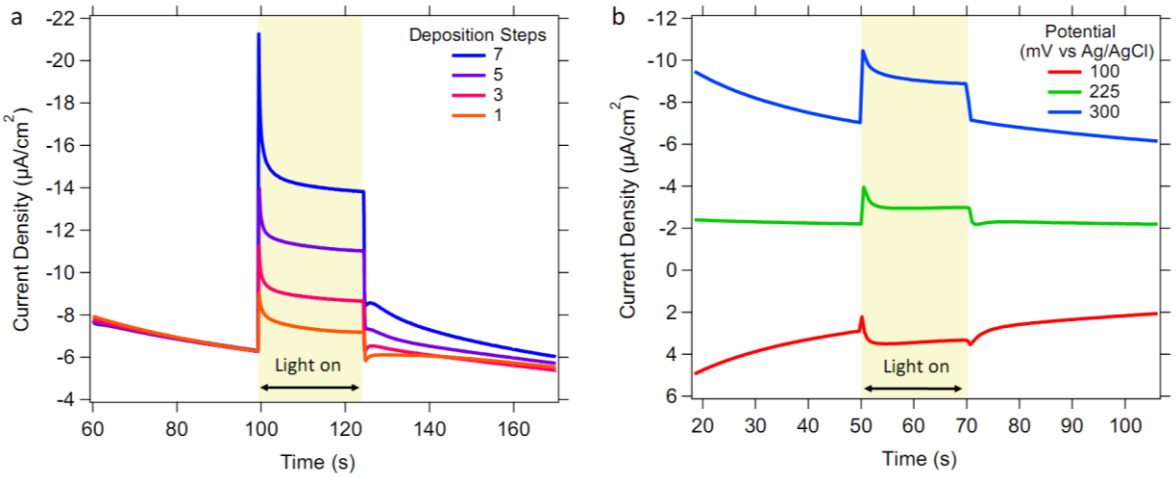

Figure 6.4. Photochronoamperometric Response of PSI Multilayer Films. (a) In dark conditions, an anodic baseline current is observed in response to the +0.1 V overpotential at which the data were collected. In response to irradiation, charge separation occurs within PSI complexes in the multilayer assembly, and these charges can then be transported through the film by the redox couple to produce a photocurrent. Thicker films produce larger photocurrents because they provide more sites at which charge separation may occur. **(b)** Photoinduced increases in current are observed at both anodic and cathodic overpotentials; however, the magnitude of the current increase is considerably larger in the anodic direction. We assert that the large thermodynamic driving force for the reduction of $[Fe(CN)_6]^{3-}$ by F_B^- relative to that for the oxidation of $[Fe(CN)_6]^{4-}$ by P_{700}^+ gives rise to the discrepancy between the magnitudes of the photocurrents at anodic and cathodic overpotentials.

formation of gradients in the electrochemical potential of the charge carriers within the system, and these gradients direct the diffusive transport of electrochemical mediators within the film. In the case of the chronoamperometric experiments shown in Figure 6.4a, the positive overpotential prompts the net transfer of negative charge into the electrode from the reduced form of the redox couple, $[Fe(CN)_6]^{4-}$, which forms a gradient in the concentration of this species that prompts its diffusion toward the electrode surface. Similarly, this consumption of the reduced form of the redox couple at the electrode

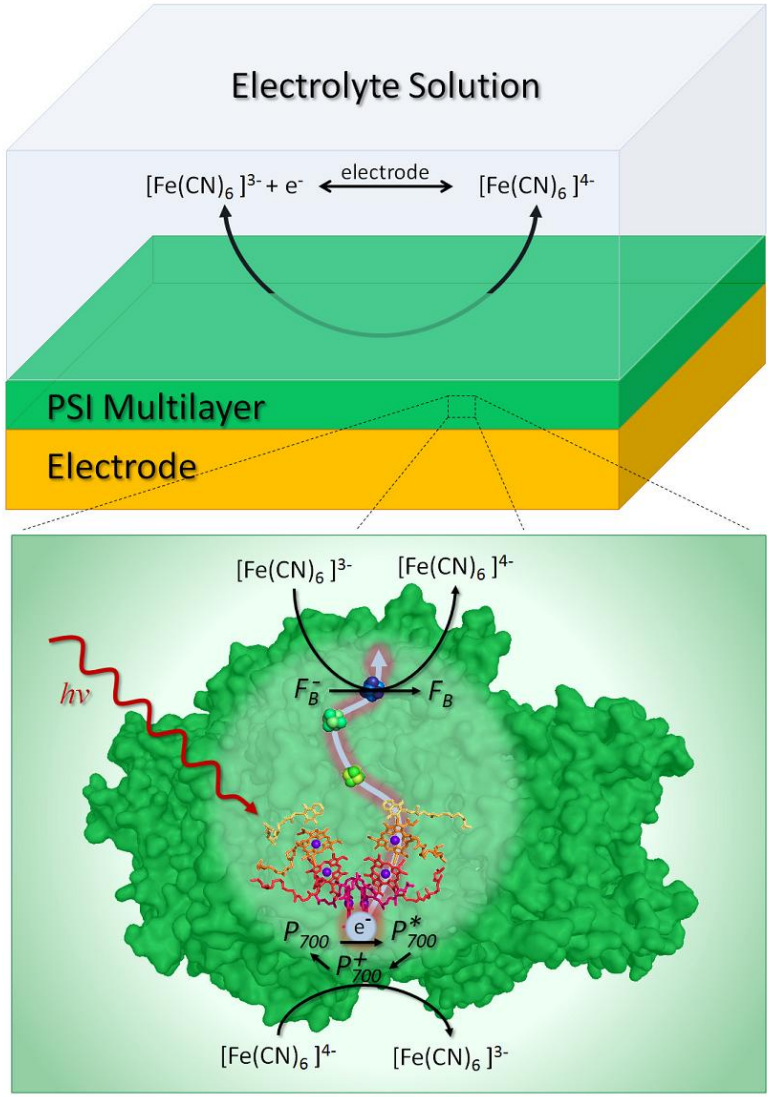

Figure 6.5. Electrochemical Reactions Occurring at the Surface of an Electrode Modified by a PSI Multilayer Film. The protein film is permeable to the electrolyte and redox couple, which allows the redox couple to react reversibly at the electrode surface as dictated by the overpotential applied to the electrode (i.e. negative overpotentials favor the reduction of $[Fe(CN)_6]^{3-}$, while positive overpotentials favor the oxidation of $[Fe(CN)_6]^{4-}$). The net transfer of charge at the electrode surface prompts the diffusional transport of charge carriers throughout the film. **Zoom Window: Photoinduced Redox Reactions Occurring within the PSI Multilayer.** Energy from incident photons is collected by chlorophylls within the antenna complexes of PSI and transferred to the P_{700} reaction center, exciting it to a state denoted as P_{700}*. The excited reaction center releases an electron down the electron transfer chain, oxidizing the P_{700} reaction center to an electron deficient state denoted as P_{700}^{+}. The terminal acceptor of the electron transfer chain is an iron-sulfur complex, denoted as F_B, that is reduced to F_B^{-} when the electron arrives. Electrons are resupplied to P_{700}^{+} by the reduced form of the redox couple, $[Fe(CN)_6]^{4-}$, and electrons are removed from F_B^{-} by the oxidized form, $[Fe(CN)_6]^{3-}$.

surface results in the production of the oxidized form, $[Fe(CN)_6]^{3-}$, in the same location, which forms a gradient concentration of this species that directs its diffusive flux away from the electrode and into the bulk electrolyte. The increased flux of negative charge carriers to the electrode surface that results from reactions (4), (5) and (6) is observed as increase in anodic current in response to irradiation. Films fabricated by 1, 3, 5, and 7 deposition steps produced approximate photocurrent densities 1.2, 2.7, 5.2, and 7.9, $\mu A \cdot cm^{-2}$, respectively. While photocurrent responses to short periods of irradiation are presented in Figure 4 to highlight the difference between the current in light and dark conditions, we have observed stable photocurrents for irradiation periods of > 10 min that decrease only according to the depletion of electrochemical mediators in the electrolyte and do not display a decay in the photocatalytic activity of the film.

In order to further elucidate the photocurrent production by the PSI multilayer assembly, photochronoamperometric experiments were performed at several additional overpotentials. In contrast to the experiments shown in Figure 6.4a, the application of a -0.1 V overpotential (~ +0.1 V vs Ag/AgCl) to the working electrode favors the reduction of $[Fe(CN)_6]^{3-}$, at the electrode surface, which prompts a cathodic current to flow through the electrode as shown in the bottom curve of Figure 6.4b. At this overpotential, the net transfer of electrons from the electrode to the oxidized form of the redox couple forms a concentration gradient that directs the oxidation product of reaction (6) towards the surface and the reduction product of reaction (5) away from the surface, thus an increase in cathodic current is measured in response to irradiation. At small overpotentials, both forms of the redox couple may react at the electrode and the magnitude of the photocurrent response contains contributions from both reactions (5)

and (6). The photocurrent responses shown in Figure 6.4b reveal that the present system favors anodic photocurrent production over cathodic. Since the photocatalytic effect arises from the production of the heterogeneous reactants by PSI complexes within the film, we attribute this result to the disparity of energetic favorability between reactions (5) and (6). The formal potentials of the F_B / F_B^-, P_{700}^+ / P_{700}, and $[Fe(CN)_6]^{3-}$ / $[Fe(CN)_6]^{4-}$ redox couples are approximately -0.585,[21] +0.490,[22] and +0.36[23] V vs NHE, respectively. The difference of the formal potentials of the reactants for reduction of $Fe(CN)_6^{3-}$ by F_B^- is ~0.95 V, while that for the reduction of P_{700}^+ by $[Fe(CN)_6]^{4-}$ is only ~0.13 V. We assert that this large thermodynamic driving force for reaction (5) relative to that for reaction (6) is primarily responsible for the production of larger photocurrents in the anodic direction than in the cathodic direction.

A more comprehensive view of the photocatalytic effect of PSI multilayer films in the presence of the $[Fe(CN)_6]^{3-}$ / $[Fe(CN)_6]^{4-}$ redox couple was obtained by performing cyclic voltammetry at various scan rates in light and dark conditions using a working electrode that was modified with a PSI multilayer of three deposition steps (**Figure 6.6**). During these experiments, heterogeneous oxidation and reduction of the redox couple occurs during the anodic and cathodic sweeps, respectively, as described by

$$\left[Fe(CN)_6\right]^{3-} + e^- \xleftrightarrow{electrode} \left[Fe(CN)_6\right]^{4-} \qquad (7)$$

When the electrode is irradiated, currents of larger magnitude are observed during both anodic and cathodic sweep segments; however, the photocurrents produced during the anodic sweeps are considerably larger than those observed during the cathodic sweep, which is consistent with the chronoamperometric experiments presented earlier in this

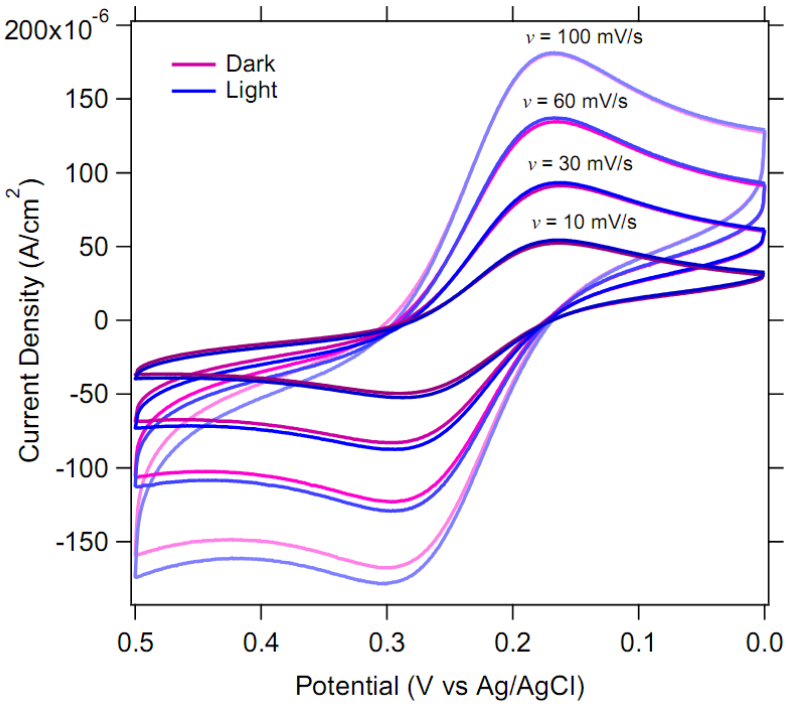

Figure 6.6. Cyclic Voltammograms of an Electrode Modified by a PSI multilayer Film in Light and Dark Conditions. Photoinduced increases in current are observed during both anodic and cathodic voltage sweeps; however, the magnitude of the current increase is considerably larger during the anodic sweep, which is consistent with photochronoamperometric measurements obtained from this system.

chapter. A plot of peak current density measured during the anodic sweep versus the square root of the scan rate, *v*, is presented in **Figure 6.7**. In both light and dark conditions, the peak current density varies approximately linearly with $v^{1/2}$, which is typical of the reversible, single-electron transfer behavior exhibited by the $[Fe(CN)_6]^{3-}$ / $[Fe(CN)_6]^{4-}$ redox couple observed in electrochemical systems. For a totally reversible heterogeneous electrochemical reaction, the peak current measured during a potential sweep, i_P, is related to the scan rate by the expression

$$i_P = \left(2.69\times10^5\right) n^{3/2} A D^{1/2} C^* v^{1/2} \qquad (8)$$

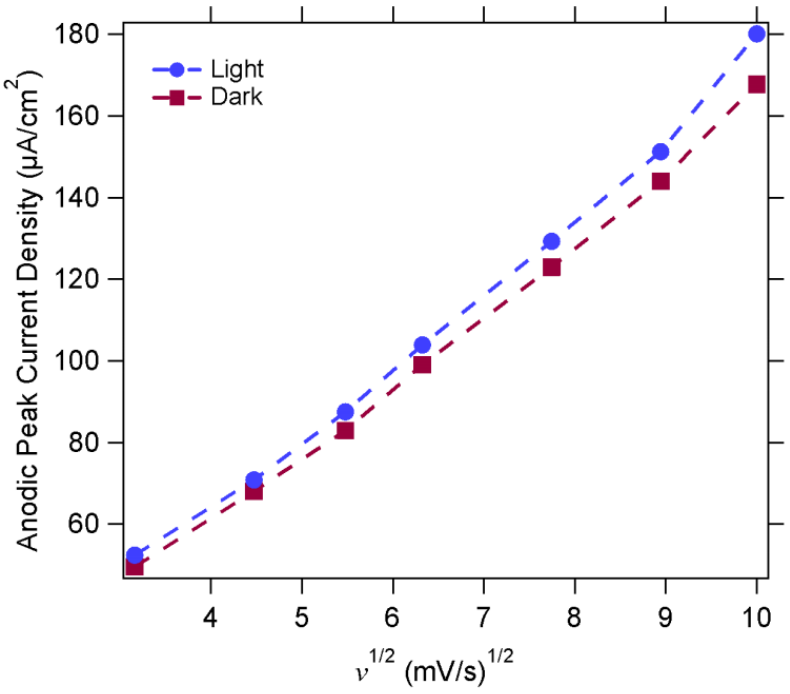

Figure 6.7. Scan Rate Dependence of the Anodic Sweep Peak Current. In both light and dark conditions, the peak current increases approximately linearly with $v^{1/2}$. A larger slope is observed during light conditions due to the photocatalytic effect of the PSI multilayer film.

where n is the number of electrons transferred in the reaction, A is the surface area of the electrode, and D and C^* are the diffusion coefficient and bulk concentration of the heterogeneous reactant, respectively.[24] Parameters extracted from a linear fit of the data shown in Figure 6.7 indicate that the slope of the line through the peak currents measured in light conditions is ~ 7% larger than the slope of the line through the dark currents. In light of equation (8), this observation may be interpreted as an effective increase the diffusion coefficient redox couple, or as an effective increase in its bulk concentration. The former interpretation suggests that the photocatalytic effect of the PSI multilayer film is due to increased transport of the heterogeneous reactant to the electrode

surface. Such an effect could arise from a decrease in the barrier properties of the film in response to irradiation. Additional information about this effect could be obtained by performing careful electrochemical impedance measurements on PSI multilayer films in light and dark conditions. Perhaps a more probable explanation is offered by the latter interpretation of equation (8): since the bulk concentration of the redox couple is clearly not changed significantly during these experiments, an effective change in the bulk concentration in (8) could arise from an increased concentration of the heterogeneous reactant within the PSI film during periods of irradiation. Further insight into this assertion could be provided by SECM, in which the mediator concentrations could be investigated very close to the electrode surface during light and dark conditions. While fundamentally different, both of these interpretations are encompassed by the effect to which photocurrent production is attributed earlier in this chapter, i.e. the increased diffusive flux of charge carriers at the electrode surface in response to irradiation, and additional experiments will help identify the contributions of each mechanism to the photocurrent production.

Photocurrent Action Spectrum

Normalized photocurrent responses of PSI multilayer films to irradiation by monochromatic light of various wavelengths are plotted with a normalized absorbance spectrum in **Figure 6.8**. Maxima in the photocurrent action spectrum appear at wavelengths that correspond to the Soret band in the blue region (~ 440 nm) and the Q_y transition band (~ 680 nm) of chlorophyll *a* in the red region, the latter of which is primarily attributed to the first electronic transition of bulk chlorophyll *a* in the core

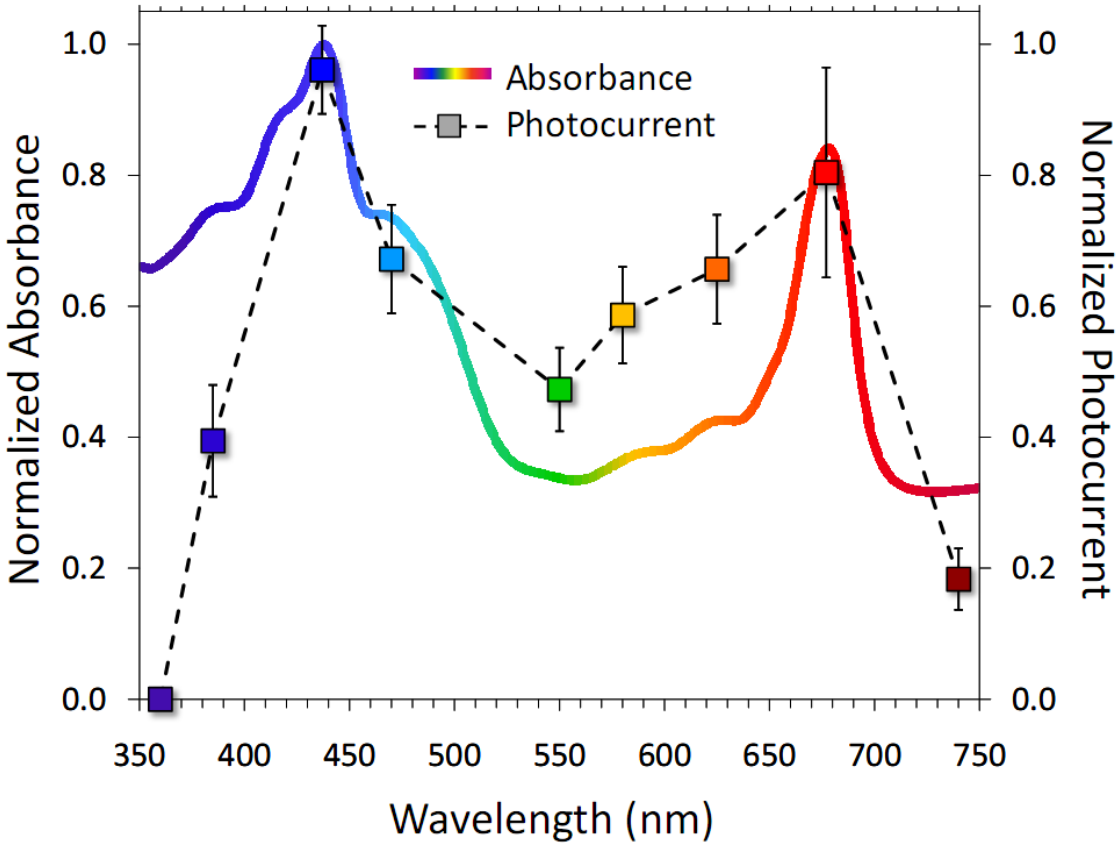

Figure 6.8. Photocurrent Action Spectrum. Trends in the photocurrents produced by electrodes modified with PSI multilayer assemblies in response to irradiation by light of various wavelengths follow the absorbance spectrum of the protein film, confirming that the photocatalytic effect originates from the activity of PSI complexes. The absorbance spectrum in this figure was collected from a PSI multilayer of 3 deposition steps and was normalized to its maximum. Data points and error bars represent the means and standard deviations, respectively, of the photocurrent responses to the various wavelengths produced by 4 identically prepared PSI multilayer films fabricated by 3 deposition steps.

antenna system of PSI.[25] While wavelengths in the UV-A region are strongly absorbed by the films, irradiation by these wavelengths did not produce proportionately large photocurrents, with virtually no photocurrent produced by 360 nm light. Absorption of these high energy photons is more likely to photo-bleach chlorophyll molecules rather than initiate electronic transitions that feed excitation energy to the electron transfer chain of PSI.[26] From these data, the internal quantum efficiency, QE_λ, was estimated by

$$QE_\lambda = \frac{\text{photocurrent electrons}}{\text{photons absorbed by film}} = \frac{j_\lambda N_A / F}{\theta_\lambda \langle P \rangle / E_\lambda} \tag{7}$$

where j_λ is the photocurrent density produced by irradiation of the sample by monochromatic light of wavelength λ, N_A is Avogadro's constant, F is Faraday's constant, $\langle P \rangle$ is the average intensity of the laser irradiating the sample (obtained by multiplying the pulse energy by the repetition rate), E_λ is the energy of a single photon of wavelength λ, and θ_λ is the fraction of photons of wavelength λ absorbed by the film and can be calculated from the absorbance spectrum by

$$\theta_\lambda = 1 - 10^{-A_\lambda} \tag{8}$$

where A_λ is the absorbance of the film at wavelength λ. From equation (7), we calculated the internal quantum efficiency for the films fabricated by 3 deposition steps to be 0.014% and 0.017% at wavelengths of 437 nm and 678 nm, respectively. In addition to providing further confirmation that the photocurrent produced by these films originates from the photocatalytic behavior of PSI, these results identify potential utility for this biomaterial in low-cost light-transduction devices capable of differentiating incident photons from certain regions of the visible spectrum based on their wavelength.

Conclusions

In summary, we have presented a method to fabricate multilayer films of Photosystem I complexes by vacuum-assisted assembly. The technique is applicable to a variety of substrates and allows control over film thickness by varying the number of deposition steps. The protein films characterized in this work produced a photocurrent when incorporated into an electrochemical system, and we have shown that the photoconversion capabilities of the films increased with their thickness. Furthermore, the photocurrent action spectrum of the films reveals that the photocurrent production, in fact, originates from the photocatalytic activity of the PSI complexes of which the films are comprised. These results represent rapid and substantial progress in terms of photocurrent production by PSI films, as the photocurrent magnitudes reported here are nearly 5 times greater than those produced by the PSI-based photoelectrochemical cell we reported recently[12] and approximately 1,800 times greater than the first photocurrents from PSI-modified electrodes fabricated by our group in 2007.[3] The multilayer films described in this work provide a fast, simple, and inexpensive means to access the useful functionality of Photosystem I, a renewable natural resource of vast abundance.

Experimental

Photosystem I Extraction

PSI-40 complexes were extracted and characterized as described in Chapter 4, and the total chlorophyll concentration of the product was determined by the method of Porra *et. al.*[17] to be 7.1×10^{-5} M with a Chl *a* / Chl *b* ratio of 3.3, and the P_{700}

concentration was determined using the method of Baba *et. al.*[27] to be 1.6 x 10^{-6} M, yielding a Chl/P_{700} ratio of 43.

Scanning Electron Microscopy

SEM images were taken with a Hitachi S-4200 Scanning Electron Microscope using an accelerating voltage of 10 kV.

Visible Absorbance Spectroscopy

Visible absorbance spectra were collected with a Varian Cary 5000 UV-VIS-NIR spectrophotometer operating in transmission mode from PSI multilayer films assembled on glass slides, using a clean glass slide as a background.

Profilometry

Film thicknesses were measured with a Veeco DEKTAK 150 Surface Profiler using a stylus force of 6.5 mg at a scan rate of 2.5 $\mu m \cdot s^{-1}$. Line-scans were collected starting near the edge of the multilayer and proceeding into the film and the average thickness of the film was recorded. This procedure was repeated for at least 3 identically prepared samples for each number of deposition steps, and the mean average of the film thickness is reported in Figure 2 with the standard deviation as error bars.

Vacuum-assisted PSI multilayer assembly

PSI multilayers were prepared on as-received glass microscope slides (Fisher) that were washed with deionized water and ethanol and dried with nitrogen for

characterization by visible absorbance spectroscopy and profilometry. For the purposes of characterization by analytical electrochemistry and scanning electron microscopy, PSI films were prepared on a ~125 nm thick gold layer (J&J Materials) which was thermally deposited onto a silicon support (Montico Silicon, <100> orientation) and modified with a self-assembled monolayer of aminoethanethiol (ACROS) to provide a hydrophilic surface to facilitate spreading of the PSI suspension. For both substrates, vacuum assisted assembly was carried out identically: a volume of 50-75 μl of the PSI suspension was pipetted on to the substrate. Volumes of this size were employed in order to produce films that covered an approximately circular area of the substrate with a diameter of ~1.5 cm. The substrate was then placed in a vacuum chamber and a pressure of ~30 mTorr was applied until the liquid had evaporated (typically 10-15 min). Additional depositions were similarly performed repetitively atop the previous film until the desired film thickness was achieved. In contrast to our previously reported vacuum assembly technique in which the resulting film was rinsed with water to yield a dense monolayer,[4] the vacuum assembled multilayer films fabricated in this work from PSI suspension that had been purified by dialysis were not water soluble and remained on the substrates even after thorough rinsing with water. We attribute this change in solubility to the reduction of the salt and surfactant concentrations in the suspension by the dialysis procedure.

Analytical photoelectrochemistry

All electrochemical measurements were obtained using a CH Instruments CHI660a electrochemical workstation equipped with a Faraday cage. A custom-built,

three electrode cell was used with the PSI-modified gold substrate as the working electrode, platinum mesh as the counter electrode, and Ag/AgCl as the reference electrode, using an aqueous electrolyte solution of 100 μM $K_3Fe(CN)_6$ (Aldrich), 100 μM $K_4Fe(CN)_6$ (Aldrich), and 0.1 M KCl (Fisher) in 5 mM pH 7 phosphate buffer (Fisher). The working electrode had an exposed surface area 0.126 cm^2. Photochronoamperometric data were collected at an overpotential of +0.1 V (approximately +300 mV vs Ag/AgCl). The photoresponses reported in Figure 6.4 were generated by illuminating the sample with a Gebrauch KL 2500 LCD lamp at an approximate intensity of 95 mW/cm^2. Photoresponses reported in the action spectrum in Figure 6.8 were obtained by illumination of the sample with the pulsed radiation of a wavelength-tunable Quantronix TITAN/TOPAS optical parametric amplifier system. This laser produces 150-fs pulses at a rate of 1 kHz and is tunable across the UV, visible, and near-IR spectral regions. A prism and aperture were used to select the desired wavelength from the beam output and to maintain a consistent spot size diameter of ~3 mm. The beam output was then attenuated by means of a variable neutral density filter to obtain average pulse energies of 3 μJ at all wavelengths, and was directed onto the sample without focusing. Pulse energies were measured using a Coherent J-10MB-LE detector and LabMax Top energy meter. Photocurrent responses were normalized with respect to optical quanta per pulse.

Works Cited

1. Carmeli, I., et al., *Photovoltaic activity of photosystem I-based self-assembled monolayer.* Journal of the American Chemical Society, 2007. **129**(41): p. 12352-+.

2. Ciobanu, M., et al., *Photosystem I Patterning Imaged by Scanning Electrochemical Microscopy.* Langmuir, 2005. **21**: p. 692-698.

3. Ciobanu, M., et al., *Electrochemistry and photoelectrochemistry of photosystem I adsorbed on hydroxyl-terminated monolayers.* Journal of Electroanalytical Chemistry, 2007. **599**(1): p. 72-78.

4. Faulkner, C.J., et al., *Rapid Assembly of Photosystem I Monolayers on Gold Electrodes.* Langmuir, 2008. **24**(16): p. 8409-8412.

5. Frolov, L., et al., *Fabrication of a photoelectronic device by direct chemical binding of the photosynthetic reaction center protein to metal surfaces.* Advanced Materials, 2005. **17**(20): p. 2434-+.

6. Kincaid, H.A., et al., *Entrapment of photosystem I within self-assembled films.* Langmuir, 2006. **22**(19): p. 8114-8120.

7. Lee, I., J.W. Lee, and E. Greenbaum, *Biomolecular electronics: Vectorial arrays of photosynthetic reaction centers.* Physical Review Letters, 1997. **79**(17): p. 3294-3297.

8. Terasaki, N., et al., *Bio-photo sensor: Cyanobacterial photosystem I coupled with transistor via molecular wire.* Biochimica Et Biophysica Acta-Bioenergetics, 2007. **1767**(6): p. 653-659.

9. Ciesielski, P.N., et al., *Functionalized Nanoporous Gold Leaf Electrode Films for the Immobilization of Photosystem I.* Acs Nano, 2008. **2**(12): p. 2465-2472.

10. Terasaki, N., et al., *Fabrication of novel photosystem I-gold nanoparticle hybrids and their photocurrent enhancement.* Thin Solid Films, 2006. **499**(1-2): p. 153-156.

11. Frolov, L., et al., *Fabrication of oriented multilayers of photosystem I proteins on solid surfaces by auto-metallization.* Advanced Materials, 2008. **20**(2): p. 263-+.

12. Ciesielski, P.N., et al., *Photosystem I - Based biohybrid photoelectrochemical cells.* Bioresource Technology 2010. **101**(9): p. 3047-3053.

13. Boekema, E.J., R.M. Wynn, and R. Malkin, *The Structure of Spinach Photosystem-I Studied by Electron-Microscopy.* Biochimica Et Biophysica Acta, 1990. **1017**(1): p. 49-56.

14. Fotiadis, D., et al., *Surface analysis of the photosystem I complex by electron and atomic force microscopy.* Journal of Molecular Biology, 1998. **283**(1): p. 83-94.

15. Lee, J.W., et al., *Chemical Platinization and Its Effect on Excitation Transfer Dynamics and P700 Photooxidation Kinetics in Isolated Photosystem-I.* Biophysical Journal, 1995. **69**(2): p. 652-659.

16. Byrdin, M., et al., *Light harvesting in photosystem I: Modeling based on the 2.5-angstrom structure of photosystem I from Synechococcus elongatus.* Biophysical Journal, 2002. **83**(1): p. 433-457.

17. Porra, R.J., *The chequered history of the development and use of simultaneous equations for the accurate determination of chlorophylls a and b.* Photosynthesis Research, 2002. **73**(1-3): p. 149-156.

18. Müh, F. and A. Zouni, *Extinction coefficients and critical solubilisation concentrations of photosystems I and II from Thermosynechococcus elongatus.* Biochimica et Biophysica Acta (BBA) - Bioenergetics, 2005. **1708**(2): p. 219-228.

19. Terasaki, N., et al., *Plugging a Molecular Wire into Photosystem I: Reconstitution of the Photoelectric Conversion System on a Gold Electrode.* Angewandte Chemie-International Edition, 2009. **48**(9): p. 1585-1587.

20. Peter, L.M., *Characterization and modeling of dye-sensitized solar cells.* Journal of Physical Chemistry C, 2007. **111**(18): p. 6601-6612.

21. Heathcote, P., et al., *The role of the membrane-bound iron-sulphur centres A and B in the Photosystem I reaction centre of spinach chloroplasts.* Biochimica et Biophysica Acta (BBA) - Bioenergetics, 1978. **503**(2): p. 333-342.

22. Setif, P. and P. Mathis, *The oxidation-reduction potential of P-700 in chloroplast lamellae and subchloroplast particles.* Archives of Biochemistry and Biophysics, 1980. **204**(2): p. 477-485.

23. *Handbook of Biochemistry and Molecular Biology* 3ed. Physical and Chemical Data, ed. G.D. Fasman. Vol. 1. 1975, Cleveland: CRC Press.

24. Bard, A.J. and L.R. Faulkner, *Electrochemical Methods: Fundamentals and Applications.* 2nd ed. 2001, New York: Wiley

25. Kennis, J.T.M., et al., *Light Harvesting by Chlorophylls and Carotenoids in the Photosystem I Core Complex of Synechococcus elongatus: A Fluorescence Upconversion Study.* The Journal of Physical Chemistry B, 2001. **105**(19): p. 4485-4494.

26. Zvezdanovic, J., et al., *Chlorophyll bleaching by UV-irradiation in vitro and in situ: Absorption and fluorescence studies.* Radiation Physics and Chemistry, 2009. **78**(1): p. 25-32.

27. Baba, K., et al., *Photoinhibition of photosystem I electron transfer activity in isolated photosystem I preparations with different chlorophyll contents.* Photosynthesis Research, 1996. **47**(2): p. 121-130.

CHAPTER VII

CONCLUSIONS AND RECOMMENDATIONS

Summary

The results presented in this thesis have demonstrated the utility of Photosystem I, a naturally abundant and highly functional photoactive protein complex, in photoelectrochemical systems. We have developed a quantitative description for the photocatalytic effect produced by monolayer films of PSI and have shown how changes in fabrication methods and system geometry can increase the amount of photocurrent produced by PSI based systems (**Figure 7.1**). Dense monolayers of PSI on planar substrates formed via vacuum-assisted assembly or solution adsorption are capable of producing photocurrent densities of ~ 100 nA/cm^2 due to the direct electron transfer between the electrode surface and the photogenerated reaction centers of the adsorbed PSI complexes. This effect may be enhanced to produced photocurrents 3-4 times larger than those produced by monolayer systems on planar electrodes by decorating nanoporous gold leaf electrode films with PSI, provided that the pore sizes of the substrate are large enough to accommodate multiple PSI complexes. Dramatic enhancements to photocurrent production are provided by multilayer assemblies of PSI. Initially, these multilayer structures were formed by an agglomeration/precipitation process that occurred within the electrolyte reservoir of a self-contained photoelectrochemical cell over a period of several days. The PSI multilayer assembly process was further improved by the development of a vacuum-assisted deposition

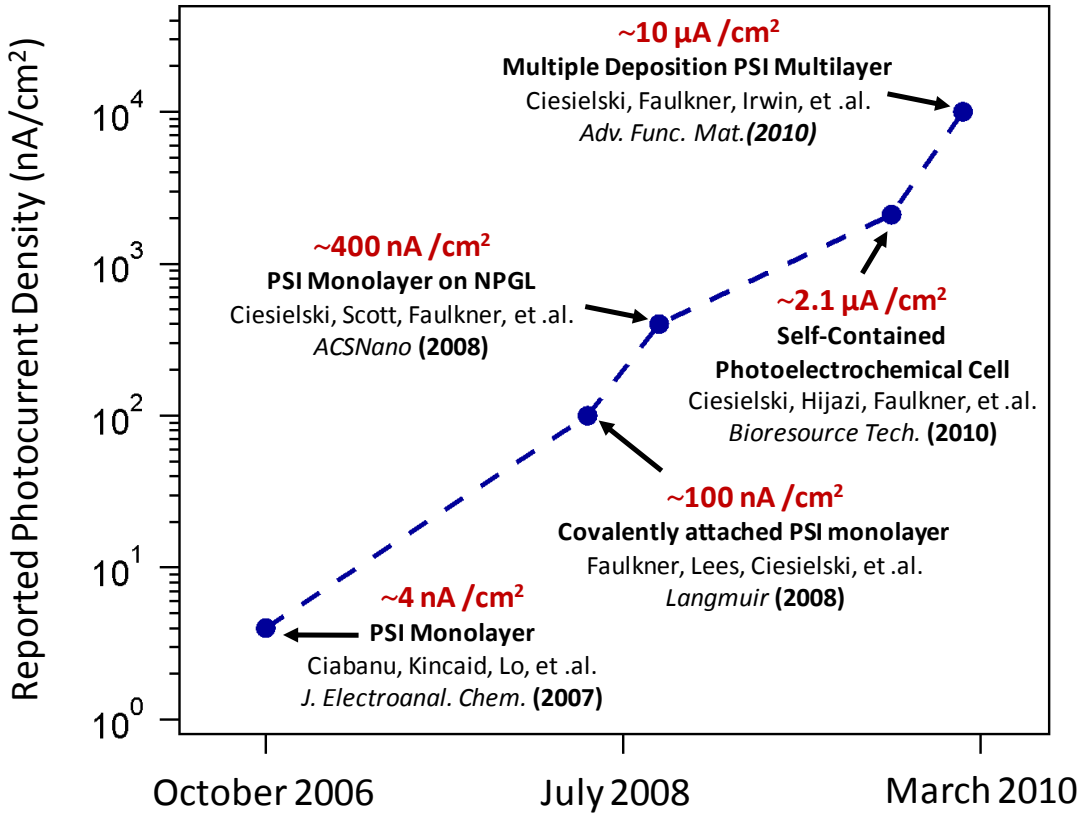

Figure 7.1. Progress in Photocurrent Production by PSI-Based Systems. The photocurrent production capabilities of PSI-bases systems produced by our group has increased by more than 3 orders of magnitude since 2007.

process which provided faster access to multilayer films of controlled thickness, and we have shown that the photocurrent production capabilities of these films increases with their thickness.

Perspectives, Future Directions and Recommendations

While considerable progress has been made in terms of photocurrent production by these systems, the power output and photoconversion efficiency of these systems must be increased substantially in order for PSI-based energy conversion technologies to

become competitive with other photoconversion technologies. In my opinion, such substantial increases are certainly feasible. The basis for my opinion is provided by the following illustration: consider a perfectly oriented PSI monolayer assembled on an electrode surface with a surface concentration Γ_{PSI} = 2 x 10^{-12} mol/cm^2 as calculated in Chapter 4. Let us assume that the entire PSI assembly is continually photoexcited such that electrons constantly move through the PSI complexes at a rate that is limited by the time it takes an electron to move from P_{700}^{*} through the electron transfer chain to reduce the terminal FeS complex to F_B^-. This "electron travel time" has been estimated to be ~ 1 μs.[1] From these assumptions, the current density produced by the PSI monolayer would be calculated as

$$\left(\frac{10^6 \text{ mol e}^-}{\text{mol PSI}\cdot\text{s}}\right)\left(\frac{2\times10^{-12} \text{ mol PSI}}{\text{cm}^2}\right)\left(\frac{9.65\times10^4 \text{ C}}{1 \text{ mol e}^-}\right) = 0.193 \text{ A}\cdot\text{cm}^{-2} \qquad (1)$$

The magnitude of this current density highlights the utility of the nanoscale dimensions and fast electron transfer capabilities of PSI, which are several of the characteristics that have attracted researchers' attention to this. Next, let us imagine that electrons may be collected from F_B^- with perfect efficiency (i.e. electrons enter the anode with the same energy they had at F_B^-), and that electrons are resupplied to PSI from a cathode whose Fermi level corresponds exactly to the redox potential of P_{700}^{+}. These assumptions are illustrated schematically in **Figure 7.2**. A device with these characteristics would exhibit an open circuit potential of -1.075 V, and would provide a power density output of

$$P = IV = (1.075 \text{ V})(0.193 \text{ A}\cdot\text{cm}^{-2}) = 208 \text{ mW}\cdot\text{cm}^{-2} \qquad (2)$$

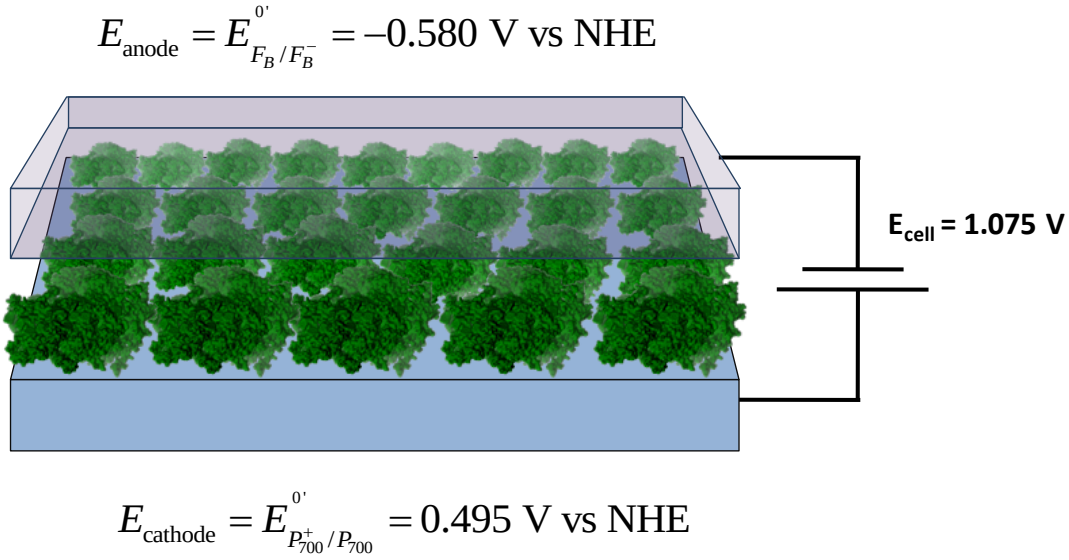

Figure 7.2. An idealized PSI-Based Photovoltaic Device. A perfectly oriented monolayer in direct electrical contact with an anode and cathode with Fermi levels that correspond exactly to the redox potentials of F_B and P_{700}, respectively, would exhibit an open circuit potential of ~1.1 V.

The maximum efficiency of such a device would be achieved when all of the photoexcitation required to continually excite the photosystems was provided by photons of 700 nm wavelengths which corresponds to the minimum energy required to excite P_{700} and initiate charge separation. The energy of one such photon is given by

$$E_{\text{photon }\lambda=700\text{ nm}} = \frac{hc}{\lambda} = \frac{\left(6.6\times10^{-34}\ \text{m}^2\cdot\text{kg}\right)\left(3\times10^{8}\ \text{m}\cdot\text{s}^{-1}\right)}{\left(700\times10^{-9}\ \text{m}\right)} = 2.8\times10^{-19}\ \text{J} \qquad (3)$$

and the energy flux required to continually photoexcite the PSI monolayer with photons of this wavelength at the rate required by equation (1) assuming a perfect quantum efficiency and total absorption is

$$E_{\text{required}} = \left(\frac{2.8\times10^{-19}\ \text{J}}{\text{photon}}\right)\left(\frac{6.02\times10^{23}\ \text{photons}}{1\ \text{mol photons}}\right)\times \left(\frac{10^{6}\ \text{mol photons}}{\text{mol PSI}\cdot\text{s}}\right)\left(\frac{2\times10^{-12}\ \text{mol PSI}}{\text{cm}^2}\right) = 337\ \text{mW}\cdot\text{cm}^{-2} \quad (4)$$

The flux of solar energy reaching the Earth's surface is often approximated as 100 mW/cm^2, thus power output of the theoretical device discussed here would likely be limited by the intensity of light reaching the device. The photoconversion efficiency of the device under these conditions is simply the ratio of the power density produce to the power density influx from irradiation, calculated by

$$\eta = \frac{208\ \text{mW}\cdot\text{cm}^{-2}}{337\ \text{mW}\cdot\text{cm}^{-2}} = 0.617 \quad (5)$$

This same efficiency is also calculated simply by dividing the standard free energy of the P_{700}^{*} state (which corresponds to the energy of a photon of 700 nm wavelength) by the standard free energy of an electron at F_B^-, using the energy of the P_{700} ground state as a reference, which is essentially calculating the photoconversion efficiency of a single PSI complex:

$$\eta = \frac{E_{P_{700}^{*}}}{E_{F_B^-}} = \frac{1.1\ \text{eV}}{1.8\ \text{eV}} = 0.61 \quad (6)$$

The theoretical efficiencies given by (5) and (6) only correspond to irritation by 700 nm wavelength photons, and energy photons of $\lambda < 700$ nm is lost as heat which would reduce these efficiencies; however, assuming the average solar photon has energy 2.3 eV, the internal photoconversion efficiency of a photon of this wavelength by a PSI complex is still η = 1.1 eV/2.3 eV = 0.49, which compares very well to efficiencies of mature photovoltaic technologies.

In light of the assumptions described in the previous discussion, as well as the results presented in previous chapters, several aspects of the PSI-based systems described in this work are revealed as obvious candidates for improvements to enhance the performance of the system. Firstly, the electron transport between the reaction centers of PSI and the charge collectors must be improved. The photoelectrochemical systems rely predominantly on electrochemical mediators to transport electrons through the electrolyte. In both monolayer and multilayer systems, only a portion of the first layer of PSI complexes may interact with the electrode directly, and charges entering the counter electrode must be carried by mediators. In order to maximize the efficiency by which charges are transported between PSI and the charge collectors in an electrochemical system, mediators must have a redox potential very close to that of the reaction center with which they are interacting such that very little free energy is wasted as heat when the charge is transferred, and the mediator must display fast electron transfer kinetics with the reaction center. These two characteristics are difficult to satisfy simultaneously, because the thermodynamic driving force for the redox reaction to occur decreases as the redox potential of the mediator approaches that of the reaction center which can translate to slower electron transfer kinetics as predicted by the theory of Marcus.[4] Nature solves this problem using redox couples bound within water-soluble proteins that specifically dock with PSI in an orientation such that the redox centers of the PSI and the electron carrier proteins are in very close proximity. This allows for kinetically fast electron transfer in the absence of a strong thermodynamic driving force. These beneficial characteristics could be imparted to the photoelectrochemical systems described in this work by the use of biomimetic mediators that dock with PSI as do

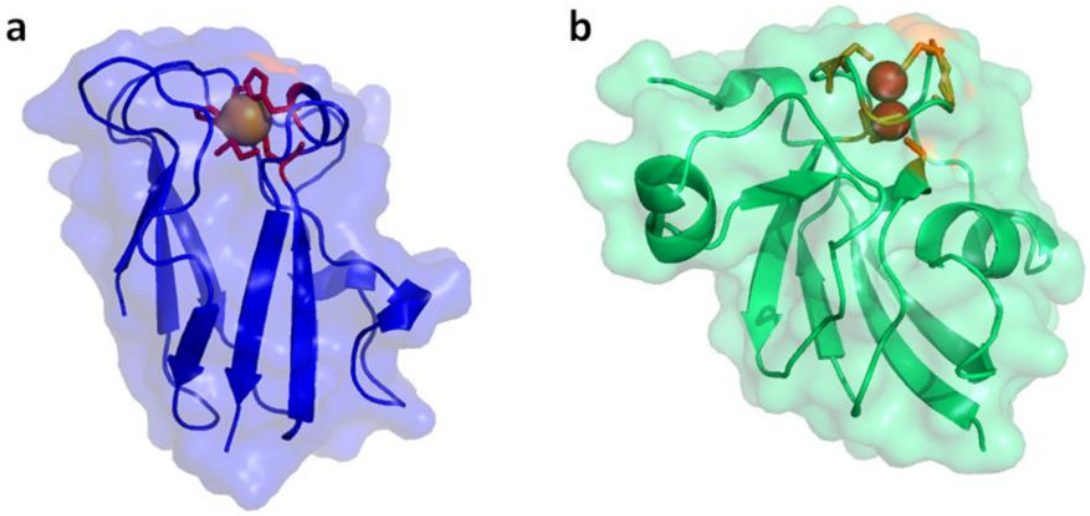

Figure 7.3. Structures of Plastocyanin and Ferredoxin. In natural photosynthesis, kinetically fast electron transfer is achieved by mobile electron carriers that dock near the reaction centers with which they interact, and little free energy is wasted because the redox potential of the electron carrier is energetically close to that of the reaction center. (**a**) Plastocyanin is a copper-containing protein that supplies electrons to P_{700}^{+}, and (**b**) Ferredoxin uses a pair of iron atoms to transport electrons away from F_B^-. These redox proteins could also be isolated from spinach during the extraction of PSI and later incorporated into the same photoelectrochemical system to serve as mediators. Atomic coordinates for plastocyanin and ferredoxin are from PDB entry 1AG6[2] and 1A70[3] respectively.

plastocyanin and ferredoxin (**Figure 7.3**). Alternatively, these proteins could be isolated along with PSI during the extraction procedure and later incorporated into the photoelectrochemical system to serve as mediators.

The perfect orientation of the monolayer as assumed in (1) was also predicted to provide large enhancements to photocurrent by the simulation described in Chapter 3. Strategies to orient monolayers of PSI have been attempted using various SAMs,[5-7] and biological mutations[8-10]. While these strategies may very well improve the uniformity of the orientation of PSI, none of these studies report dramatic enhancements

to photocurrent resulting from their orientation scheme. Based on the investigation of PSI orientation presented in Chapter 4, it is not likely that the orientation strategies in the aforementioned studies are orienting > 95% of the PSI complexes in a single configuration, as the simulation in Chapter 4 predicts that doing such would produce at least an order-of-magnitude increase in photocurrent. Complete orientation of a PSI monolayer is clearly very entropically unfavorable; nevertheless, this feat is routinely achieved to perfection within thylakoid membranes. Perhaps the successful strategy will involve the isolation and subsequent adsorption of intact thylakoid membranes in which PSI complexes remain oriented.

Another aspect of the present systems that must be improved in order to increase their efficiency is the ability of the photoactive layer to absorb light. One of the assumptions for equation (4) was that all of the photons were absorbed by the PSI monolayer. This is clearly an unrealistic assumption because the absorbance of a PSI monolayer in the visible region was below the detection limit of the spectrometer as reported in Chapter 4, and even the thickest PSI multilayer films investigated in this work, which display absorbances 10^4 - 10^5 times larger than PSI monolayer films, do not display complete absorbance throughout the visible spectrum. Perhaps the increased photocurrent production by the multilayer films is in some way a result of the similarity of this approach to the light absorption problem taken by Nature, in which thylakoid membranes are stacked into effective multilayers within the chloroplast. While increasing the thickness of the PSI film clearly increases its absorbance throughout the visible region, it does not change the fact that PSI relies predominantly on chlorophyll to absorb light. Chlorophyll displays excellent absorbance in the red and blue regions of the

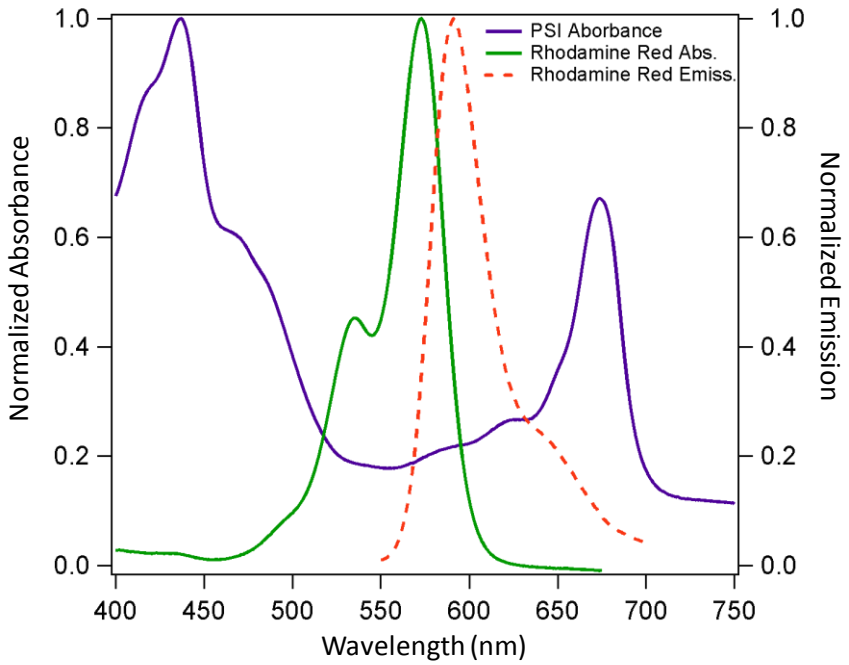

Figure 7.4. Absorption and Emission Spectra of Rhodamine Red and Absorption Spectrum of PSI. The fluorescent dye may be attached to the antenna complexes of PSI and used to increase the sensitivity of the photosystem to green photons.

visible spectrum but has a relatively low absorbance in the yellow and green regions. This is an unfortunate constraint of PSI-based devices intended to harness solar energy because the majority of solar photons have wavelengths in this region of low absorbance. This problem has been approached by several groups who have shown pigments that absorb in the green region and emit in the red region can be used to increase the sensitivity of the antenna complexes of PSI to green photons.[11, 12] Both of these studies employed Rhodamine dyes to sensitize the proteins to green light, and demonstrated the improvement by using excitation/emission spectroscopies. The absorption and emission spectra of one such dye, Rhodamine Red is shown with the absorption spectrum of PSI in **Figure 7.4**. Green photons absorbed by the dye initiate the

formation of excitons whose energies correspond to photons in the red region and are thus more compatible with the antenna complexes of PSI and ultimately more likely to initiate charge separation via the electron transport chain. Variations of this dye that contain lysine-reactive groups intended for protein labeling are commercially available, and could be used to covalently attach the dye to PSI. While this effect has been demonstrated spectroscopically, it has yet to be verified by way of photoelectrochemical photocurrent production, which would likely be an attainable goal with the resources of our group and those of our collaborators.

While the enhanced visible absorbance provided by the multilayer systems clearly provides benefit to the system, it may provide additional benefits to the photocurrent production that arise from transport phenomena. In order to optimize these benefits, we must first increase our understanding of the mechanisms by which charges are transported through the multilayer film. Simply increasing the surface concentration of PSI in the simulation described in Chapter 4 causes the model to predict large increases in photocurrent (**Figure 7.5**); however, such a modification is a poor approximation of the behavior of the multilayer system because it assumes that all the PSI complexes in the system are able to undergo heterogeneous electron transfer reactions. In order to extend the kinetic model to the multilayer system, a geometry must be defined that accurately represents the spatial distribution of the reaction centers of PSI complexes throughout the multilayer assembly. Such a simulation with considerable spatial inhomogeneity is poorly suited for the Matlab PDE solver, but could be performed using a more flexible finite element solver such as Comsol. This simulation, in tandem with the SECM and EIS experiments described in the discussion of Chapter 6, would provide considerable

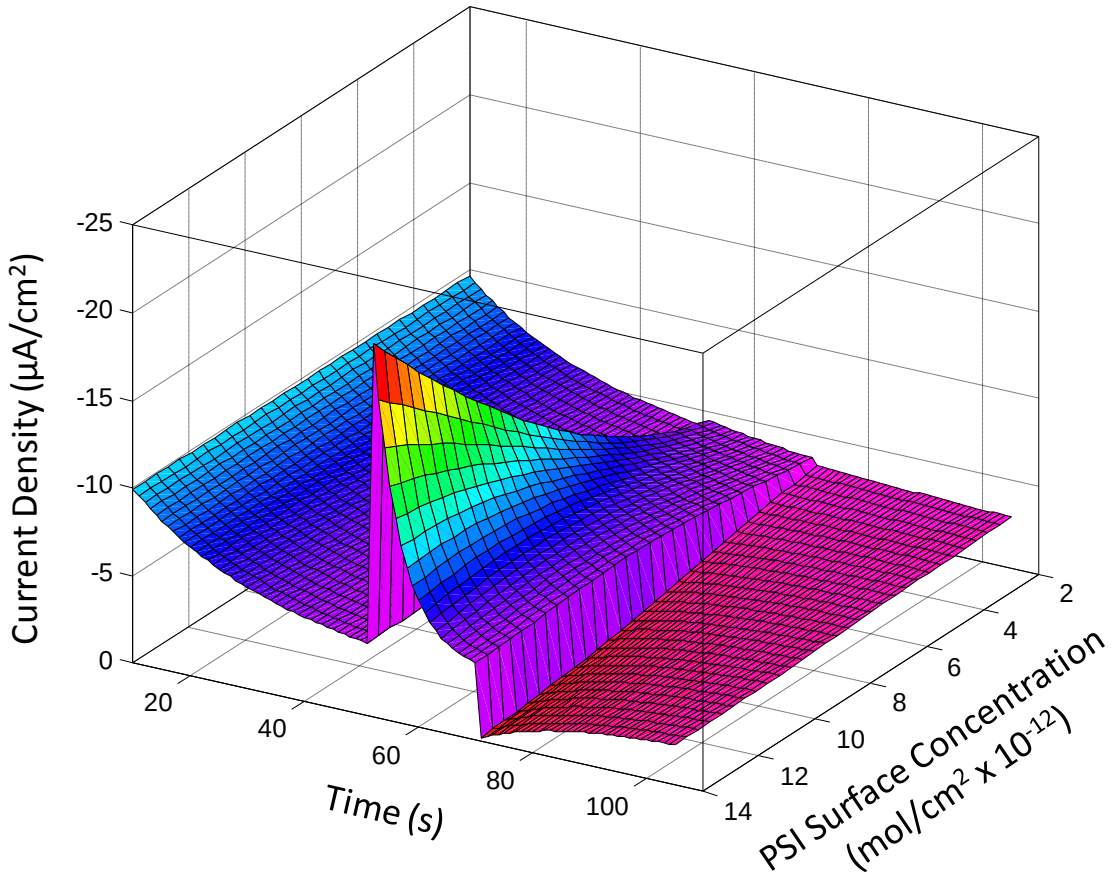

Figure 7.5. Effect of Increasing Surface Concentration in the PSI Monolayer Simulation. Increasing Γ_{PSI} in the simulation described in Chapter 4 causes the model to predict large increases in photocurrent that resemble those produced by the PSI multilayers presented in Chapter 6; however, this modification assumes that all of the PSI complexes may participate in heterogeneous reactions and neglects the thickness of the PSI film and is thus an unrealistic scenario. The model presented in 3 could be accurately extended to the multilayer system by defining the spatial distribution of the reaction centers of PSI when specifying the system geometry. Such a simulation could be performed in Comsol.

insight into the charge transport that takes place within a PSI multilayer and could identify additional strategies to further increase the performance of the system.

When the photoelectrochemical behavior of the PSI film is optimized and an improved self-contained device is to be constructed, several aspects of the design that

pertain to charge transport through the device should be considered. The efficiency of the photoelectrochemical cell presented in Chapter 5 was limited by the diffusive transport of charge carriers through the electrolyte solution. This limitation can be averted using several strategies. The first is to decrease the distance between the electrodes to < 40 μm, as diffusional limitations to photocurrent production become negligible with electrode spacings in this regime in dye sensitized solar cells.[13] Such a close spacing may be achieved using thin film sealants such as those commercially available from Solaronix to form the electrolyte reservoir of the cell instead of the much thicker PDMS layer used in the device reported in Chapter 5. An alternative to this strategy is to forgo the electrolyte reservoir entirely and attempt to make direct electrical contact between both electrodes and the photoactive layer. This strategy was attempted previously by depositing a transparent conductive material via thermal evaporation onto a PSI monolayer, and resulted in a solid state device that was reported to be highly efficient;[14] however, this work was not pursued by the authors after the original publication. A similar strategy employing a PSI multilayer could be investigated by our group by first depositing the PSI film onto an ITO-coated substrate, and then forming a direct electrical contact to the other side of the PSI film using conductive tape or by depositing a thin metallic film directly onto the protein layer. Such a device would eliminate diffusion limitations, but may suffer from poor transport within the film because of the lack of mobile electron carriers.

Conclusions

The results demonstrated in the previous chapters of this work and the perspectives presented in this section demonstrate that PSI is in a fact valuable and abundant natural resource that holds great potential for its application in photoelectrochemical systems. While great progress in the design and construction of PSI-based systems has been described in this work, the full potential of the highly efficient protein complex has yet to be realized. Improvements to the systems described herein may be achieved by the use of more effective electrochemical mediators, enhancing the absorbance capabilities of the films, eliminating the diffusional limitations of the self-contained electrochemical cells that employ PSI as the photoactive component, and by accurately simulating the mechanisms of charge transport through the PSI multilayer. These improvements and others should be undertaken to move toward PSI-based energy conversion systems that exhibit speed and efficiency comparable to that displayed by this impressive protein complex *in vivo*, as such systems would certainly be competitive with, or even outperform, current photovoltaic technologies in terms of both cost and efficiency.

Works Cited

1. Brettel, K. and W. Leibl, *Electron transfer in photosystem I.* Biochimica Et Biophysica Acta-Bioenergetics, 2001. **1507**(1-3): p. 100-114.

2. Yafeng, X., et al., *Crystal structure of spinach plastocyanin at 1.7 Å resolution.* Protein Science, 1998. **7**(10): p. 2099-2105.

3. *Structure of the Mutant E92K of [2Fe–2S] Ferredoxin I from Spinacia oleracea at 1.7 Å Resolution.* Acta Crystallographica Section D, 1998. **54**(6-2): p. 1353-1358.

4. Marcus, R.A., *On the Theory of Electron-Transfer Reactions. VI. Unified Treatment for Homogeneous and Electrode Reactions.* The Journal of Chemical Physics, 1965. **43**(2): p. 679-701.

5. Ko, B.S., et al., *Effect of surface composition on the adsorption of photosystem I onto alkanethiolate self-assembled monolayers on gold.* Langmuir, 2004. **20**(10): p. 4033-4038.

6. Kincaid, H.A., et al., *Entrapment of Photosystem I within Self-Assembled Films.* Langmuir, 2006. **22**(19): p. 8114-8120.

7. Terasaki, N., et al., *Fabrication of novel photosystem I-gold nanoparticle hybrids and their photocurrent enhancement.* Thin Solid Films, 2006. **499**(1-2): p. 153-156.

8. Frolov, L., et al., *Fabrication of oriented multilayers of photosystem I proteins on solid surfaces by auto-metallization.* Advanced Materials, 2008. **20**(2): p. 263-+.

9. Krassen, H., et al., *Photosynthetic Hydrogen Production by a Hybrid Complex of Photosystem I and [NiFe]-Hydrogenase.* Acs Nano, 2009. **3**(12): p. 4055-4061.

10. Terasaki, N., et al., *Plugging a Molecular Wire into Photosystem I: Reconstitution of the Photoelectric Conversion System on a Gold Electrode.* Angewandte Chemie-International Edition, 2009. **48**(9): p. 1585-1587.

11. Miyajima, Y., et al., *Sensitization of the primary charge separation in photosystem I to green light by an amphiphilic polymer bearing Rhodamine 6G.* Chemistry Letters, 2006. **35**(9): p. 1034-1035.

12. Gundlach, K., et al., *Filling the "green gap" of the major light-harvesting chlorophyll a/b complex by covalent attachment of Rhodamine Red.* Biochimica et Biophysica Acta (BBA) - Bioenergetics, 2009. **1787**(12): p. 1499-1504.

13. Peter, L.M., *Characterization and modeling of dye-sensitized solar cells.* Journal of Physical Chemistry C, 2007. **111**(18): p. 6601-6612.

14. Das, R., et al., *Integration of photosynthetic protein molecular complexes in solid-state electronic devices.* Nano Letters, 2004. **4**(6): p. 1079-1083.

APPENDIX A

LASER EXCITATION OF PSI MULTILAYER FILMS

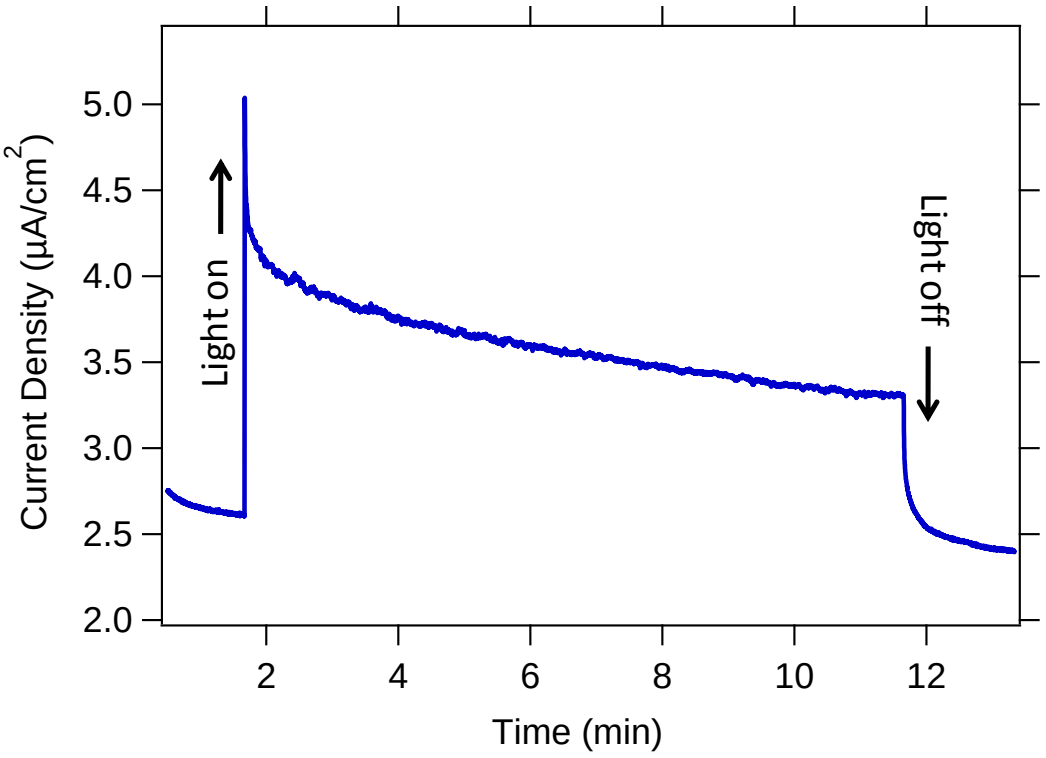

Figure A.1. Extended Irradiation of a PSI Multilayer Film. A vacuum assembled PSI multilayer film fabricated by 1 deposition step was irradiated by 678 nm light with pulse energy of 5 μJ/pulse at a repetition rate of 1 kHz for 10 min during a photochrono-amperometric experiment. The working electrode was held at a potential of -0.15 V vs Ag/AgCl in an electrolyte solution containing 250 μM dichloroindophenol, 5 mM sodium ascorbate, and 100 mM NaCl in a pH 7 phosphate buffer. The photocurrent decreased due to the depletion of the mediator at the electrode surface, but displayed no significant signs of photodamage of the PSI complexes in the film throughout the course of the experiment.

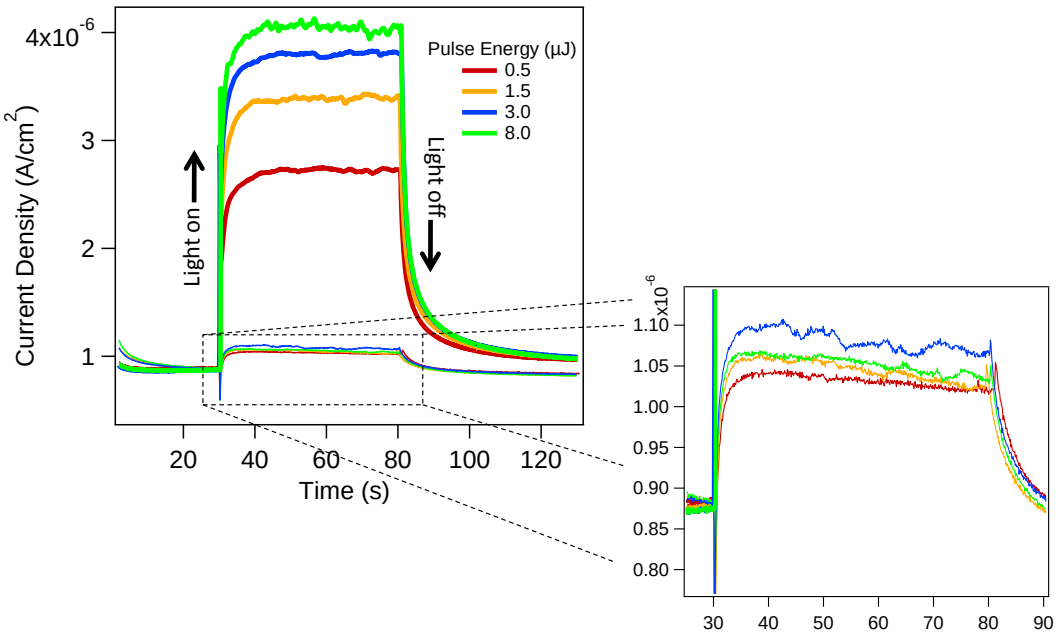

Figure A.2. Irradiation of a PSI Multilayer Film by Various Laser Pulse Energies. A vacuum assembled PSI multilayer film fabricated by 4 deposition steps was irradiated by 678 nm light at various pulse energies during a photochronoamperometric experiment. The working electrode was held at a potential of -0.085 V vs. Ag/AgCl in an electrolyte solution containing 0.1 M methyl viologen in a pH 7 phosphate buffer. **Zoom Window:** Experimental controls of identical photochronoamperometric experiments performed using un-modified electrodes reveal that small photocurrents result from photoexcitation of this electrochemical mediator in the absence of a PSI film.

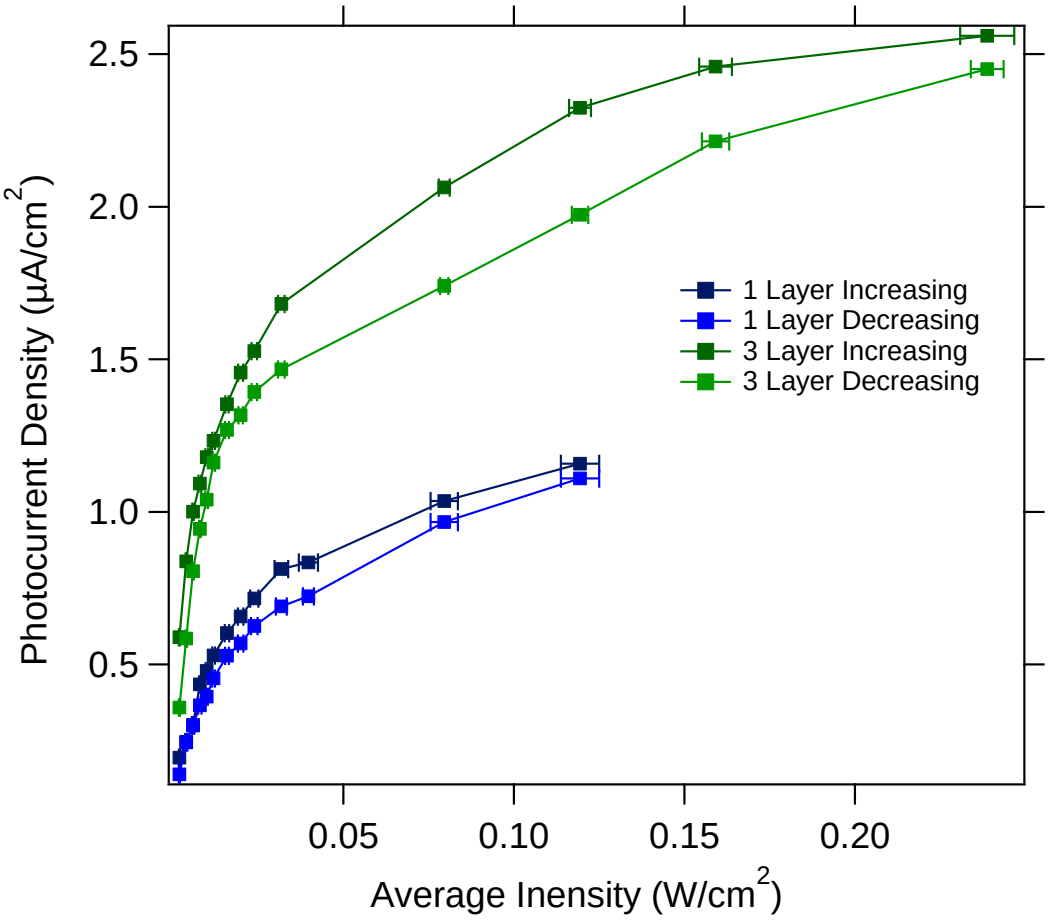

Figure A.3. Hysteresis of Photocurrent Production between Increasing and Decreasing Irradiation Intensities. PSI multilayer films fabricated by 1 and 3 deposition steps were irradiated by 678 nm light at various pulse energies and photocurrent responses were recorded. The pulse energy was increased until an asymptote was observed in the photocurrent production, which indicated the approach of saturating irradiation intensities. Photocurrent responses were then re-measured as the irradiation was decreased in order to assess reduction in photocurrent production due to photodamage of the protein films. The film fabricated by 3 deposition steps required larger intensities in order to approach saturation and produced larger photocurrents than the film fabricated by 1 deposition step at the same intensities. More hysteresis is observed in the photocurrent measurements produced by the film of 3 deposition steps because it was subjected to higher irradiation intensities that caused significantly more photodamage to the film.